University of Alberta

The performance and magnetic shielding of a 6 MV in-line linac in a parallel linac-MR configuration

by

Dan Michael Uson Santos

A thesis submitted to the Faculty of Graduate Studies and Research
in partial fulfillment of the requirements for the degree of

Master of Science
in

Medical Physics

Department of Oncology

Spring 2012
Edmonton, Alberta

Abstract

To achieve real-time image-guided radiation therapy, the integration of a linear accelerator (linac) with a magnetic resonance (MR) imager has been proposed. This thesis presents work that investigated performance and magnetic shielding of a linac in the presence of parallel magnetic flux densities. This work used computer simulations and numerical techniques such as finite element and particle tracking algorithms. It showed that a linac can operate with only a 17 ± 1 % target current lost and maintain its treatment beam's symmetry in the presence of 0.011 T parallel magnetic flux densities. Furthermore, the target current lost is the result of the altered electron gun optics when parallel magnetic flux densities are present. Minimal magnetic shielding (such as a 5-mm-thick, 146.5-mm-long passive shield or a pair of active shield coils with 625 and 430 A-turns) around the electron gun and waveguide was demonstrated to recover this lost target current.

Acknowledgements

I would like to express my gratitude to the persons that made this thesis possible. First and foremost, I would like to thank my supervisor, Dr. Stephen Steciw, for his guidance during this research project. His expertise was invaluable when solving problems that were encountered during this project. The many hours spent reviewing my manuscripts and abstracts and helping me prepare for presentations were greatly appreciated. I would like to thank Dr. Gino Fallone, my co-supervisor, for his vision and leadership in this project. He is a driving force behind this project. His advice and comments helped me to strive to be a better physicist. I would like to thank Dr. Joel St. Aubin for giving me advice and ideas and for explaining the subtleties of the simulations when I was starting this project. I would like to thank Dr. Richard Sydora, who was part of my supervisory committee, for the advice and insights that he provided during my supervisory committee meetings. Also, I would like to thank Dr. Richard Marchand, who was part of my examining committee, for his advice in improving this thesis. To the Cross Cancer Institute's Medical Physics Department and the University of Alberta's Oncology Department, I thank you for the support that I have received during my classes and this project. I am grateful to my classmates who I work with closely. They had provided comments which were sometimes useful in this project. Lastly, I would like to thank my parents and siblings for their support and encouragements during my graduate program.

Table of Contents

CHAPTER 1 : INTRODUCTION 1
- 1.1 Theses Organization 1
- 1.2 A brief background of EBRT 2
  - 1.2.1 Technological development of EBRT 2
  - 1.2.2 Evolution of EBRT treatment techniques 4
  - 1.2.3 Patient Dose Margins 5
- 1.3 Image-guided radiotherapy (IGRT) 8
  - 1.3.1 Megavoltage portal imaging 8
  - 1.3.2 Kilo voltage cone beam computed tomography (CBCT) 9
  - 1.3.3 Tomotherapy 10
  - 1.3.4 Ultra Sound (US) 11
  - 1.3.5 Fiducial Markers 11
- 1.4 Magnetic resonance (MR) imaging in IGRT 12
  - 1.4.1 Real-time MR-guided radiotherapy 13
  - 1.4.2 Linac-MR integration 13
- 1.5 Research motivation 18
- 1.6 References 19

CHAPTER 2 : BASIC BACKGROUND 25
- 2.1 Magnetostatics 25
  - 2.1.1 Biot-Savart Law 26
  - 2.1.2 Vector potential of a current loop 27
  - 2.1.3 B-field of a current loop 30
  - 2.1.4 Magnetic Force 31
- 2.2 External magnetic fields in matter 34
  - 2.2.1 The magnetic field H 34
  - 2.2.2 Diamagnetism 35
  - 2.2.3 Paramagnetism 36
  - 2.2.4 Ferromagnetism 36
- 2.3 RF linear accelerators (linacs) 38
  - 2.3.1 Electron gun 38
  - 2.3.2 Electromagnetic Theory 41
  - 2.3.3 Waveguides 43
  - 2.3.4 Dispersion relation and group velocity 46
  - 2.3.5 Root mean square emittance 51
- 2.4 References 53

CHAPTER 3 : NUMERICAL TECHNIQUES 56
- 3.1 Introduction 56
- 3.2 Finite element method (FEM) 56
  - 3.2.1 Mesh generation 57

3.2.2 Basis function selection 60
3.2.3 Formulation of elemental equation 61
3.2.4 Matrix assembly 65
3.2.5 Matrix solution 65
3.3 The particle tracking code PARMELA 66
3.4 Monte Carlo 68
3.4.1 MC optimization 69
3.5 References 71
CHAPTER 4 : LONGITUDINAL MAGNETIC FLUX DENSITY EFFECTS ON 6 MV IN-LINE LINAC 74
4.1 Introduction 74
4.2 Methods 75
4.2.1 Linac simulation 75
4.2.2 MR fringe magnetic field 76
4.2.3 Creation and optimization of the analytic current loop model 77
4.2.4 Effects of lateral misalignment of the linac in the presence of MR fringe magnetic flux densities 78
4.2.5 Extension to the stronger MR fringe magnetic flux densities 79
4.2.6 Addition of the magnetic flux densities to the linac simulation 79
4.3 Results and Discussion 82
4.3.1 MR fringe magnetic field optimization 82
4.3.2 Linac performance in the presence of MR fringe magnetic flux density 83
4.3.3 Linac performance in the presence of longitudinal homogeneous magnetic flux densities 90
4.4 Summary 94
4.5 References 95
CHAPTER 5 : MAGNETIC SHIELDING INVESTIGATION FOR A 6 MV IN-LINE LINAC WITHIN THE PARALLEL CONFIGURATION OF A LINAC-MR SYSTEM 97
5.1 Introduction 97
5.2 Methods 99
5.2.1 Electron gun’s casing 99
5.2.2 The currentloop models 99
5.2.3 In-house-designed MR imager for our linac-MR system 107
5.2.4 Linac simulation 108
5.3 Results and discussion 109
5.3.1 The *currentloop*$_{FEM}$ *model* 109
5.3.2 Electron gun output 112
5.3.3 Passive magnetic shield studies 113
5.3.4 Active magnetic shield studies 116
5.3.5 Homogeneous magnetic fields 118

5.3.6 Linac performance in the in-house linac-MR system 122
5.4 Summary 123
5.5 References 124
CHAPTER 6 : CONCLUSION AND FUTURE WORK 127
6.1 Concluding statements 127
6.2 Future work 127

List of Figures

Figure 1.1: The patient dose margins from the ICRU Report 50 and ICRU Report 62 7

Figure 1.2: The *perpendicular configuration* for the linac-MR. Reproduced with permission from Emanuel Bosser. 15

Figure 1.3: The *parallel configuration* for the linac-MR system depicting the location of the shielding studied in this report. The MR magnets for this study are superconducting coil magnets. Reproduced with permission from Emanuel Bosser. 16

Figure 2.1: The setup for the current loop where B is calculated on the test point P. 28

Figure 2.2: A pair of current loop. The top loop has current $I_1 d\mathrm{l}_1$ and a radius a_1 while the bottom loop has current $I_2 d\mathrm{l}_2$ and a radius a_2. d is the separation distance between the two current loops. 33

Figure 2.3: A representative magnetization curve for a ferromagnetic substance. 37

Figure 2.4: A schematic diagram showing a cross-sectional view of a Pierce-diode electron gun. 39

Figure 2.5: A schematic diagram of a) a forward travelling-wave waveguide[18] and b) a standing-wave waveguide.[8,18] 44

Figure 2.6: A schematic diagram of a) a cylindrical waveguide and b) an iris-loaded waveguide used to create slow waveguides 45

Figure 2.7: A representative dispersion relation plot for a uniform waveguide. The solid blue curve is calculated from Eq. 2.57 while the red dashed line is a plot of a linear dispersion relation where $\omega = ck_{z0}$. The y-intercept of the blue curve is the cut-off frequency ω_c. 47

Figure 2.8: A transverse a) phase-space projection and b) a trace-space projection when the effects of nonlinear forces on the particle beam are ignored. 52

Figure 3.1: Possible finite element shapes for a system that is a) one dimensional, b) two dimensional, and c) three dimensional. d) Finite element shapes with curved edges. The red dots in each of the finite element shape are called nodes. 58

Figure 4.1: A flow diagram which shows the creation of the *currentloop*$_{analytic}$ *model* to the addition of magnetic flux density via external magnetic flux density maps to the linac simulation. 81

Figure 4.2: A diagram of the *currentloop*$_{analytic}$ *model* showing the current loop configurations. 82

Figure 4.3: The calculated magnetic fields (solid line) and the PARAmed isoline data (dots) along the symmetric axis of the *currentloop*$_{analytic}$ *model* in Fig. 4.2.. 83

Figure 4.4: The phase-space of the electron gun output beam when a) 0 T, b) 0.0022 T, c) 0.0049 T, and d) 0.011 T MR's fringe magnetic flux densities are present at the electron gun cathode. In the figures, *r* and *r'* are calculated by Eqs 2.68 and 2.69, respectively. 84

Figure 4.5: The energy distribution of the linac electron beam at the linac target from different MR magnetic flux densities at the electron gun cathode.......... 86

Figure 4.6: The cross-line spatial distribution of the electron beam at the target for the normal 0 T case and three linac-MR SAD setups.......... 87

Figure 4.7: MC simulations of a 40 x 40 cm^2 treatment beam were performed in collaboration with another student.[6] The cross-line dose profiles (a-c) at 1.5 cm depth were compared to measurements taken from a linac operating in 0 T. The DD curves in d are from a simulated linac were normalized at the dose at D_{10} but scaled for visual clarity. 89

Figure 4.8: The electron gun's cathode emission current and injection current in the presence of parallel magnetic flux densities. The injection current rises slowly, at first but drops when the flux density increases beyond 0.012 T.......... 91

Figure 4.9: A quarter cut-out of the electron gun is shown to show its electron beam in the normal 0 T case and three parallel homogenous fringe magnetic flux densities.......... 93

Figure 4.10: The relative target current for a linac in the presence of homogenous fringe magnetic flux densities.......... 94

Figure 5.1: Cross-section of a passive magnetic shield setup.......... 102

Figure 5.2: A schematic diagram showing the location of the a) passive and b) active magnetic shields relative to the linac electron gun and waveguide. 103

Figure 5.3: A flow diagram showing the passive and active magnetic shielding process.......... 105

Figure 5.4: Plots of the differences in B_x, B_y, and B_z (in a, b, c, respectively), from the gun casing simulations (with and without the 1 cm hole on its side). The differences are plotted along the electron gun's central axis and ±3 mm off-axis. 111

Figure 5.5: The phase-space diagram for an electron gun output beam is shown for four simulation conditions: a) a linac during normal operation (0 T), b) an unshielded linac, c) a passively shielded linac (which used a 5-mm-thickness and 146.5-mm-long passive shield), and d) an actively shielded linac. For scenarios b to c, a linac-MR SAD setup of 1.0 m was used. In this figure, *r* and *r'* are the radial distance and angular deflection calculated by Eqs 2.68 and 2.69, respectively. 113

Figure 5.6: The target current (as a percentage of the nominal case) for four passive shield thicknesses is plotted against the passive shield length. The linac-MR SAD setup of 1.0 m was used for the simulations. At a shield length of

146.5 mm, full target current recovery is possible for the four shield thicknesses. 114

Figure 5.7: The mean magnetic flux densities in the electron gun plotted against the passive shield length for the four passive shield thicknesses in Fig. 5.6. 115

Figure 5.8: The relative injection currents (as a percentage of the nominal injection current) for four passive shield thicknesses are plotted against the homogeneous magnetic flux density magnitudes. A fixed passive shield length of 146.5 mm was used for all shield thicknesses investigated. 120

Figure 5.9: The relative target current (as a percentage of the nominal target current) as the longitudinal homogeneous magnetic flux densities are increased. A fixed passive shield length of 146.5 mm was used for all shield thicknesses investigated. 121

List of Abbreviations

3D CRT	3D conformal radiotherapy
6D	6 dimensional
CBCT	Cone beam computed tomography
CDF	Cumulative distribution function
CT	Computed tomography
CTV	Clinical target volume
D_{10}	Depth dose at 10 cm depth
D_{CAX}	Central axis dose
DD	Depth dose
DSV	Diametrical spherical volume
EBRT	External beam radiation therapy
ECUT	Electron transport cut-off energies
EM	Electromagnetic
EPID	Electronic portal imaging device
FEM	Finite element method
GTV	Gross tumor volume
ICRU	International Commission on Radiation Units and Measurements
IGRT	Image-guided radiotherapy
IM	Internal margin
IMRT	Intensity-modulated radiotherapy
kV	Kilo voltage
linac	Linear accelerators
MLC	Multileaf collimators
MC	Monte Carlo
MR	Magnetic resonance
MV	Megavolt
OAR	Organ at risk
PARMELA	Phase and Radial Motion in Electron Linear Accelerators

PCUT	photo transport cut-off energies
PDE	Partial differential equation
PDF	Probability distribution function
PIC	Particle-in-a-cell
PTV	Planning target volume
RDF	Real-time fluorescent dosimeter
RMS	Root mean square
RF	Radio-frequency
SAD	Source-to-axis-distance
SM	Setup margin
TM	Transverse-magnetic
US	Ultra sound

CHAPTER 1 : INTRODUCTION

1.1 Theses Organization

Before discussing the topic of the project, the thesis organization is presented first in this chapter. The rest of CHAPTER 1 introduces the background and the motivation behind the work presented in this document. The background of the external beam radiation therapy (EBRT) begins with a brief historical overview of the evolution of the technology that was used in EBRT: from the initial discovery of the X-rays to the commercial availability of medical linear accelerators (linac). In addition, some background on the evolution of the treatment techniques in EBRT is provided. Image-guided radiation therapy (IGRT), which has the goal of maximizing the tumor dose while minimizing the normal tissue dose, is discussed next. Afterwards, details about the linac-MR project and how the work presented here fit within the linac-MR project is presented. In CHAPTER 2, a derivation of the magnetic field and force equations for a current loop is presented. This is followed by a short discussion of magnetism. Then, a discussion of the linac electron gun and waveguide is presented. In CHAPTER 3, descriptions the various numerical techniques (such as the finite element method (FEM), particle tracking software, and Monte Carlo (MC)) used by the software packages in the linac simulation are presented. In CHAPTER 4, discussions about the linac performance in the presence of longitudinal magnetic fields are presented. The work presented in CHAPTER 4 was published as “Effects of longitudinal magnetic fields on a simulated in-line

6 MV linac" in *Medical Physics*. CHAPTER 5, in turn, discusses the methods employed to minimize the adverse effects of the longitudinal magnetic fields: magnetic shielding. This work presented in CHAPTER 5 has been submitted for publication as "Magnetic shielding investigation for a 6 MV in-line linac within the parallel configuration of a linac-MR system" in *Medical Physics*. The conclusion derived from this project and future work are presented in CHAPTER 6.

1.2 A brief background of EBRT

1.2.1 Technological development of EBRT

The technology used for radiation treatment developed shortly after the discovery of X-rays by W. C. Roentgen in 1895.[1-2] X-rays were produced by a Crookes tube,[1] which is a partially evacuated glass tube with a cathode and an anode. The Crookes tube is a cold cathode vacuum tube and does not rely on an independently heated cathode for thermionic electron emission. Electrons were liberated from the cathode and were accelerated towards the anode through the potential difference between the cathode and anode. This electron beam, called cathode rays during this period, impacted onto the anode to produce X-rays primarily through Bremsstrahlung interactions.[3] Although the first patient was successfully treated via radiation therapy[4,5] in 1899, many early radiation therapy treatments suffered from inaccuracies of radiation delivery[4] and from long exposure times.[2,4] The low peak energies of the X-rays used in early radiotherapy treatments (< 100 kVp)[6] limited treatment sites to mostly superficial lesions.[4]

Combined with the long exposure times, the low peak X-ray energies could cause severe damage to the skin and surrounding soft tissue[4] when treating deep-seated tumors. While treatments of deep-seated tumors using a single radiation field failed, there was some success when multiple radiation field techniques were introduced by Dr. Béclère in 1908.[7]

In 1913, the Coolidge tube, which uses an independently heated cathode filament and harder vacuum, was introduced[4,8] to the medical world. The Coolidge tube allowed the peak X-rays energies to increase to 140 kVp,[4] which is sufficient for diagnostic purposes.[3,4] By the 1940s, peak X-ray energies were increased to 400 kVp, which were suited for deep-seated tumor radiation treatments.[4,9]

The next set of technological advancements in EBRT led to treatment units with increased treatment beam energies. By using a 30 foot evacuated X-ray tube[10] and a Cockcrott-Walton high voltage direct current generator, a potential difference of 1 MV across the x-ray tube could maintained, making 1 MV treatment beams possible.[10] This increased beam energy allowed for deep-seated tumor treatments. In 1937, one of the first megavolt (MV) treatment units was used for patent treatment and research in the St. Bartholomew's Hospital (Barts), London.[10] By 1940, there was no doubt about the advantages of treatment beams with 1 MV or greater mean energy for radiation treatment of deep-seated tumor.[10-12]

In addition to using X-ray tubes, radionuclides and particle accelerators gave the means of increasing the treatment energy beyond 1 MV. A ^{60}Co unit was first used in patient treatments in the Saskatoon Clinic, Saskatoon, Saskatchewan, Canada in 1951.[4] These radiotherapy units use ^{60}Co radionuclide sources,[3,4] which is an artificially created radionuclide through the neutron irradiation of ^{59}Co.[4] Its mean photon energy (1.25 MeV) is a high enough X-ray energy to have a skin sparing effect[10] during treatment. Increased treatment beam energy via particle accelerators came with the development of the betatron by Donald W. Kerst from the University of Illinois,[10] Champaign, Illinois, USA. The betatron used an increasing magnetic flux to accelerate electrons.[10] The accelerated electron beam was nearly monoenergetic and had a beam energy of 2.3 MeV at first.[10] Later, accelerated electron energy of 300 MeV was possible.[10] In 1948, the first patient was successfully treated with the betatron[10] by mounting an X-Ray target on the injector assembly. In addition to the betatron, medical linacs also provided a means of generating MV X-ray beam for radiotherapy treatments. Megawatt microwave generators, which were originally developed for and applied to radar, were applied to linacs after World War II.[10,13] This led to the klystron, which amplifies microwave power, and the magnetron, which generates microwave, to become megawatt microwave sources for linacs[10] and allowed medical linacs, in the 1960's, to reached X-ray beam energies of up to 25 MV.[4]

1.2.2 Evolution of EBRT treatment techniques

In the early development of radiation treatments, treatments were delivered with a single prolonged exposure; consequently, soft tissue injuries accompanied the radiation treatment,[4] especially from treatments involving deep-seated tumors. Improvements to radiotherapy techniques came with the introduction of multiple radiation fields by Dr. Béclère, which was mentioned earlier and multi-fractionated radiotherapy by Regaud, Ferroux, and others.[14] The increasing treatment energy (from kV energies to MV energies) helped during the radiation treatments of deep-seated tumors. Not long after the development of both the ^{60}Co units and medical linacs, complicated field shaping devices (such as Johns and Cunningham's work[15] on the ^{60}Co units in 1959 and Takahashi's work[16] on the multileaf collimator (MLC) in 1965) that helped make the treatment beam conform to the tumor shape and dose delivery concepts (such as Brahme's work (1982) and Cormack's work (1987) on the rotation therapy)[17,18] started to be investigated. The increasing power of computers allowed for the development of 3D conformal radiotherapy (3D CRT) in the 1970s and dose escalation techniques such as intensity-modulated radiotherapy (IMRT)[6] in the 1980s. With dose escalation, increased probability of tumor control was possible while the probabilities of normal tissue complications are reduced.[6] However, greater accuracy in treatment delivery was needed. As the computer-controlled MLC became more commercially available, the current implementation of IMRT became possible.[6]

1.2.3 Patient Dose Margins

A major goal in radiotherapy is the delivery of tumor killing dose and to maximize tumor control while sparing the surrounding healthy tissue from the radiation dose. To achieve this goal, radiotherapy treatments need an accurate treatment beam delivery. For current dose delivery techniques such as IMRT, there is greater emphasis on precision and accuracy.[6] However, there are still geometric uncertainties that arise such as the patient's setup which cannot be replicated exactly for each daily treatment. In addition, there are tumor and/or organ motion during the treatment. To help account for these uncertainties and provide guidelines on the tumor and organ at risk (OAR) localizations and dose margin definition during radiotherapy treatment planning and contouring, the International Commission of Radiation Units and Measurements (ICRU) published the reports ICRU 50[19,20] and ICRU 62[21].

The first dose volume that is contoured from the patient's planning image data set, which primarily consists of a CT data set, is the gross tumor volume (GTV). The GTV which is defined by the ICRU in the ICRU Report 50[19] and 62[21] and includes the volume of tissue with the palpable tumor growth that is detectable from the patient's planning image data set.[19] The GTV is then enclosed in a larger dose volume called the clinical target volume (CTV). The CTV is used to account for microscopic tumor growth that would not be detectable in the planning image data set.[19] During the patient radiotherapy treatment, the CTV's size, shape, and position inside the patient can change. In addition, the patient's daily setup cannot be reproduced exactly. Therefore, the CTV is encapsulated in a larger dose volume called the planning target volume (PTV). The CTV-to-PTV margin accounts for the uncertainties associated with the patient's daily setup and the geometric changes in the CTV during treatment.[19,22] In the ICRU 62, the CTV-to-PTV margin was divided into two margins to explicitly separate the

CTV's geometric uncertainties and the uncertainties in the patient's daily setup[21,22]. The internal margin (IM) is defined in ICRU 62 as the volume added to the CTV to account for the CTV's geometric uncertainties in the patient.[22] The second part of the CTV-to-PTV margin defined in ICRU 62 is the setup margin (SM), which accounts for the uncertainties in treatment beam locations that relates to the patient daily setup.[22] Therefore, the CTV-to-PTV margin consists of IM and SM. The patient dose margins discussed above is shown in Fig. 1.1.

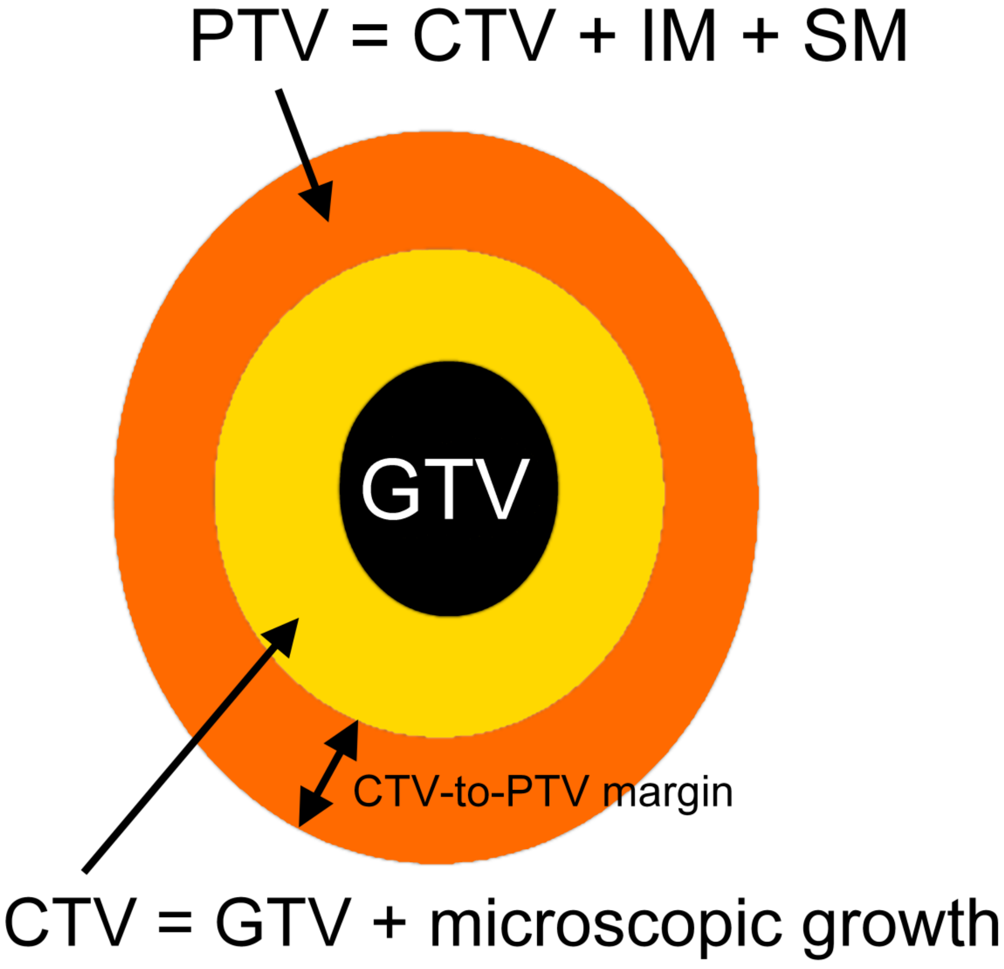

Figure 1.1: The patient dose margins from the ICRU Report 50 and ICRU Report 62.

Reducing the CTV-to-PTV margin will in turn reduce the volume of healthy tissue that would be irradiated during the radiotherapy treatment session. As a result, less patient side effect will occur and therefore improve the patient's treatment outcome.

In current IGRT techniques, the CTV-to-PTV is reduced by minimizing the SM. The patient is imaged prior to treatment. Then this pre-treatment image data set is compared with the planning CT (computed tomography) image data set. Appropriate treatment couch shifts and rotations are then applied to minimize the patient's daily setup variation. The next section describes the different imaging modalities that are used to take the pre-treatment image data set that was used in IGRT.

1.3 Image-guided radiotherapy (IGRT)

Current IGRT treatments require a daily acquisition of the patient's image data prior to treatment.[4] This priori information is compared to the patient's planning image data set where appropriate adjustments such as treatment couch shifts and/or rotation can be applied to minimize the daily setup variation.[4] A variety of imaging modalities can be used to acquire the patient's daily image data set.

1.3.1 Megavoltage portal imaging

MV portal imagers are imaging devices that use the linac's treatment beam to create a 2D radiograph of the patient.[23] These radiographs are usually taken prior to the patient treatment for setup verification. Because this imaging modality uses MV X-rays, it suffers from poor soft-tissue contrast.[24] The early portal imagers used for the patient's treatment verification were film-based.[25] Because of the poor contrast in the patient's MV radiographs, these film-based portal images needed a great deal of skill and time to visually interpret its images.[25] In 1986, Leong applied digital fluoroscopy to radiotherapy and developed a real-time fluorescent dosimeter (RFD). The RFD produced portal images that are of good visual quality and acted as a large array (512x512) of dosimeters with the 10 MV X-rays.[26] The current generation of MV electronic portal imaging devices (EPIDs), however, consist of an active matrix flat panel detector[27] which is integrated with a linac. These detectors provide a more improved image resolution of 1024 x 512 pixels than the RFD portal images. Both the RFD and MV EPID imagers are capable of real-time image acquisition. Through digital manipulation, such as digital image filtration and window and level manipulation, EPID imagers are more flexible than the film-based portal imagers and have improve visual interpretation. The automated field shape verification and pre-treatment patient setup verification from digital EPID images are possible.[25]

1.3.2 Kilo voltage cone beam computed tomography (CBCT)

Cone beam CT (CBCT) is another modality used in IGRT. The Elekta Synergy^{TM} (Elekta, Crawley, UK) was the first commercially available IGRT system with an integrated CBCT[28,29] which was followed by the Varian Trilogy^{TM} (Varian Medical System, Palo Alto, CA, USA).[30] The integrated CBCT of an

IGRT linac consist of a retractable kilo voltage (kV) X-ray source, an amorphous silicon flat panel imager, and software to control the CBCT system. The source and imager are mounted perpendicular to the linac's treatment beam.[30] Prior to the patient's treatment, the gantry is rotated around the patient acquiring hundreds of two-dimensional radiographs.[23,30] A volumetric image is reconstructed by using back-projection method.[23] These kV CBCT's volumetric images provide sufficient contrast between the fat, vessels, and muscle groups[31,32] for clinical use. However, organ motion such as free breathing causes blurring artifacts to appear in the images because of the slow image acquisition. Prior to treatment, the difference between the pre-treatment data set and the planning data set is calculated and displayed.[30] Then, three dimensional translations and three axes rotation of the treatment table and patient based on the difference between the two data sets is made to minimize pre-treatment setup variation.[30]

1.3.3 Tomotherapy

First proposed in 1993 by Mackie *et al.*, the helical tomotherapy (TomoTherapy, Inc., Madison, WI,USA)[30] uses a 6 MV in-line linac that rotates around the patient in a fashion similar to a helical CT study[30] in which the patient couch moves into the bore of the machine during normal operation. Prior to treatment, an MV CT image of the patient is taken using a detuned linac (3.5 MV X-rays)[23]. The used of MV X-rays for imaging helps to reduce artifacts that are caused by high-atomic-number materials such as metal prostheses.[23] However, like with the MV EPID images, its MV CT images suffer from poor soft tissue contrast. The pre-treatment image is compared to the planning CT image, and the patient couch is shifted and rotated appropriately to minimize the daily setup variations.[23]

1.3.4 Ultra Sound (US)

Ultra sound (US) was pioneered by Wild and Reid in the 1950s.[4] It consists of a transducer array that propagates longitudinal waves through the patient's tissues and receives the reflected wave from the interfaces between different tissues.[4] Images that offer some soft tissue visualization[23] can be made by timing the reflected wave from the tissues interfaces. Therefore, image guidance based on soft tissue images for radiotherapy is possible with the use of US. Although this relatively inexpensive technology[23] is widely used for daily prostate localization,[4] US is limited to sites where there is a clear boundary between different tissues. In addition, US is not suitable in a site with large air gaps and bone since reflections for these air gaps and bone can overwhelm the reflected signal coming from soft tissue.[23] Because US relies on tissue boundaries, it has poor image quality when imaging within soft tissues. Furthermore, proper use of US and interpretation of the US images require great technical user skill and user training. Therefore, another problem with US is that image quality is greatly dependent on the user's skill.[23]

1.3.5 Fiducial Markers

In some treatment sites such as the prostate, there is significant variation in the organ location relative to bony landmarks[23] during the course of the radiotherapy treatment. Implanted markers (such as gold seeds or stainless steel screws[33]) are used as surrogates for the tumor location during localization. These implanted markers can be tracked by an EPID, flat panel detectors like in the Cyberknife's Synchrony system (Accuray, Sunnyvale, CA, USA), or an external radio-frequency (RF) antenna to provide target localization. In cases such as the Synchrony system, the tracked implanted markers are used in conjunction with external markers[33] to provide real-time target tracking.[33] Although these markers can enable better tumor localization over the other methods, there is a risk of infection[23] from surgery that should be considered. In addition, there is also a possibility of the tumor spreading along the needle track during the surgery.[23] The implanted markers also have the risk of seed migration when large tumor/target motion occurs such as in the lung.[31]

1.4 Magnetic resonance (MR) imaging in IGRT

In current IGRT techniques, direct 3D real-time tumor/target tracking is not possible. In most techniques, daily pre-treatment image data sets of the patient are taken and compared to the patient's planning CT image data sets prior to treatment. Appropriate shifts and rotations are made to the treatment couch to minimize the patient's daily setup variations. However, the tumor/target can have intra-fractional motion, and the techniques discussed above lack direct real-time tumor/target tracking capabilities. Consequently, CTV-to-PTV margin still needs to be enlarged to the full extent of the tumor/target motion to ensure that the tumor/target receives the prescribed dose. Other techniques such as the Synchrony and Varian's RPM systems (Varian Medical Systems, Palo Alto, CA, USA) are capable of real-time tumor/target tracking through surrogates such as external markers[34] and implanted markers based on the patient's planning CT data set. However, these markers are only surrogates for the tumor/target motion.

1.4.1 Real-time MR-guided radiotherapy

In order to achieve true 3D real-time tumor/target tracking without the use of surrogates, various groups around the world are integrating a magnetic resonance (MR) imager with an external beam treatment delivery unit such as a linac or ^{60}Co unit.[35-37] The MR imager can acquire the patient's 3D real-time images with a soft-tissue contrast that is superior to the images from the other imaging modalities described in § 1.3. Guided by the MR's 3D real-time images, the linac or ^{60}Co unit can shape the treatment beam to closely conform to and follow the tumor/target. As a result, less healthy tissue will be irradiated; therefore, patient side effects, which arise from the toxicity of the irradiated healthy tissue, would be reduced. Better patient survival outcomes would be a result.

1.4.2 Linac-MR integration

The various designs for an integrated linac-MR or cobalt-MR generally fall under two categories. The first category uses a stationary solenoid MR system while the linac or ^{60}Co units rotate around the patient and the MR's solenoid magnets. The main magnetic field $\boldsymbol{B_0}$ for this design is perpendicular to the treatment beam. The Utrecht group[36] from the University Medical Center Utrecht in The Netherlands uses a linac-MR design that falls into this category. Their group is integrating a 1.5 T Philips Achieva MRI system (Best, The Netherlands) with a 6 MV Elekta linac (Crawley, UK).[36,38] In their design, the treatment beam will passes through the MR's magnet (which consist of layers of aluminum and cryogens) before it reaches the patient;[38] therefore, beam hardening and attenuation in the treatment beam will result. There may also be increased scatter-dose to the patient from the scatter radiation. From the University of Florida, Viewray's cobalt-MR system, which integrates three ^{60}Co sources with a stationary split-field solenoid MR system, falls under this design category as well.[37] Unlike the Utrecht group, their design allows the cobalt-MR system to irradiate the tumor/target unattenuated through the opening between the magnets of a split-field MR imager.[37]

In the second category of linac-MR designs, both the linac and MR magnet rotate in unison with each other. Therefore, the linac is stationary in relation to the MR magnet. Any eddy current induced when a conductor (such as the linac and the gantry) moves inside a magnetic field is eliminated. In addition, the MR's main magnetic flux density $\boldsymbol{B_0}$ can either be perpendicular or parallel to the linac's treatment beam which allows for greater flexibility in the linac placement compared to the first linac-MR category. Our group at the Cross Cancer Institute (CCI), which is lead by Dr. Fallone, is investigating linac-MR designs that fall under this second category.

The linac and MR systems are two medical technologies that work well when used separately; however, the integration of a linac with an MR imager has many technological challenges. The linac emits RF radiation which interferes with the MR imager, and the presence of the MR's magnetic fields interferes with the linac's operation. Our group has investigated and found solutions to many technological challenges encountered in the linac-MR intergration.[35,39-46] Our group was the first to built and test a prototype linac-MR design in 2009[35] where a Varian 600C linac was integrated with a 0.2 T bi-planar permanent magnet MR imager with a pole-to-pole opening of 27.9 cm. This first linac-MR prototype, shown in Fig. 1.2, places the linac in between the bi-planar magnets where $\boldsymbol{B_0}$ is perpendicular to the treatment beam. This linac-MR configuration will be referred to as the *perpendicular configuration* onwards in this document.

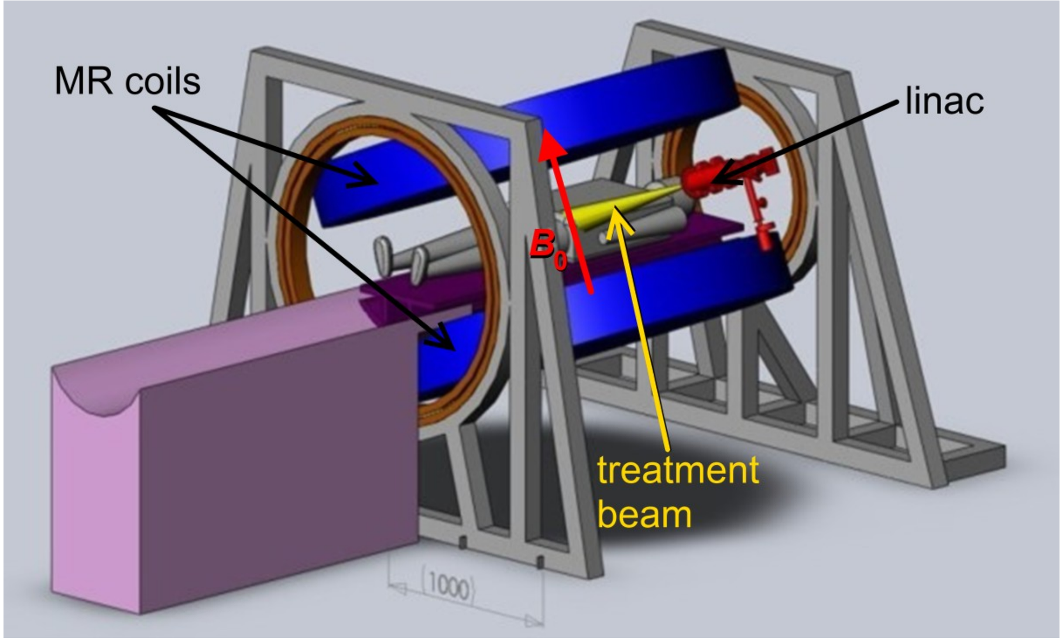

Figure 1.2: The *perpendicular configuration* for the linac-MR. Reproduced with permission from Emanuel Bosser.

A second configuration, which was proposed by our group, places the linac along the central axis of the MR magnets where $\boldsymbol{B_0}$ is parallel (or anti-parallel) to the treatment beam (Fig. 1.3). This configuration will be called the *parallel configuration* in this document and will be used in the second linac-MR prototype, which will integrate a Varian 600C linac with a PARAmed 0.5 T MROpen^{TM} (North Andover, MA) superconducting magnet. As with all coil (resistive or superconducting) magnets, the MROpen^{TM} has a bore, which, when the material that covers it is removed, is sufficiently large enough to create an opening for a radiation field to pass through.

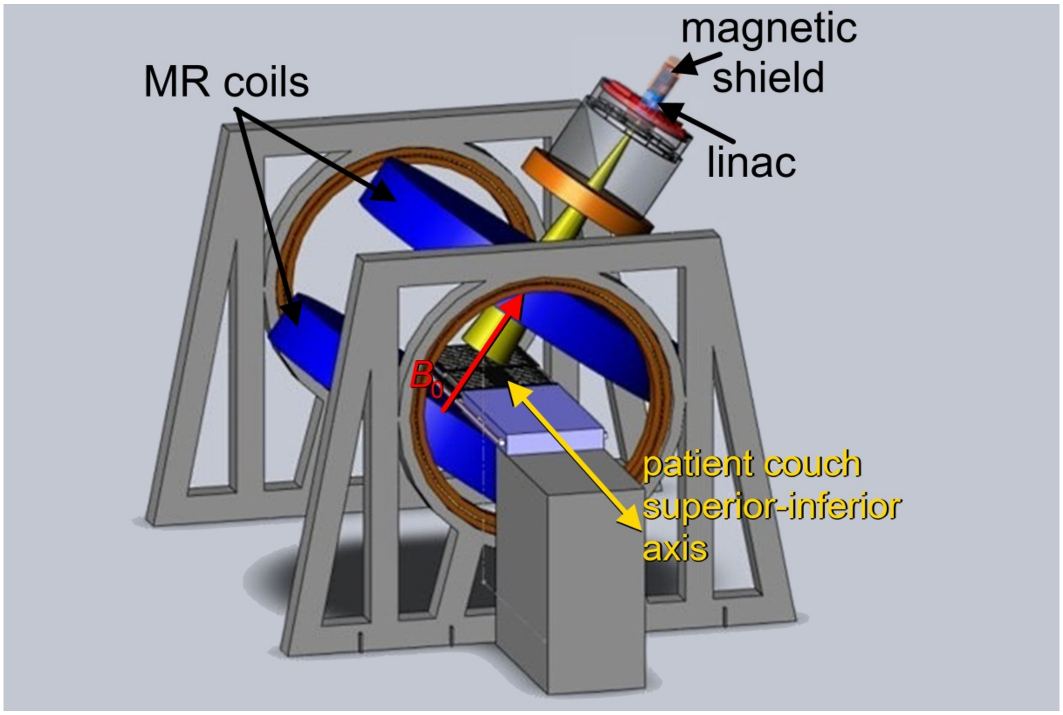

Figure 1.3: The *parallel configuration* for the linac-MR system depicting the location of the shielding studied in this report. The MR magnets for this study are superconducting coil magnets. Reproduced with permission from Emanuel Bosser.

In the *perpendicular configuration* as well as the first linac-MR category, the electrons liberated in the patient experience a Lorentz force, which results in a net transverse deflection in their trajectories. Our group have shown that these magnetic deflections in the patient significantly changes the patient dosimetry by producing hotspots as high as 20% at the tissue/air interfaces such as the lungs[39,40] when compared to the normal 0 T case for the same treatment plan. As the $\boldsymbol{B_0}$ is increased, the magnitude of these hotspots will increase. Therefore, these hotspots would be more detrimental the patient dosimetry when stronger MR magnets, such as the 1.5 T solenoid magnet used by the Utrecht group, are used.[40] Although a MC IMRT optimization[47] may overcome this limitation, there is no report in literature of a MC IMRT optimization that successfully removed these hotspots in the lung at the time this document was written. Furthermore, the beamlets that are required in the IMRT optimization need to be calculated by using MC, which is independent of the optimization package; this takes a considerable amount of time and can be tedious to implement. The MR fringe magnetic flux densities in the *perpendicular configuration* traverse the linac waveguide and electron gun perpendicular to the overall electron trajectories inside those structures. Therefore, the fringe magnetic flux densities also exert Lorentz forces on the electrons in the waveguide causing a net deflection of their trajectories and reducing the current incident on the target. Consequently, a reduction in the linac's useful radiation output occurs. Although the presence of small fringe magnet fields such as 1.4 x 10^{-3} T transverse magnetic fields can result in a 100 % treatment beam loss,[42] this beam loss can be reduced by magnetically shielding the linac electron gun and waveguide.[46]

In the *parallel configuration* described previously, the Lorentz force experience by the secondary electrons in the patients will direct the electrons in the direction of the treatment beam. This will result in the magnetic collimation of the scattered electrons from the linac head and secondary electrons in the patient. The collimation of electrons in the patient is beneficial, reducing the occurrence of hot spots at tissue/air interfaces in the patient dosimetry.[40] In addition, this magnetic collimation can result in smaller treatment beam penumbra and sharper dose distribution during treatment.[48] However, this collimation can focus the scattered electrons onto the patient's surface, increasing the skin dose. MC simulations performed by our group has shown that this increase is minimal, increasing the skin dose by approximately 4 %. This effect could be minimized or removed with the use of either electric or magnetic fields to deflect the collimated scattered electrons away the patient's surface.

In the electron gun and waveguide, the Lorentz forces on the electrons caused by the MR's fringe magnetic flux densities, unlike in the *perpendicular configuration*, would be significantly reduced. However, because there are some components of the electron trajectories that are transverse to the magnetic fields, such as their trajectories in the electron gun, the linac output would still be adversely affected.

1.5 Research motivation

One of the challenges in the linac-MR integration requires an understanding of the effects of the MR's fringe magnetic flux densities on the linac performance during patient treatment. Although the first prototype had the *perpendicular configuration*, our group has chosen to use the *parallel configuration* in the second linac-MR prototype because of its advantages, which were mentioned in § 1.4.2, over the *perpendicular configuration*. However, the effects of the MR's fringe magnetic flux densities on a *parallel-configured* linac needed to be investigated. These effects were investigated for the *parallel configuration* in this work. Like in the *perpendicular configuration*, the magnetic shield solutions (either passive or active) were investigated as well in order to minimize or eliminate any adverse magnetic field effects, and therefore, recover any lost linac performance caused by the MR's fringe magnetic fields.

1.6 References

[1] W. C. Roentgen. "On a New Kind of Rays," Nature, **53,** 274-276, (1896).

[2] O. Glasser. *Wilhelm Conrad Rontgen and the Early History of the Roentgen Rays* (C. C. Thomas, Illinois, 1934).

[3] H. E. Johns and J. R. Cunningham. *The Physics of Radiology* (C. C. Thomas, Illinois, 1983).

[4] J. V. Dyk. *The Modern Technology of Radiation Oncology* (Medical Physics Publisher, Wisconsin, 1999).

[5] C. A. Perez, L. W. Brady and J. L. Roti. *Principles and Practice of Radiation Oncology*, (Lippincott-Raven, Pennsylvania, 1998).

[6] J. V. Dyk. *The Modern Technology of Radiation Oncology* (Medical Physics Publishing, Wisconsin, 2005)

[7] A. B. Wayte. "Treatment of Some Disorders of the Pituitary by Radiotherapy," Proc R Soc Med, **44,** 450-452, (1951).

[8] W. D. Coolidge. United States Patent Office. (1934) *X-Ray Tube,* US Patent 1946312.

[9] C. C. Ma. "X-Ray Therapy Equipment, Low and Medium Energy." *Encyclopaedia of Medical Devices and Instrumentation*. (2006).

[10] J. S. Laughlin. "Development of the technology of radiation therapy." Radiographics, **9,** 1245-1266, (1989).

[11] G. S. Innes. "The one million volt x-ray therapy equipment at St. Bartholomew's Hospital," Br. J. Radiol., **22 (suppl),** 11-16, (1988).

[12] A. Jones. "The development of megavoltage x-ray therapy at St. Bartholomew's Hospital." Br. J. Radiol., **22 (suppl),** 3-10, (1988).

[13] T. P. Wangler. *RF Linear Accelerators* (Wiley-VCH, Weinheim, 2008).

[14] L. L. Gunderson and J. E. Tepper. *Clinical Radiation Oncology* (Elsevier Churchill Livingstone, Pennsylvania, 2007).

[15] H. E. Johns and J. R. Cunningham. "A precision cobalt 60 unit for fixed field and rotation therapy," Am. J. Roentgenol. Radium Therapy Nuclear Med, **81,** 4-12, (1959).

[16] T. Kitabatake and S. Takahashi. "Conformation Radiotherapy by Means of 6 MeV Linear Accelerator," Tohoku J. exp. Med., **94,** 37-43, (1968).

[17] A. Brahme, J.-E. Roos and I. Lax. "Solution of an integral equation encountered in rotation therapy," Phys. Med. Biol., **27,** 1221, (1982).

[18] A. M. Cormack and R. A. Cormack. "A problem in rotation therapy with x-rays: Dose distributions with an axis of symmetry," Int J Radiat Oncol Biol Phys, **13,** 1921, (1987).

[19] ICRU. , "Prescribing, Recording and Reporting Photon Beam Therapy", ICRU Report 50, (1993).

[20] A. F. Monti, A. Ostinelli, M. Frigerio, et al. "An ICRU 50 radiotherapy treatment chart," Radiother. and Oncol., **35,** 145, (1995).

[21] ICRU. , "Prescribing, Recording and Reporting Photon Beam Therapy (Supplement to ICRU Report 50)", ICRU Report 62, (1999).

[22] T. Nguyen, A. Hoole, S. Thomas, H. Chantler, I. Cowley and N. Burnet. "The use of shifted-isocentre techniques for plan evaluation," *World Congress on Medical Physics and Biomedical Engineering 2006* (IFMBE Proceedings), **14,** 1863-1866, (2007).

[23] M. B. Sharpe, T. Craig and D. J. Moseley. "Image guidance: Treatment target localization systems," Front Radiat Ther Oncol, **40,** 72-93, (2007).

[24] A. Groh, J. H. Siewerdsen, D. G. Drake, J. W. Wong, and D. A. Jaffray. "A performance comparison of flat-panel imager-based MV and kV cone-beam CT," Med. Phys., **29**, 967-975, (2002).

[25] S. Balter and J. M. Balter. "Anniversary Paper: A sampling of novel technologies and the role of medical physicists in radiation oncology," Med. Phys., **35,** 5641-5652, (2008).

[26] J. Leong. "Use of digital fluoroscopy as an online verification device in radiation-therapy," Phys. Med. Biol., **31,** 985-992, (1986).

[27] L. E. Antonuk, J. Boudry, W. Huang, et al. "Demonstration of megavoltage and diagnostic x-ray imaging with hydrogenated amorphous silicon arrays," Med. Phys., **19,** 1455-1466, (1992).

[28] D. A. Jaffray, J. H. Siewerdsen, G. K. Edmundson, J. W. Wong and A. A. Martinez. "Flat-panel cone-beam CT on a mobile isocentric C-arm for image-guided brachytherapy," Proc. SPIE Physics of Medical Imaging, **4682,** 209-217, (2002).

[29] D. A. Jaffray, D. G. Drake, M. Moreau, A. A. Martinez and J. W. Wong. "A radiographic and tomographic imaging system integrated into a medical linear accelerator for localization of bone and soft-tissue targets," Int J Radiat Oncol Biol Phys, **45,** 773, (1999).

[30] J. A. Purdy. "From new frontiers to new standards of practice: Advances in radiotherapy planning and delivery," Front Radiat Ther Oncol, **40,** 18-39, (2007).

[31] H. Shirato, T. Harada, T. Harabayashi, et al. "Feasibility of insertion/implantation of 2.0-mm-diameter gold internal fiducial markers for precise setup and real-time tumor tracking in radiotherapy," Int J Radiat Oncol Biol Phys, **56,** 240, (2003).

[32] D. A. Jaffray. "Kilovoltage volumetric Imaging in the treatment room," Front Radiat Ther Oncol, **40,** 116-131, (2007).

[33] C. Ozhasoglu, C. B. Saw, H. Chen, et al. "Synchrony - Cyberknife Respiratory Compensation Technology," Medical Dosimetry, **33,** 117, (2008).

[34] Y. Otani, I. Fukuda, N. Tsukamoto, et al. "A comparison of the respiratory signals acquired by different respiratory monitoring systems used in respiratory gated radiotherapy," Med. Phys., **37,** 6178-6186, (2010).

[35] B. G. Fallone, B. Murray, S. Rathee, et al. "First MR images obtained during megavoltage photon irradiation from a prototype integrated linac-MR system," Med. Phys., **36,** 2084-2088, (2009).

[36] J. G. M. Kok, B. W. Raaymakers, J. J. W. Lagendijk, J. Overweg, C. H. W. de Graaff and K. J. Brown. "Installation of the 1.5 T MRI accelerator next to clinical accelerators: impact of the fringe field," Phys. Med. Biol., **54,** N409-N415, (2009).

[37] J. F. Dempsey, D. Benoit, J. R. Fitzsimmons, et al. "A Device for Realtime 3D Image-Guided IMRT," Int J Radiat Oncol Biol Phys, **63,** S202-S202, (2005).

[38] B. W. Raaymakers, J. J. W. Lagendijk, J. Overweg, et al. "Integrating a 1.5 T MRI scanner with a 6 MV accelerator: proof of concept," Phys. Med. Biol., **54,** N229, (2009).

[39] C. Kirkby, T. Stanescu, S. Rathee, M. Carlone, B. Murray and B. G. Fallone. "Patient dosimetry for hybrid MRI-radiotherapy systems," Med. Phys., **35,** 1019-1027, (2008).

[40] C. Kirkby, B. Murray, S. Rathee and B. G. Fallone. "Lung dosimetry in a linac-MRI radiotherapy unit with a longitudinal magnetic field," Med. Phys., **37,** 4722-4732, (2010).

[41] B. Burke, B. G. Fallone and S. Rathee. "Radiation induced currents in MRI RF coils: application to linac/MRI integration," Phys. Med. Biol., **55,** 735, (2010).

[42] J. S. Aubin, S. Steciw and B. G. Fallone. "Effect of transverse magnetic fields on a simulated in-line 6 MV linac," Phys. Med. Biol., **55,** 4861, (2010).

[43] J. St. Aubin, D. M. Santos, S. Steciw and B. G. Fallone. "Effect of longitudinal magnetic fields on a simulated in-line 6 MV linac," Med. Phys., **37,** 4916-4923, (2010).

[44] J. Yun, J. St. Aubin, S. Rathee and B. G. Fallone. "Brushed permanent magnet DC MLC motor operation in an external magnetic field," Med. Phys., **37,** 2131-2134, (2010).

[45] J. St. Aubin, S. Steciw and B. G. Fallone. "Waveguide detuning caused by transverse magnetic fields on a simulated in-line 6 MV linac," Med. Phys., **37,** 4751-4754, (2010).

[46] J. St. Aubin, S. Steciw and B. G. Fallone. "Magnetic decoupling of the linac in a low field biplanar linac-MR system," Med. Phys., **37,** 4755-4761, (2010).

[47] A. J. E. Raaijmakers, B. Hårdemark, B. W. Raaymakers, C. P. J. Raaijmakers, J. J. W. Lagendijk. "Dose optimization for the MRI-accelerator: IMRT in the presence of a magnetic field," Phys. Med. Biol., **52**, 7045-7054, (2007).

[48] S. A. Naqvi, X. A. Li, S. W. Ramahi, J. C. Chu and S. Ye. "Reducing loss in lateral charged-particle equilibrium due to air cavities present in x-ray irradiated media by using longitudinal magnetic fields," Med. Phys., **28,** 603-611, (2001).

CHAPTER 2 : BASIC BACKGROUND

2.1 Magnetostatics

Magnetism began as the study of the mechanical attraction of iron to lodestone, which a primarily made of iron oxides.[1] Its name was derived from Magnesia, a region in Asia Minor.[1] Although, it is not apparent with permanent magnets and with the initial study of magnetism, magnetism involves moving charges or a current and can be summarized into two simplified statements. Firstly, moving charges or a current creates a magnetic field around it.[2] This statement drives the analytic calculations for the 3D magnetic fields of a current loop which will be discussed later in § 2.1.2 and § 2.1.3. Secondly, magnetic fields exerts magnetic forces on a moving charge or a current that is perpendicular to its motion;[2] the magnetic force is discussed in § 2.1.4. Because the linac uses an electron beam to produce the treatment beam, as discuss in § 1.5, knowing these magnetic forces and how they affect the electron beam is important in understanding how magnetic fields will affect the linac performance.

On a side note, it would be useful to present an explanation of the notation for the magnetic flux density **B** and the magnetic field **H**. The fields **B** and **H** are both magnetic fields. The difference between the two values is their sources. The field **H** is the magnetic fields that arises from only free currents (conduction or convection currents) while **B** is the magnetic fields that arises from the sum of both the free currents and the magnetization **M** of the magnetic material. To fall in line with the literature, **H** will be referred to as the magnetic field while **B** will be referred to as the magnetic flux density.

2.1.1 Biot-Savart Law

In magnetostatics, the current density **J** discussed in § 2.1 is assumed to be constant in time[1] (Eq. 2.1) and is called a steady current.

$$\nabla \cdot \mathbf{J}=0 \qquad 2.1$$

Its magnetic flux density **B** is calculated through the Biot-Savart law[3] given by Eq. 2.2.

$$\mathbf{B}(\mathbf{r})=\frac{\mu_0}{4\pi}\int \frac{\mathbf{J}(\mathbf{r}')\times\mathbf{R}}{R^2}\,d\tau' \qquad 2.2$$

In Eq. 2.2, μ_o is the permeability of free space, **r** and **r'** are the test points and current source, respectively. Thus, τ' is a dummy integration variable, and **R** is a vector from the current source to the point of calculation for **B**. It can be shown that Eq. 2.2 has no divergence (Eq. 2.3) and its curl is calculated by Ampère's Law Eq. 2.4.

$$\nabla \cdot \mathbf{B}=0 \qquad 2.3$$

(Ampère's Law) $$\nabla \times \mathbf{B} = \mu_0 \mathbf{J}(\mathbf{r}) \qquad 2.4$$

Eqs 2.3 and 2.4 are the Maxwell's equations for magnetostatics.[3] By satisfying Eq. 2.3 and 2.4, the magnetic flux density calculated from Eq. 2.2 are guaranteed to be physically realistic.

Because the Biot-Savart law (Eq. 2.2) satisfies Eq. 2.3, a magnetic vector potential **A** can be introduce by the Helmholtz theorem[1,3] such that **A** is a divergent-less fields (Eq. 2.5). **B** can then be calculated by taking the curl of **A** (Eq. 2.6).

$$\nabla \cdot \mathbf{A}=0 \qquad 2.5$$

$$\mathbf{B}=\nabla \times \mathbf{A} \qquad 2.6$$

However, **A** is not unique for a given **B**. Like the scalar potential from electrostatics,[1,3] there is freedom to add any function whose curl vanishes. This freedom in **A** provides some convenience in the analytical calculations of **B**. By using Eq. 2.6 into Eq. 2.4, Eq. 2.4 will become Eq. 2.7, which is a vector formulation of n Poisson's equations for n dimensions.[3]

$$\nabla^2 \mathbf{A} = -\mu_0 \mathbf{J} \qquad 2.7$$

When **J** is set to vanish at infinity, the solution for Eq. 2.7 gives the magnetic vector potential **A** in the form of Eq. 2.8.[3]

$$\mathbf{A}(\mathbf{r}) = \frac{\mu_0}{4\pi} \int \frac{\mathbf{J}(\mathbf{r'})}{R} d\tau' \qquad 2.8$$

In Eq. 2.8, **A** is a function of the test point **r**, **J** is a function of the current source point **r'**, R is the length between **r** and **r'**, and τ' is a dummy variable used for integration.

2.1.2 Vector potential of a current loop

For the following two sections, Eq. 2.8 will be used to calculate the 3D magnetic flux density of a current loop. This specific application will be used later in CHAPTER 4 to build a 3D MR's fringe magnetic field model.

When the current density **J** in Eq. 2.2 and 2.8 is a line current flowing along a wire, **J** can be replaced by *Id***l**. The wire is made infinitely thin so that the effects of the wire on **B** can be ignored. Thus, I is the magnitude of the current flowing in the wire which is assumed to be constant, while $d\mathbf{l}$ gives the direction of the current flow. Therefore, Eq. 2.8 then becomes Eq. 2.9.

$$\mathbf{A}(\mathbf{r}) = \frac{\mu_0 I}{4\pi}\int \frac{d\mathbf{l}}{R} \qquad 2.9$$

Furthermore, both ends of the wire are put together such that the wire forms a circular ring with a radius a. The current $Id\mathbf{l}$ now flows in a close loop forming the current loop. For a general solution, this current loop is suspended above the xy-plane by a distance h (Fig. 2.1).

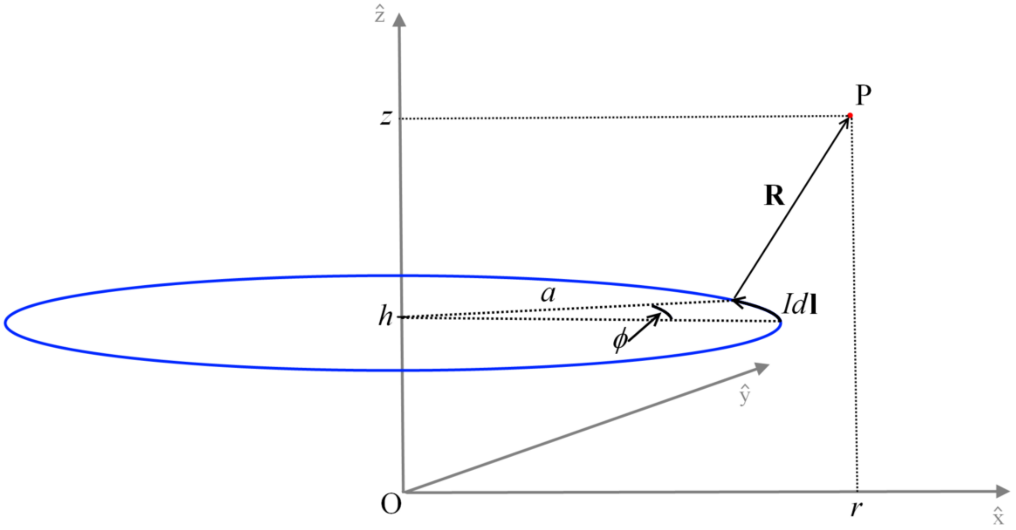

Figure 2.1: The setup for the current loop where B is calculated on the test point P.

If the test point P where **B** is to be calculated is on the xz-plane, it has the co-ordinates (r, 0, z), and R and $d\mathbf{l}$ are given by Eq. 2.10 and Eq. 2.11, respectively.

$$R = \sqrt{(r+a)^2 + (z-h)^2 - 4ra\left(\frac{1+\cos\phi}{2}\right)} \qquad 2.10$$

$$d\mathbf{l} = \mathrm{a}(-sin\phi\hat{\boldsymbol{x}} + cos\phi\hat{\boldsymbol{y}})d\phi \qquad 2.11$$

In Fig. 2.1, ϕ is in the azimuthal direction. When Eq. 2.10 and Eq. 2.11 are substituted into Eq. 2.9, **A** becomes Eq. 2.12.

$$\mathbf{A}(\mathbf{r},\mathbf{z}) = \frac{\mu_0 aI}{4\pi}\int_0^{\pi} \frac{cos\phi d\phi}{\sqrt{(r+a)^2 + (z-h)^2 - 4ra\left(\frac{1+cos\phi}{2}\right)}}\hat{\boldsymbol{y}} \qquad 2.12$$

Because of the cylindrical symmetry of the current loop, Eq. 2.12 can be generalized for all cases (Eq. 2.13) in cylindrical coordinates by replacing $\hat{\boldsymbol{y}}$ with $\hat{\boldsymbol{\phi}}$, which is the unit vector in the azimuthal direction.

$$\mathbf{A}(r,z) = \frac{\mu_0 aI}{4\pi}\int_0^{\pi} \frac{cos\phi d\phi}{\sqrt{(r+a)^2 + (z-h)^2 - 4ra\left(\frac{1+cos\phi}{2}\right)}}\hat{\boldsymbol{\phi}} \qquad 2.13$$

In order to make more simplification to Eq. 2.12, a new variable α is introduced so that $\phi = \pi - 2\alpha$ and $d\phi = -2d\alpha$. Therefore, $cos\phi$ becomes $-cos(2\alpha)$ through the difference trigonometric identity.[4] By using the half-angle trigonometric identity,[4] $cos\phi$ becomes Eq. 2.14.

$$cos\phi = -(1 - 2sin^2\alpha) \qquad 2.14$$

When Eq. 2.14 is solved for $sin^2\alpha$ and substituted into Eq. 2.10, Eq. 2.10 can be simplified into Eq. 2.15 where k is given by Eq. 2.16.

$$R = \frac{2}{k}\sqrt{ra}\sqrt{1 - k^2 sin^2\alpha} \qquad 2.15$$

$$k \equiv \sqrt{\frac{4ra}{(z-h)^2 + (r+a)^2}} \qquad 2.16$$

Using Eqs 2.14, 2.15, and 2.16 in Eq. 2.13, a new expression for **A** is given (Eq. 2.17).

$$\mathbf{A} = \frac{\mu_0 I k}{4\pi}\sqrt{\frac{a}{r}}\left[2\int_0^{\pi/2}\frac{sin^2\alpha d\alpha}{\sqrt{1-k^2 sin^2\alpha}} + \int_0^{\pi/2}\frac{d\alpha}{\sqrt{1-k^2 sin^2\alpha}}\right]\hat{\boldsymbol{\phi}} \qquad 2.17$$

The integral in the second term of Eq. 2.17 is in the form of the complete elliptic integral of the first kind[5] *K*(*k*) (Eq. 2.18). On the other hand, the integral in the first term is a linear combination[1] (Eq. 2.20) of the complete elliptic integral of the first and second[5] kind *E*(*k*) (Eq. 2.19).

$$K(k) = \int_0^{\pi/2}\frac{d\alpha}{\sqrt{1-k^2 sin^2\alpha}} \qquad 2.18$$

$$E(k) = \int_0^{\pi/2}\sqrt{1-k^2 sin^2\alpha}\, d\alpha \qquad 2.19$$

$$\frac{1}{k^2}[K(k) - E(k)] = \int_0^{\pi/2}\frac{sin^2\alpha d\alpha}{\sqrt{1-k^2 sin^2\alpha}} \qquad 2.20$$

In Eqs. 2.18 and 2.19, *K*(*k*) and *E*(*k*) has a value of $\frac{\pi}{2}$ when k=0.[5] As k reaches $\frac{\pi}{2}$, *K*(*k*) becomes infinite[5] while *E*(*k*) becomes unity.[5] When Eqs 2.18 and 2.20 is used in Eq. 2.17, the final form on the vector potential **A** (Eq. 2.21) is obtained after performing additional simplifications.

$$\mathbf{A}(r) = \frac{\mu_0 I}{2\pi}\sqrt{\frac{a}{r}}\left[\left(\frac{2}{k} - k\right)K(k) - \frac{2}{k}E(k)\right]\hat{\boldsymbol{\phi}} \qquad 2.21$$

2.1.3 B-field of a current loop

Once the vector potential **A** is known, **B** can be calculated by applying Eq. 2.6 on Eq. 2.21, which is shown in Eq. 2.22.

$$\mathbf{B}(r,z) = -\frac{\partial A_\phi}{\partial z}\hat{\boldsymbol{r}} + \frac{1}{r}\frac{\partial r A_\phi}{\partial r}\hat{\boldsymbol{z}} \qquad 2.22$$

As shown by Eq. 2.22, **B** does not have an azimuthal component since the current in the current loop flows along the loop which is in the azimuthal direction. Because the current direction is used in the cross product in Eq. 2.2**,** **B** would be perpendicular to the current direction.

$$\mathbf{B}(r,z) = \frac{\mu_0 I k}{4\pi\sqrt{ar}}\left[\frac{-(z-\mathrm{h})}{r}\left(K(k) - \frac{2-k^2}{2\left(1-k^2\right)}E(k)\right)\hat{\boldsymbol{r}} + \left(K(k) + \frac{k^2(r+a)-2r}{2r\left(1-k^2\right)}E(k)\right)\hat{\boldsymbol{z}}\right] \qquad 2.23$$

When Eq. 2.22 is applied to Eq. 2.21, **B** simplifies into Eq. 2.23 in Telsa. In Eq. 2.23, $\hat{\boldsymbol{r}}$ and $\hat{\boldsymbol{z}}$ are the radial and longitudinal unit vectors, respectively. Eq. 2.23 has a singularity at r=0, because of the variable r in its denominator. Therefore, this r needs to be eliminated. Remembering that k is a function of both r and z, the r in the denominator of Eq. 2.23 can be eliminated by substituting Eq. 2.16 for k in Eq. 2.23. The radial, B_r, and longitudinal, B_z, components of the magnetic flux density simplifies into Eq. 2.24 and Eq. 2.25, where α is an integration variable.

$$B_r(r,z) = -\frac{\mu_0 I(\mathrm{z}-h)a}{\pi\sqrt{((z-h)^2+(r+a)^2)^3}\left(1-k^2\right)}\left[2\int_0^{\pi/2}\frac{sin^2\alpha-1}{\sqrt{1-k^2 sin^2\alpha}}d\alpha + E(k)\right] \qquad 2.24$$

$$B_z(r,z) = \frac{\mu_0 I}{2\pi\sqrt{(z-h)^2+(r+a)^2}}\left[K(k) + \left(\frac{2(r+a)a}{((z-h)^2+(r+a)^2)\left(1-k^2\right)} - \frac{1}{1-k^2}\right)E(k)\right] \qquad 2.25$$

2.1.4 Magnetic Force

When a charged particle, with a charge q and a velocity **v**, traverses through **B**, this particle will experience a force that is perpendicular to its motion. This magnetic force $\mathbf{F}_{\mathrm{mag}}$ is calculated by Eq. 2.26 as the cross-product of the charged particle's motion and **B**.[3]

$$\mathbf{F}_{\text{mag}} = q\mathbf{v} \times \mathbf{B} \qquad 2.26$$

Now suppose that the charged particle above is part of a charge distribution that is traveling along a wire, Eq. 2.26 will need to be integrated for the entire charge distribution. When this charge distribution is thought of as the line current $Id\mathbf{l}$, Eq. 2.26 can be rewritten as Eq. 2.27. In Eq. 2.27, I is outside of the integral because I is assumed to be constant in magnitude throughout the wire.[3]

$$\mathbf{F}_{\text{mag}} = I\int (d\mathbf{l} \times \mathbf{B}) \qquad 2.27$$

When two current loops are put side by side along their symmetric axis (Fig. 2.2), each current loop experiences a magnetic flux density that was produced by the other current loop. Therefore, there will be a magnetic force exerted on each current loop dictated by Eq. 2.27, where I and $d\mathbf{l}$ are the current magnitude and direction from the current loop and $\mathbf{B}$ is the magnetic flux density experienced by the current loop.

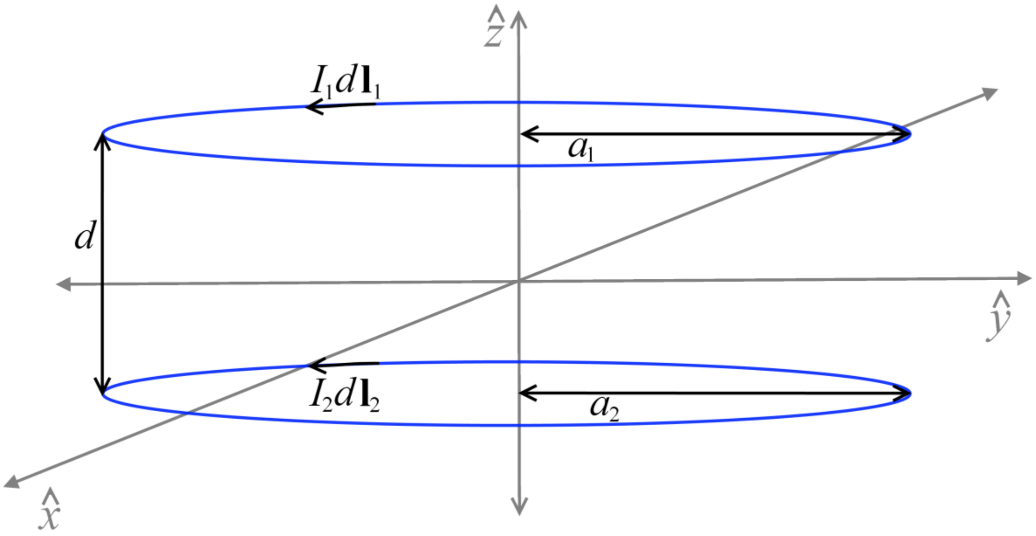

Figure 2.2: A pair of current loop. The top loop has current $I_1 d\mathbf{l}_1$ and a radius a_1 while the bottom loop has current $I_2 d\mathbf{l}_2$ and a radius a_2. d is the separation distance between the two current loops.

If B_{r2} and B_{z2} is the radial and longitudinal components of $\mathbf{B}_2$ produced by the bottom current loop in Fig. 2.2, the top current loop (which has a current of $I_1 d\mathbf{l}_1$ and a radius of a_1) will experience a magnetic force $\mathbf{F}_{21}$ (Eq. 2.28).

$$\mathbf{F}_{21} = I_1 a_1 \left(\int_0^{2\pi} d\phi_1 \right) (B_{z2}\hat{\boldsymbol{r}} - B_{r2}\hat{\boldsymbol{z}}) \qquad 2.28$$

Because of the cylindrical symmetry in the $\mathbf{B}_2$, $\mathbf{B}_2$ has no dependence on ϕ, which is in the azimuthal direction. Once the integration in Eq. 2.28 is completed, Eq. 2.28 becomes Eq. 2.29 which gives the magnetic force $\mathbf{F}_{21}$ experienced by the top current loop.

$$\mathbf{F}_{21} = 2\pi I_1 a_1 (B_{z2}\hat{\boldsymbol{r}} - B_{r2}\hat{\boldsymbol{z}}) \qquad 2.29$$

2.2 External magnetic fields in matter

2.2.1 The magnetic field H

The current **J** in Ampère's Law (Eq. 2.4) can be divided into the conventional current density $\mathbf{J}_\mathrm{c}$ and the magnetization current density $\mathbf{J}_\mathrm{m}$,[1] which is shown in Eq. 2.30.

$$\nabla \times \mathbf{B} = \mu_0(\mathbf{J}_\mathrm{c} + \mathbf{J}_\mathrm{m}) \qquad 2.30$$

In Eq. 2.30, $\mathbf{J}_\mathrm{c}$ encompasses both the convection current and the conduction current.[1] Furthermore, $\mathbf{J}_\mathrm{m}$ consist of the volumetric current that arises from magnetization **M** of the material (Eq. 2.31), which is the sum of all the individual atomic or molecular magnetic dipole moments **m** in the magnetic material (Eq. 2.32).

$$\mathbf{J}_\mathrm{m} = \nabla \times \mathbf{M} \qquad 2.31$$

$$\mathbf{M}=N\mathbf{m} \qquad 2.32$$

In Eq. 2.32, N in number of atoms or molecules per cubic meter in the material.[1] When Eq. 2.31 is substituted in Eq. 2.30, Eq. 2.30 becomes Eq. 2.33 while the new quantity **H** (Eq. 2.34) is defined as the magnetic field. It is caused by only free current and has units of $\frac{A}{m}$.

$$\nabla \times \left(\frac{1}{\mu_0}\mathbf{B} - \mathbf{M}\right) = \mathbf{J}_\mathrm{c} \qquad 2.33$$

$$\mathbf{H} = \left(\frac{1}{\mu_0}\right)\mathbf{B} - \mathbf{M} \qquad 2.34$$

Furthermore, **H** is only proportional to the conventional current density $\mathbf{J}_\mathrm{c}$ (from Eq. 2.33 and 2.34), which is easy to measure. Thus, **M** can be set to Eq. 2.35

because **H** is easier to measure than **B.** When **M** is substituted back into Eq. 2.34, a constitutive relation for **B** and **H** is obtained (Eq. 2.36).

$$\mathbf{M} = \chi_m \mathbf{H} \qquad 2.35$$

$$\mathbf{B} = (1 + \chi_m)\mu_0 \mathbf{H} \qquad 2.36$$

In Eq. 2.36, χ_m is the magnetic susceptibility of the material. When $(1 + \chi_m)$ is set to the relative permeability μ_r, the final form of the constitutive relation is obtained (Eq. 2.37).

$$\mathbf{B} = \mu_\mathrm{r}\mu_0 \mathbf{H} \qquad 2.37$$

2.2.2 Diamagnetism

Diamagnetism is a type of magnetism that is associated with a pair of coupled the electron's orbital angular momenta.[1-3] When no external magnetic field is present, the atomic or molecular magnetic moments **m** in a diamagnetic material will be oriented randomly, which results in no net **M** in the material. Therefore, the material will have no magnetic field. An external magnetic field will cause this individual atomic or molecular **m** to align parallel to each other and anti-parallel to the external magnetic field.[2,3] Diamagnetic materials are characterized by a μ_r of less than unity and, consequently, a negative χ_m.[1-3] Since diamagnetism is an electron contribution, it is present in all matter; however, its effect is very weak and is negligible when other types of magnetism is present.[2]

2.2.3 Paramagnetism

Like diamagnetism, paramagnetism is an atomic or molecular phenomenon. However, it is associated with unpaired electron.[2] The atomic or molecular **m** in the paramagnetic material are oriented randomly as well when no external magnetic field is present. An external magnetic field will cause these atomic or molecular **m** to align parallel to each other and the external magnetic field.[1] Compared to ferromagnetism (discussed in § 2.2.4), paramagnetism is still very weak. Paramagnetic materials have μ_r that on the order of unity and χ_m of less than unity.[1-3]

2.2.4 Ferromagnetism

The last type of magnetism that will be discussed in this chapter is ferromagnetism. Like paramagnetism, ferromagnetism involves the atomic magnetic dipoles **m** of unpaired electrons in the material.[3] Because of the stronger interactions between these dipoles, they spontaneously align parallel to each other, creating a net magnetization **M**. These dipole alignments, however, only occur in many small regions in the material called magnetic domains. There is no large scale magnetization that occurs because the many domains in the material are oriented in a random fashion[3] when no external magnetic field is present. Ferromagnetic effects can be 10^5 times greater than that of diamagnetism and paramagnetism.

When an external magnetic field **H** is present on the ferromagnetic material, **B** has a non-linear response to **H** (Fig. 2.3) in ferromagnetic materials.

The curve in Fig. 2.3 is a representative magnetization curve of a ferromagnetic material. As **H** is increased, more of the magnetic domains in the material becomes oriented parallel to **H**. When all of the magnetic domains become parallel to **H**, the ferromagnetic material is said to be magnetically saturated and **B** remains constant as **H** is increased. The horizontal asymptote seen in Fig. 2.3 is an evidence of the magnetic saturation of a ferromagnetic material.

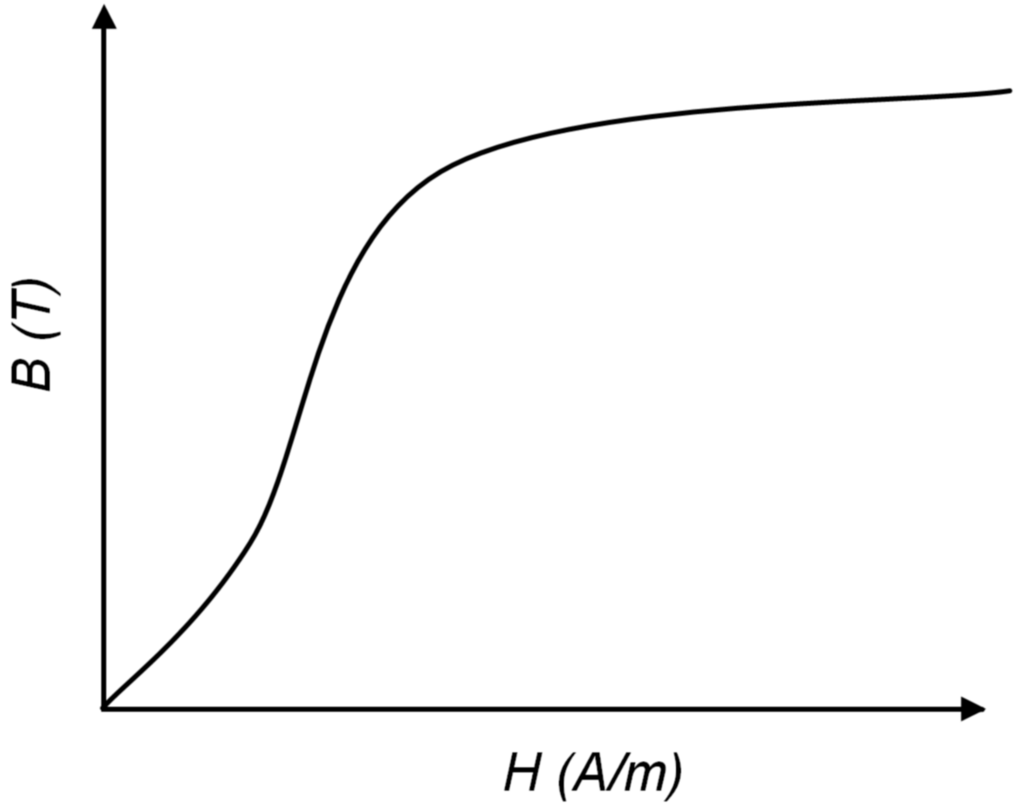

Figure 2.3: A representative magnetization curve for a ferromagnetic substance.

To obtain the curve in Fig. 2.3 from an unmagnetized ferromagnetic substances, **H** is increased monotonically starting from zero while the **B** is the response of the material to the applied field **H**.[1] The slope of the magnetization curve is the permeability μ (or μ_r if μ_0 is factored out of the slope) from Eq. 2.37. Both μ and

μ_r are not constant and μ_r can be large (>1000) depending on which value of **H** is used. Because **B** is dependent of the material (Eq. 2.30), μ_r will be different for different ferromagnetic materials. For example, the μ_r for steel can be as large as 1247.[6]

2.3 RF linear accelerators (linacs)

Particle accelerators such as linacs deliver energy to charged-particles through the use of electric fields.[7] The early accelerators use electrostatic fields, which meant that the energy gained by the charged particle was equal to the particle charge times the potential drop in the accelerator.[7] The maximum energy transferred to the charge particle by this kind of accelerators cannot exceed this product. Because the potential drop in the early accelerators was limited to less than 10 MV by electric breakdown,[7] this puts a limitation on the maximum energy that a charge particle can gain from these early accelerators. In order to increase the maximum energy transferred to a charge particle, RF accelerators which use time-varying electric fields to deliver energy to and accelerate charge particles are used.

2.3.1 Electron gun

Depending on the application, particle accelerators can accelerate different types of charged-particles such as electrons, protons, and carbon ions. The charged particle used in medical linacs is the electron, where the source of the electrons comes from the *electron gun* (also called an *electron injector*). In the *electron gun*, electrons pass through a resistive cathode usually made of tungsten and are ejected from the cathode when they have enough energy to overcome the cathode's work function. Since the cathode is kept at a low potential, the thermionically emitted electrons are accelerated and focussed via an electric lens onto the anode (high potential), at which points the electron beam is injected into the linac waveguide. The electric lens consists of electric fields which are shaped according to the shape of the electron gun's focussing electrodes.[8] The geometric shape and design of the electron gun depends of the needs of the application it is used in. For this project, the electron gun is based of Pierce-diode electron gun[8,9] (Fig. 2.4).

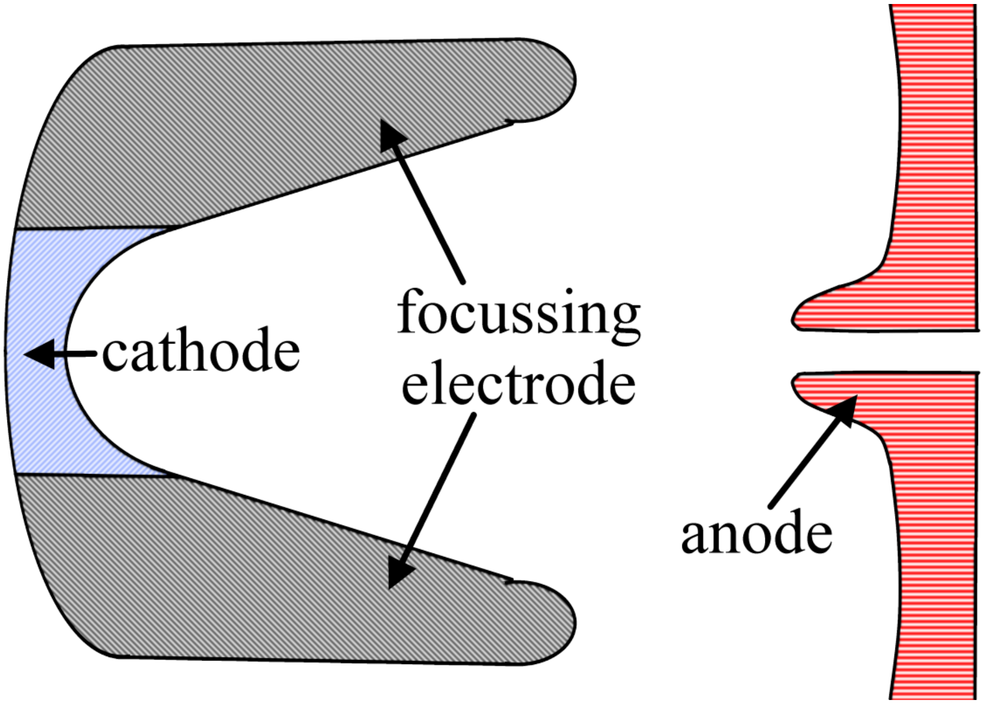

Figure 2.4: A schematic diagram showing a cross-sectional view of a Pierce-diode electron gun.

The amount of thermionic cathode emission increases as the temperature of the cathode increases. When there are a large amount of electron emitted from the cathode, a cloud of electrons, surrounding the cathode, forms a negatively charge region directly in front of the cathode; this causes some of the emitted electrons to be repelled back to cathode.[10] This cloud of electrons is called the space-charge. When a sufficiently large space-charge is formed, the thermionic cathode emission no longer increases as the cathode temperature increases. At this point, the electron gun is said to be space-charge limited. Child's Law (Eq. 2.38) can be used to describe the electron current density j_e when the electron gun is space-charge limited.[9,11-13]

$$j_e = \frac{4\varepsilon_0}{9}\sqrt{\frac{2e}{m_e}}\frac{V^{3/2}}{d_{CL}^2} \tag{2.38}$$

In Eq. 2.38, ε_0 is the permittivity of free space, m_e is the electron mass, e is the electron charge, V and d_{CL} are the potential difference and the distance, respectively, between the cathode and anode.

A second emission model, the Fowler-Nordheim field emission model, can be used for more accurate electron current density calculation.[14] However, a comparison between these two emission models show a difference of less than 1 %.[8,15] To use the Fowler-Nordheim field emission model however, the cathode's temperature and work function are required.[15] When the cathode temperature is high enough to be space-charge limited, both Child's Law and the Fowler Nordheim field emission models give the same result. In this work, the cathode temperature is an unknown. However, the electron gun used for this work is space-charge limited; therefore, Child's Law was the cathode emission model used for this work.

2.3.2 Electromagnetic Theory

The theory of both electricity and magnetism is unified in the electromagnetic theory. When time-varying electric fields **E** and time-varying **B** are present, every phenomenon in classical electromagnetism can be summarized into the Maxwell's equations (Eq. 2.39-2.42). Ampère's Law from Eq. 2.4 is modified by adding a term with the electric displacement **D** in Eq. 2.42. Furthermore, **D** and **E** are related to each other through the constitutive relation in Eq. 2.43. Eq. 2.39 2.42 occur in matter and therefore uses both **D** and **E** and both **H** (Eq. 2.37) and **B**.

(Gauss's Law)

$$\nabla \cdot \mathbf{D} = \frac{\rho}{\varepsilon_0} \qquad 2.39$$

$$\nabla \cdot \mathbf{B} = 0 \qquad 2.40$$

(Faraday's Law)

$$\nabla \times \mathbf{E} = -\frac{\partial \mathbf{B}}{\partial t} \qquad 2.41$$

(Ampère's Law)

$$\nabla \times \mathbf{H} = \mathbf{J}_{\mathrm{c}} + \frac{\partial \mathbf{D}}{\partial t} \qquad 2.42$$

$$\mathbf{D} = \varepsilon_r \varepsilon_0 \mathbf{E} \qquad 2.43$$

In Eq. 2.43, ε_r and ε_0 are the relative permittivity of the material and the permittivity of free space, respectively.

In the Maxwell's equations, a time varying **B** can be the source for **E**. In addition, a time-varying **E** (or **D**) can be the source for **B** (or **H**). The electric fields and magnetic flux density of a propagating electromagnetic (EM) wave (RF waves) with a frequency ω and wavenumber k_{z0} have the form described in

Eq. 2.44 and Eq. 2.45, respectively. The direction of propagation of the waves described in Eqs 2.44 and 2.45 along the *z*-axis.

$$\mathbf{E} = E_0 e^{i(\omega t - k_{z0} z)} \hat{\mathbf{z}} \qquad 2.44$$

$$\mathbf{B} = B_0 e^{i(\omega t - k_{z0} z)} \hat{\mathbf{z}} \qquad 2.45$$

In Eqs 2.44 and 2.45, E_0 and B_0 are the initial amplitudes of the electric fields and magnetic flux density, respectively. A force law is needed to describe the effects of these electric and magnetic waves on charged-particles. By adding the electric force onto the magnetic force in Eq. 2.26, the complete force law (called the Lorentz force **F**) for electromagnetism is obtained (Eq. 2.46). Eq. 2.46 shows that the electric force acts on a charged-particle parallel to its trajectory while the magnetic force acts on a charged-particle perpendicular to its trajectory.

$$\mathbf{F} = q(\mathbf{E} + \mathbf{v} \times \mathbf{B}) \qquad 2.46$$

The coupled **E** and **B** in Eq. 2.39-2.42 are often cumbersome and difficult to work with. In a source-less and current-less case, taking the curl of Eq. 2.41 and using Eqs 2.37, 2.39, 2.42, 2.43, and 2.44 gives a de-coupled second order partial differential equation (PDE) for **E** (Eq. 2.47). Likewise, taking the curl of Eq. 2.42 and using Eqs 2.37, 2.40, 2.41, 2.43, and 2.45, a de-coupled second order PDE for **B** (Eq. 2.48) is obtained. Eqs 2.47 and 2.48 are in the form of the Helmholtz equation, a second order elliptic PDE.[16]

$$\nabla^2 \mathbf{E} + k_0^2 \mathbf{E} = 0 \qquad 2.47$$

$$\nabla^2 \mathbf{B} + k_0^2 \mathbf{B} = 0 \qquad 2.48$$

$$k_0^2 = \mu_r \mu_0 \varepsilon_r \varepsilon_0 \omega^2 = \frac{\omega^2}{v^2} \qquad 2.49$$

In Eqs 2.47-2.49, k_0 is the free space wavenumber.[17]

2.3.3 Waveguides

Waveguides are structures that contain and direct the flow of propagating RF waves. Waveguides in linacs are used to transfer electromagnetic energy from the electric fields of an RF wave to a charged-particle beam such as the electron beam of a linac.[17] Either a travelling-wave or a standing-wave can be used for particle acceleration. The waveguide's design depends on the type of RF wave used for acceleration. A travelling-wave waveguide (Fig. 2.5a) will have only forward travelling RF wave.[18] Only one out of every four cavity is capable of particle acceleration.[18] For travelling-wave waveguides, a resistive load is used to absorb the out-going RF waves. A standing-wave waveguide (Fig. 2.5b) will have forward and backward travelling RF waves.[18] Both ends of a standing-wave waveguide are short circuited, so the RF waves have hard reflections. The standing-waves will vary in magnitude with time; however, they will be partially stationary in phase.[18] Although all of the standing-wave waveguide's cavities can accelerate charge-particles,[18] only the forward travelling RF waves in each cavity can successfully accelerate a charge-particle.[18] The waveguide used in this project is a standing-wave waveguide; therefore, this document will only deal with standing-wave waveguide.

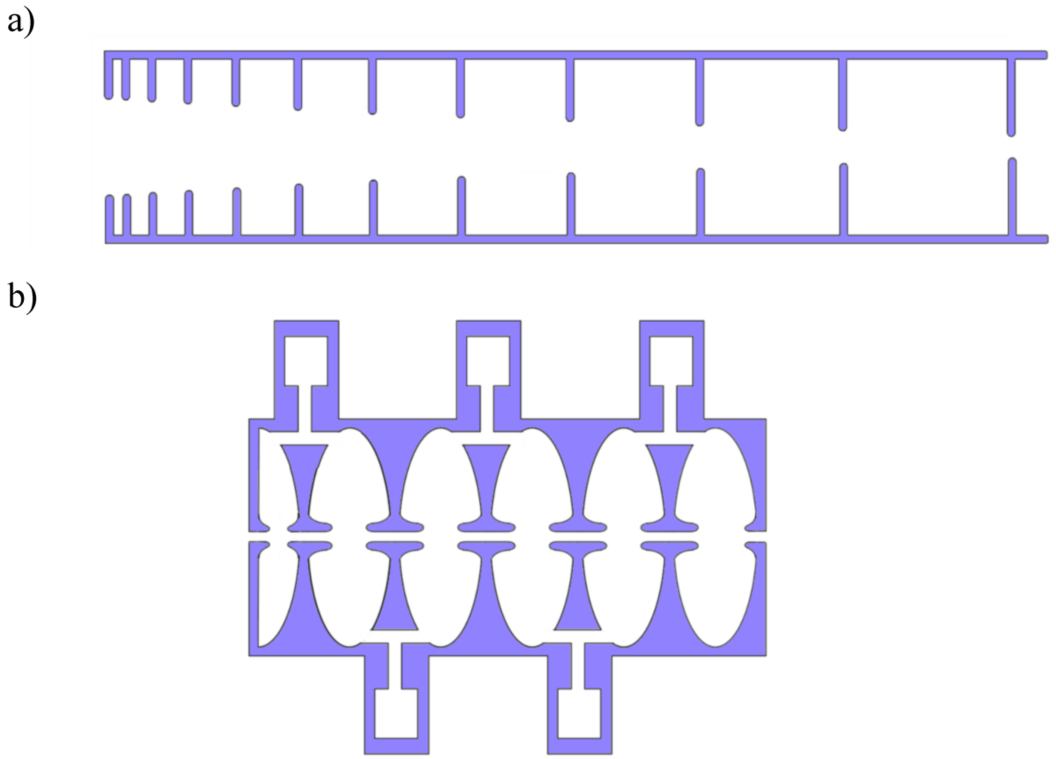

Figure 2.5: A schematic diagram of a) a forward travelling-wave waveguide[18] and b) a standing-wave waveguide.[8,18]

The solution to the Maxwell's equations (or the resulting Helmholtz equations) will only be unique when the boundary conditions are specified. For an ideal conductor, the tangential electric field and the normal magnetic field are zero at the waveguides walls.[7] In addition, Eqs 2.50-2.53 must also be satisfied at the walls of the waveguide.[7]

$$\hat{\boldsymbol{n}} \cdot \mathbf{E} = \frac{\Sigma}{\varepsilon_0} \tag{2.50}$$

$$\hat{\boldsymbol{n}} \times \mathbf{H} = \mathbf{K} \tag{2.51}$$

$$\hat{\boldsymbol{n}} \cdot \mathbf{B} = 0 \tag{2.52}$$

$$\hat{\boldsymbol{n}} \times \mathbf{E} = 0 \tag{2.53}$$

So, $\hat{n}$ is the unit vector normal to the waveguide's walls, **K** is the surface current density, and Σ is the surface charge density. For an ideal conductor, there is a sharp cut-off in the RF wave's electric and magnetic fields at the conductor's surface. However, metals such as copper are not ideal conductors although they are good conductors. For good conductors, RF waves are able to penetrate through the conductor's wall to a small finite distance inside the conductor.[7] This phenomenon is called the skin effect.[7]

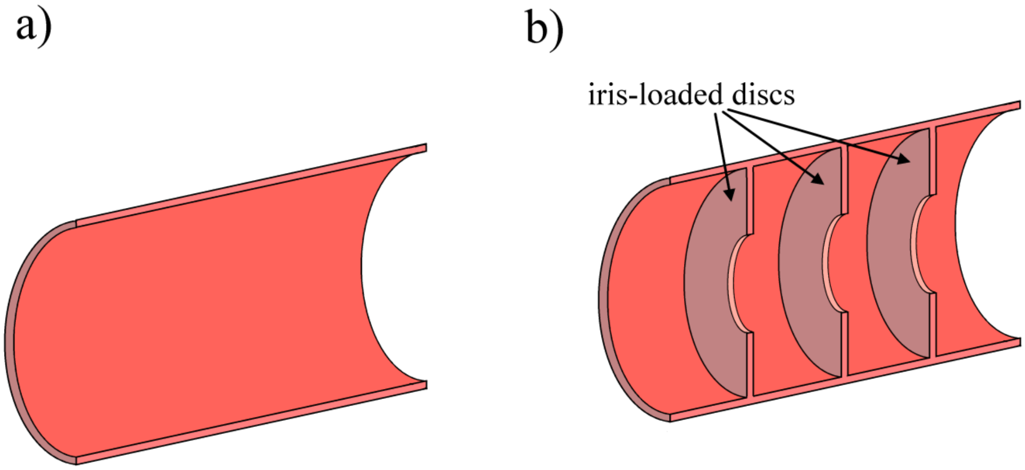

Figure 2.6: A schematic diagram of a) a cylindrical waveguide and b) an iris-loaded waveguide used to create slow waveguides

A simple waveguide is a hollow cylinder as seen in Fig. 2.6a. In a cylindrical waveguide, one of the possible set of modes is the transverse-magnetic modes (TM_{01n}, where n = 0,1,2,3, …). In the TM_{01n} mode, the longitudinal magnetic field component vanishes. In the simplest mode (TM_{010}), the longitudinal electric field solution of Eq. 2.47 is described by Eq. 2.54 with k_{z0} calculated from Eq. 2.56 and J_0 as a Bessel function of the first kind.[5]

$$\mathbf{E}(r,z,t) = E_0 J_0\left(\sqrt{k_0^2 - k_{z0}^2}\, r\right) e^{i(\omega t - k_{z0} z)} \hat{\mathbf{z}} \qquad 2.54$$

$$k_{z0} = \frac{2\pi}{\lambda_g} \qquad 2.55$$

2.3.4 Dispersion relation and group velocity

Eqs 2.44 and 2.45 propagates only monochromatic RF waves. In reality, propagating waves are a superposition of many different frequencies and wavenumbers.[7] When the propagating wave in matter is composed of a range of frequencies, a phenomenon called dispersion, which is the dependence of the phase velocity v_p on the frequency of the propagating waves,[1,3] can occur. When there is no dispersion, the encompassing envelope of the propagating waves move without losing its shape.[7] Therefore, information can be transmitted with the propagating waves. The velocity of this envelop is called the group velocity v_g (Eq. 2.56).

$$v_g = \frac{d\omega}{dk_{z0}} \qquad 2.56$$

To calculate v_g for the waveguide described above, the waveguide's dispersion relation is needed. In a vacuum, the relative permeability μ_r and the relative permittivity ε_r from Eq. 2.46 are unity and c is the speed of light; therefore, the cylindrical waveguide's dispersion relation is described by Eq. 2.57.

$$k_{z0}^2 = \frac{\omega^2}{c^2} - \frac{\omega_c^2}{c^2} \qquad 2.57$$

$$c = \frac{1}{\sqrt{\mu_0 \varepsilon_0}} \tag{2.58}$$

Eq. 2.57 is visualized in a plot of ω versus k_{z0} in Fig. 2.7.

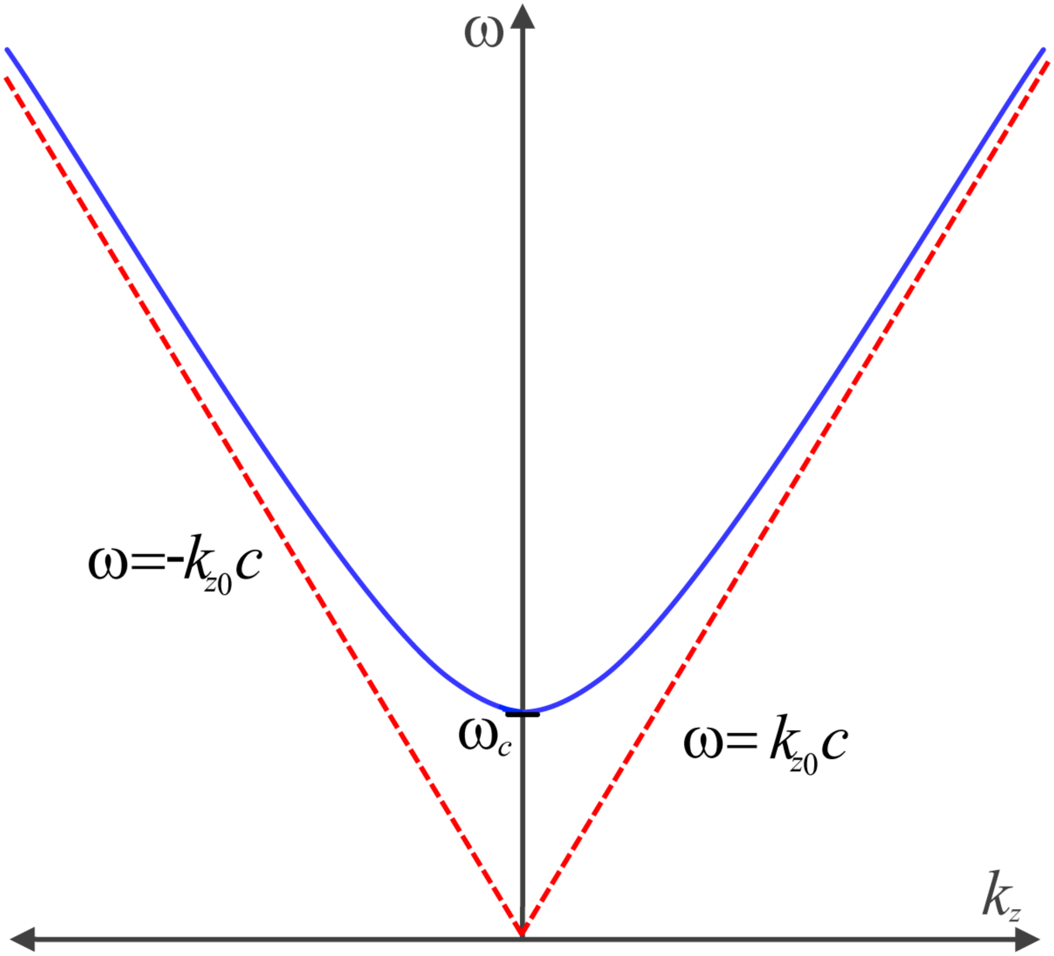

Figure 2.7: A representative dispersion relation plot for a uniform waveguide. The solid blue curve is calculated from Eq. 2.57 while the red dashed line is a plot of a linear dispersion relation where $\omega = ck_{z0}$. The y-intercept of the blue curve is the cut-off frequency ω_c.

The frequency ω_c (the y-intercept of the solid blue curve in Fig. 2.7 at $k_{z0} = 0$) is called the waveguide's cut-off frequency. RF waves with $\omega < \omega_c$ cannot propagate in the waveguide. They exponentially decay as they pass through the waveguide.

The quantity v_p (Eq. 2.59) is called the phase velocity and Eq. 2.60 shows v_g for the uniform cylindrical waveguide.

$$v_p = \frac{\omega}{k_{z0}} = \frac{c}{\sqrt{1 - \frac{\omega_c}{\omega}}} \qquad 2.59$$

$$v_g = c\sqrt{1 - \left(\frac{\omega_c}{\omega}\right)^2} \qquad 2.60$$

For the cylindrical waveguide, $v_p > c$; therefore, a hollow cylindrical waveguide cannot be used in particle acceleration.[7, 15, 17] Particle acceleration requires phase matching between particles and EM wave; this matching cannot be accomplished if $v_p > c$ since particle velocities cannot exceed the speed of light.[15] A solution to this limitation is to use using iris-loaded discs in the cylindrical waveguide structure (as illustrated in Fig. 2.6b) to create slow waves.[15,17,19]

Slow waves are EM waves that have a property of $v_p <$ c. These waves are created by adding iris-loaded discs to the cylindrical waveguide as shown in Fig. 2.6b. This thesis will provide a simplified treatment of iris-loaded waveguides although this topic is treated rigorously by Wangler in the book entitled *RF Linear Accelerators.*[7] Iris-loaded waveguides will have a periodic structure. This periodic structure perturbs the accelerating field, which is **E** for the cylindrical waveguide, by introducing a static function $\mathbf{E}_p$ defined in Eq. 2.61.[7]

$$\mathbf{E}(r,z,t) = \mathbf{E}_p(r,z)e^{i(\omega t - k_{z0}z)} \qquad 2.61$$

The function $\mathbf{E}_p$ is a periodic modulation of the electric field's amplitude in the direction of the wave propagation. For a periodic waveguide structure with a period p, the Floguet's theorem[7] (Eq. 2.62) was used to obtain the solutions for the propagating waves.

$$\mathbf{E}(r,z+p) = \mathbf{E}(r,z)e^{\pm ik_{z0}p} \tag{2.62}$$

$$E_p(r,z) = \sum_{n=-\infty}^{\infty} a_n(r)e^{-\frac{i2\pi nz}{p}} \tag{2.63}$$

The sign in the exponent of Eq. 2.62 depends on the direction of the wave propagation. The magnitude of $\mathbf{E}_p$ is periodic; therefore, it can be expanded into a Fourier series (Eq. 2.63). Its direction is in the longitudinal or z- direction. When the coefficients $a_n(r)$ in Eq. 2.63 satisfy Eq. 2.47, Eq. 2.64 is obtained by substituting Eq. 2.63 into Eq. 2.61 and gives the solution for the propagating wave (Eq. 2.64). In Eq. 2.64, k_{zn} (Eq. 2.65) is the wavenumber for the n^{th} TM mode possible in the waveguide. Equation 2.66 gives the new dispersion relation for the iris-loaded waveguide.

$$E_z(r,z,t) = \sum_{n=-\infty}^{\infty} E_n J_0(K_n r)e^{i(\omega t-k_{zn}z)} \tag{2.64}$$

$$k_{zn} = k_0 + \frac{2\pi n}{p} \tag{2.65}$$

$$k_{zn}^2 = \frac{\omega^2}{c^2} - \frac{\omega_c^2}{c^2} \tag{2.66}$$

Equation 2.64 represents an infinite number of travelling waves called *space-harmonics*,[7] which are denoted by the subscript n. The *space-harmonics* with $n < 0$ are waves travelling in the $-z$ direction while the *space-harmonics* with $n > 0$ are waves travelling in the $+z$ direction. The *space-harmonic* with $n = 0$ is called the principal wave.[7] The phase velocity for the n^{th} *space-harmonics* (v_p^n) is given by Eq. 2.67, where $\lambda = \frac{2\pi}{\omega}$. In Eq. 2.67, v_p^0 is the phase velocity of the principal wave, which is obtained from Eq. 2.59.

$$v_p^n = \frac{v_p^0}{1 + \frac{\lambda n}{p}} \qquad 2.67$$

The principal wave usually have the largest Fourier amplitude from Eq. 2.64;[7] therefore, periodic waveguides like the iris-loaded waveguide are usually designed such that the principal wave is synchronous[7] with the particle beam for efficient energy transfer.

The iris-loaded waveguide will be divided in multiple cells. In each cell, RF energy is transferred to the charged-particles, and the charged-particles gain velocity. For efficient energy transfer, the charged-particles need a correct initial velocity by having a correct phase relative to the electric field when they enter each cell to gain velocity from the RF wave. For linacs made of identical cells, this phase is the same in all cavities. When a charged-particle has a constant phase in all cavities, it is called a *synchronous particle*. Its phase is called the *synchronous phase*.[20] Such a particle is injected in the waveguide at a stable point in the electric field's wavefront and, therefore, can maintain synchronism with the accelerating fields,[7] which is the electric field. Charged-particles with a phase close to the *synchronous phase* will have phases that oscillate around the stable point; however, charged-particles with phases far from the *synchronous phase* do not get accelerated in the waveguide.

2.3.5 Root mean square emittance

It is desirable to have a description of the coherent or laminar-like property of the electron beam in the linac electron gun and waveguide. An ideal electron beam will have the most laminar-like flow.[7,20] The quantity ε called the beam emittance provides a quantitative description of the laminar-like property of the linac's electron beam.[7,20] To calculate ε, the particle beam's phase-space, which consist of each particle's position (x, y, z) and momentum $\mathbf{p}$ (or velocity $\mathbf{v}$), is necessary. The phase-space can be visualized through 2D phase-space projections, which is a plot of each particle's normalized momentum versus its coordinates. In the traverse plane, phase-space projections are the plots of the x versus $\frac{p_x}{mc}$ and y versus $\frac{p_y}{mc}$, with m as the mass of the particle, and p_x and p_y and the x- and y-component of the particle's momentum, respectively. For convenience, the particles' divergence angles ($x' = \frac{p_x}{|\mathbf{p}|}, y' = \frac{p_y}{|\mathbf{p}|}$) are calculated from the momentum information in the particle beam's phase-space. The plots of the x versus x' and y versus y' are called the transverse trace-space or the unnormalized phase-space (also called a trace-space) projection of the particle beam[7]. When analyzing an axisymmetric particle beam, the plots of x versus x' and y versus y' will look identical to each other. The beam's trace-space can be plotted in terms of r, which is the electron's radial distance (with respect to gun's central axis) at the electron gun output, and r', which is the magnitude of the net angular deflection of the particle from the longitudinal (z) axis. Thus, r and r' are given by Eqs 2.68 and 2.69, respectively.

$$r = \sqrt{x^2 + y^2} \qquad 2.68$$

$$r' = \sqrt{x'^2 + y'^2} \qquad 2.69$$

When the effects of nonlinear forces are ignored and assuming that the particle's motion in the x, y, and z directions are independent from each other, the area of the beam's phase-space in the xp_x and yp_y planes remains constant.[18] Under this condition, the area in the beam's normalized phase-space (Fig. 2.8a) or trace-space (Fig. 2.8b) is assumed to be bounded by an ellipse.[18] Therefore, each point inside the ellipse in Fig. 2.8a and b is a possible location for the particle.[18]

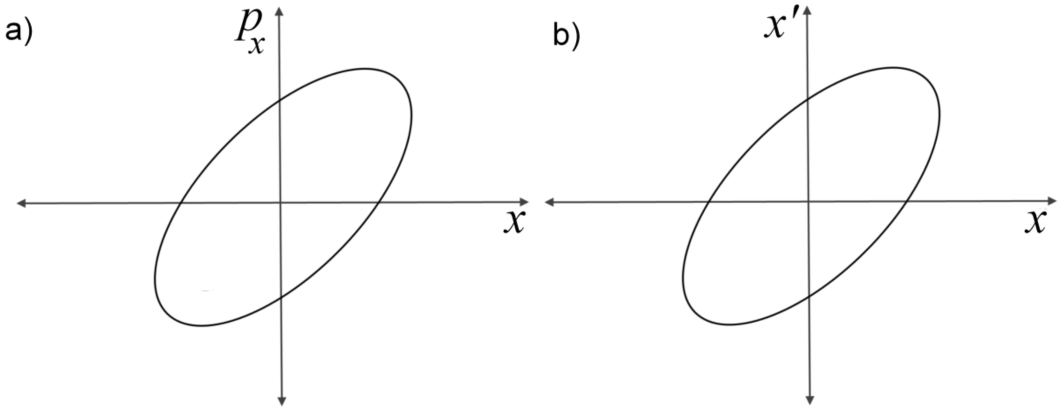

Figure 2.8: A transverse a) phase-space projection and b) a trace-space projection when the effects of nonlinear forces on the particle beam are ignored.

By, convention, the area of the elliptical plots in Fig. 2.8 divided by π defines the beam emittance ε.[7,18] When nonlinear forces are considered, the shape of the beam's phase-space is distorted[7,18] and a departure from the elliptical shapes of Fig. 2.8 is seened.[7] In this case, the unnormalized emittance is redefined in Eq. 2.70 based on mean-square values or the second moments of positions and the divergence angle.[7,21] The emittance in Eq. 2.70 is called the root-mean-square (rms) emittance ε_{rms}. Eq. 2.70 shows ε_{rms} along the x-axis, and ε_{rms} along y-axis will be identical to Eq. 2.70 but with y and y' instead of x and x'.

$$\varepsilon_{rms} = \sqrt{\overline{x^2}\,\overline{x'^2} - \overline{xx'}^2} \qquad 2.70$$

2.4 References

[1] Shadowitz. *The Electromagnetic Field* (McGraw-Hill, New York, 1975).

[2] H. D. Young and R. A. Freedman. *University Physics with Modern Physics* (Addison-Wesley, San Francisco, 2000).

[3] D. J. Griffiths. *Introduction to Electrodynamics* (Prentice Hall, New Jersey, 1999).

[4] J. Stewart. *Calculus* (Brooks/Cole Publishing Company, Pacific Grove, 1999).

[5] H. J. Weber and G. B. Arfken. *Essential Mathematical Methods for Physicists* (Elsevier Academic Press, New York, 2004).

[6] N. B. S. Gloria, M. C. L. Areiza, I. V. J. Miranda and J. M. A. Rebello. "Development of a magnetic sensor for detection and sizing of internal pipeline corrosion defects," NDT E Int., **42**, 669, (2009).

[7] T. P. Wangler. *RF Linear Accelerators* (Wiley-VCH, Weinheim, 2008).

[8] J. St. Aubin, S. Steciw, C. Kirkby and B. G. Fallone. "An integrated 6 MV linear accelerator model from electron gun to dose in a water tank," Med. Phys., **37**, 2279-2288, (2010).

[9] J. Pierce R. *Theory and Design of Electron Beams* (D. Van Mostrand Company, Inc., Toronto, 1949).

[10] H. E. Johns and J. R. Cunningham. *The Physics of Radiology* (C. C. Thomas, Illinois, 1983).

[11] Langmuir and K. B. Blodgett. "Currents Limited by Space Charge between Concentric Spheres," Phys. Rev., **24**, 49-59, (1924).

[12] D. Child. "Discharge From Hot CaO," Phys. Rev. (Series I), **32**, 492-511, (1911).

[13] Y. Y. Lau. "Simple Theory for the Two-Dimensional Child-Langmuir Law," Phys. Rev. Lett., **87**, 278301, (2001).

[14] R. H. Fowler and L. Nordheim. "Electron Emission in Intense Electric Fields," Proceedings of the Royal Society of London. Series A, Containing Papers of a Mathematical and Physical Character, **119**, pp. 173-181, (1928).

[15] J. St. Aubin. *Three dimensional simulation and magnetic decoupling of the linac in a linac-MR system*. Doctoral dissertation, University of Alberta, Edmonton, Alberta, Canada (2010).

[16] W. E. Boyce and R. C. DiPrima. *Elementary Differential Equations and Boundary Value Problems* (John Wiley & Sons, Inc, New Jersey, 2005).

[17] S. Humphries. *Charged Particle Beams* (John Wiley and Sons, New York, 1990).

[18] C. J. Karzmark, C. S. Nunan, E. Tanabe. *Medical Electron Accelerators* (McGraw-Hill, Inc., New York, 1993).

[19] J. St. Aubin, S. Steciw and B. G. Fallone. "The design of a simulated in-line side-coupled 6 MV linear accelerator waveguide," Med. Phys., **37**, 466-476, (2010).

[20] S. Humphries. *Principles of Charged Particle Acceleration* (John Wiley and Sons, New York, 1986).

[21] L. M. Young. "Parmela", LA-UR-96-1835, (2005).

CHAPTER 3 : NUMERICAL TECHNIQUES

3.1 Introduction

The simulations performed in this project employed various software packages to calculate the electric and magnetic fields within a bound and an unbound system. The mathematical description of the numerical techniques, which are used by the software used in this project, is presented in this chapter.

3.2 Finite element method (FEM)

FEM is a numerical technique used to calculate approximate solutions to boundary-value problems.[1] It has been successfully applied to electromagnetism and is a powerful and versatile tool that can handle unstructured grids[2] and complex geometry.

In this work, FEM is the computational technique used by the computer software OPERA-3D /SCALA (Cobham Technical Services, Kidlington, UK) and COMSOL Multiphysics (Burlington, MA). In this document, OPERA-3D /SCALA will be referred to SCALA. The 3D electron gun model[3] and 3D waveguide model[4] was previously created by Dr. St. Aubin in SCALA and COMSOL, respective. The electron gun model was used to calculate the electrostatic fields in a Pierce-diode electron gun and to track the electron trajectories during the electron gun's operation.[3,4] The waveguide model was used to calculate the RF fields in a Varian 600C wavguide.[4,5] For this work, a 3D fringe magnetic field model, which will be described later in CHAPTER 5, was created in COMSOL. The fringe magnetic field model was used to emulate the fringe magnetic fields of a 0.5 T MROpen^{TM} imager.[5,6] These three 3D models were used extensively in this work.

The general FEM techniques can be divided into a five major portions: mesh generation, basis function selection, elemental equations formulation, system matrix assembly and system matrix solution.

3.2.1 Mesh generation

The first step in FEM is the domain discretization. In this step, the domain Ω is divided into a number of smaller sub-domains or finite elements Ω^{el}, where the superscript *el* denotes the sub-domain number[1]. This step is important since it affects the problem's memory requirements, computation time, and the accuracy of the solution. The solution to the unknown function **u** will have improved accuracy as the elements become smaller. However, smaller elements increase the number of sub-domains used to discretization Ω and result in larger memory requirements and longer computation time.

The shape of the finite elements will depend on the type of problem that needs to be solved. In the one dimension, the finite elements is a line (Fig. 3.1a), either straight or curved.[1] Two dimensions have a choice of quadrilateral or triangular finite elements (Fig. 3.1b). The quadrilateral element is best suited for domains which have regular rectangular shapes.[1] Triangular elements, on the other hand, can be used in irregularly shaped domains[1]. In three dimensions, tetrahedral, triangular prisms, and rectangular bricks can be used (Fig. 3.1c). Of these elements, the tetrahedral element is best suited for arbitrarily shaped three dimensional domains.[1]

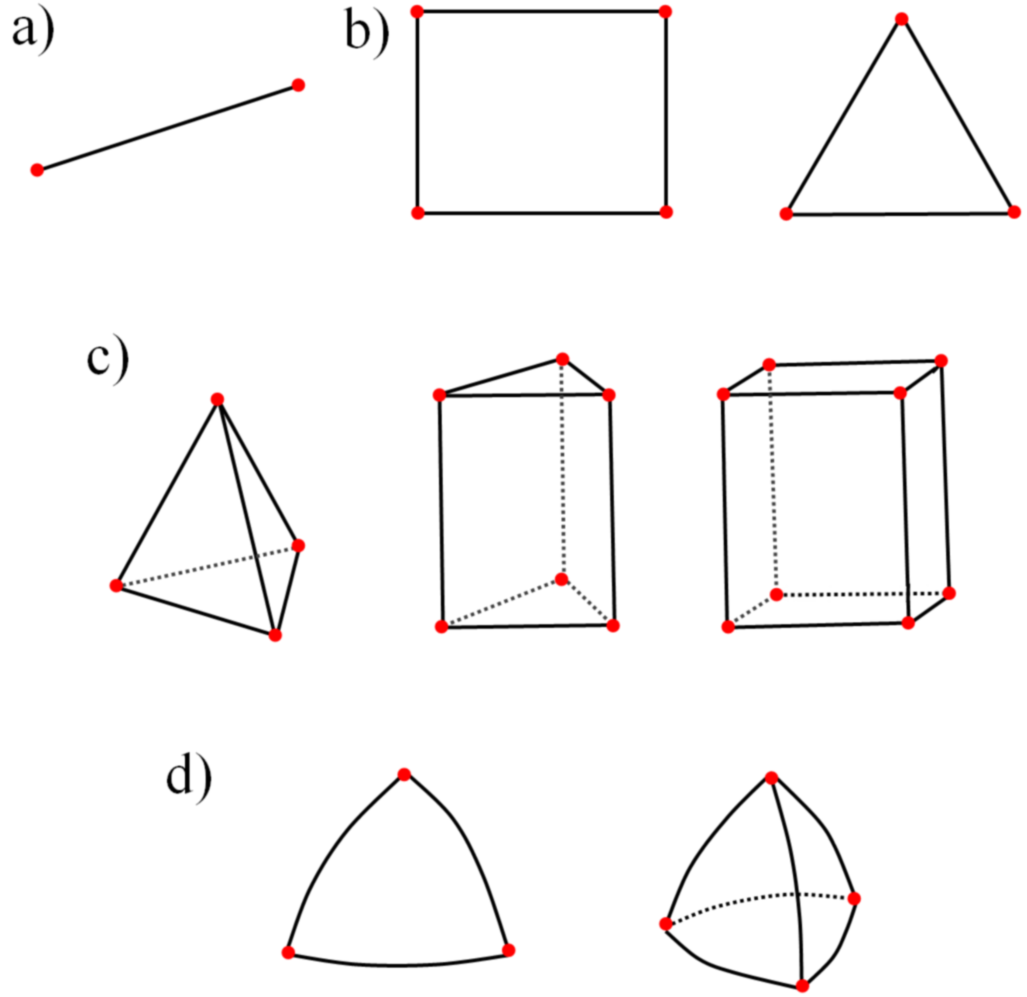

Figure 3.1: Possible finite element shapes for a system that is a) one dimensional, b) two dimensional, and c) three dimensional. d) Finite element shapes with curved edges. The red dots in each of the finite element shape are called nodes.

When generating the mesh, there can be no overlap or gaps between the each finite element. Neighbouring finite elements need to be connected by the element's vertices (or nodes); an element cannot have a vertex/node along the face or edge of its neighbour. In order to better conform to curve boundaries and provide a better approximation of the function **u**, curve elemental edges can be used[1] (Fig. 3.1d).

Once the mesh is generated, optimization is needed to ensure the generated mesh will provide accurate solution to **u**. If triangular elements are used, the element's shape needs to be as close as possible to equilateral triangles to minimize numerical error caused by the mesh.[7] This condition applies to problems where the geometry is not elongated, and ideally the aspect ratio in all dimensions is unity. Computational instability occurs the finite element mesh consist elongated triangles[7] since the error in triangular finite element is proportional to the length of its longest side. An optimization method of preventing the appearance of elongated triangular element and achieving greater accuracy in the numerical solution is called the Delaunay triangulation.[8] This mesh optimization method ensures that the triangular elements in the mesh remain as closes as possible to equilateral triangle[8] and, therefore, providing greater accuracy in the numerical solution. Both COMSOL and SCALA use this method for mesh optimization.

During mesh generation, efficient memory use is achieved through proper element and node (shown as red dots in Fig. 3.1) labels. To be of any use, the coordinate values, the local number, and the global number for each node in every element needs to be specified and be unique for each node. The node's local number describes the nodes position within the element while the global number specifies the nodes location in the entire system.[1] The node's coordinate value specifies the nodes location according to the coordinate system used for the problem. A way of organizing all the necessary node description efficiently is by using the *T*- and *P*- arrays. The *T*-array is an N^e x q^e array where the superscript *e* is the element number, N^e is the number of elements, and q^e is the node number within the element *e*. The node numbering scheme within an element is usually counter-clockwise to ensure that the area of the finite element is positive. The *T*-array maps the local node location to the global node location. The second array, the *P*-array, simply maps each node's global number to its coordinate values. Its size is N^q x d^e, where N^q is the total number of nodes in the system and d^e is the dimension of the system. *T*- and *P*- arrays are necessary when the system matrix is being assembled.

3.2.2 Basis function selection

After the mesh generation and optimization are finished, the basis or shape function ϕ is selected. A basis function is an interpolation function used in FEM to approximate **u** within each element. A common basis function used in FEM software, which includes SCALA and COMSOL, is the Lagrange basis function.[1] The Lagrange basis function uses the Lagrange polynomial[9] in its interpolation. One property of the Lagrange basis function is that at the i^{th} node, its value is 1 while its value is 0 at all the other nodes. Its simplest form is a linear or first order function while higher order functions can achieve greater accuracy in the solution. SCALA can use the first and second order Lagrange basis function while COMSOL can use up to the sixth order Lagrange basis function.

Lagrange basis functions are scalar basis functions, and it is not suitable to discretize the vector form of an EM problem such as Eqs 2.47 and 2.48. Only the basis function is required to be continuous at the i^{th} node while its derivative does not need to be continuous. Therefore, the divergence condition Eqs 2.39 and 2.40 will not be satisfied, and spurious modes or nonphysical solutions could occur.[1,10] In addition, boundary conditions, such as the Neumann boundary condition, along the element edges need to be explicitly enforced on the problem.[1] These limitations can be overcome by using vector basis functions, such as the curl-conforming functions introduced by Nedelec,[11] instead of using the Lagrange basis function. These functions are used by COMSOL for the EM vector problems. This function is appropriate for discretization of the Eqs 2.47 and 2.48 since it provide the required tangential and normal continuity along element edges.[10] Therefore, the divergence condition is satisfied, and these functions can suppress the occurrences of spurious modes[10] which would occur when the Lagrange basis function are used. It can also implicitly impose Neumann boundary conditions on $\mathbf{u}$,[10] simplifying the required formulation of the system equations. Like the Lagrange basis functions, the vector basis function can obtain better accuracy in the field solutions by using higher order functions.[10] COMSOL can use up to cubic vector basis function to solve EM vector problems.

3.2.3 Formulation of elemental equation

After the system mesh is generated and the basis function is selected, the system PDE needs to be discretized and the elemental matrix equation needs to be formulated. Two common approaches in formulating the elemental equation are the Galerkin's method[1] and the Rayleigh-Ritz variation method.[1] Since both COMSOL and SCALA used the Galerkin's method, an example of the Galerkin's method is provided in this thesis. The Rayleigh-Ritz variation method is treated by Jin in the book *The Finite Element Method in Electromagnetics*.[1] In either method, the resulting elemental equation will have the form of Eq. 3.1.

$$\mathbf{K}^e\mathbf{u}^e = \mathbf{b}^e \qquad 3.1$$

Thus, $\mathbf{K}^e$ is the elemental stiffness matrix, $\mathbf{u}^e$ is the unknown solution in the element *e*. In addition, $\mathbf{b}^e$ is the elemental load vector. The elemental equation will be used to assemble the system equation. Galerkin's method is part of more general technique called *method of weighted residual*.

In general, the PDE defined as $L\tilde{\mathbf{u}} - \mathbf{g}$, L is the operator, $\tilde{\mathbf{u}}$ is an approximation of $\mathbf{u}$, and $\mathbf{g} = L\mathbf{u}$. The Galerkin's method states that the best approximation for $\mathbf{u}$ is the one that gives the least residual $\mathbf{r}_{res}$ Eq. 3.2.

$$\mathbf{r}_{res} = L\tilde{\mathbf{u}} - \mathbf{g} \qquad 3.2$$

Minimization of $\mathbf{r}_{res}$ can be achieved by minimizing the L_2 norm of Eq. 3.2.

$$||\mathbf{r}||^2 = \iint\limits_{\Omega} |L\tilde{\mathbf{u}} - \mathbf{g}|^2 \mathrm{d}\Omega \qquad 3.3$$

When the weighting function is the local basis function ϕ_i^e for the i^{th} node and e^{th} element, the Galerkin's method's weak solution formulation to the PDE is then given by Eq. 3.4.

$$\langle L\tilde{\mathbf{u}}^e - \mathbf{g}, \phi_i^e \rangle = 0 \qquad 3.4$$

The approximate solution $\tilde{\mathbf{u}}^e$ over the e^{th} element is then expressed as the sum of the weighted solution at each node in the element (Eq. 3.5).

$$\tilde{\mathbf{u}}^e = \sum_{j=1}^{q^e} u_j^e \phi_j^e \qquad 3.5$$

In the magnetostatic case such as the current loop presented in § 2.1.2-2.1.4, the equation to be discretized is the Ampère's law. The current loop described in § 2.1.2-2.1.4 is axisymmetric; therefore, the Ampère's law can be written in cylindrical coordinates in Eq. 3.6 where J_ϕ is the azimuthal component of the current.

$$-\frac{\partial}{\partial r}\left[\frac{1}{r\mu_r\mu_0}\frac{\partial\left(rA_\phi\right)}{\partial r}\right] - \frac{\partial}{\partial z}\left[\frac{1}{r\mu_r\mu_0}\frac{\partial\left(rA_\phi\right)}{\partial z}\right] = J_\phi \qquad 3.6$$

The boundary conditions on the domain boundaries are the natural Neumann boundary condition (Eq. 3.7) while interfaces between the sub-domains used a continuity boundary condition (Eq. 3.8).

$$\hat{\mathbf{n}} \times (\nabla \times \mathbf{A}) = 0 \qquad 3.7$$

$$\hat{\mathbf{n}} \times \mathbf{H}^+ = \hat{\mathbf{n}} \times \mathbf{H}^- \qquad 3.8$$

When Eq. 3.6 is rewritten in the form of Eq. 3.2, the operator L is defined as

$$L = -\frac{\partial}{\partial r}\left[\frac{1}{r\mu_r\mu_0}\frac{\partial}{\partial r}\right] - \frac{\partial}{\partial z}\left[\frac{1}{r\mu_r\mu_0}\frac{\partial}{\partial z}\right] \qquad 3.9$$

When the Eq. 3.9 is substituted into Eq. 3.4, the inner product of Eq. 3.4 becomes Eq. 3.10 with $\lambda = \frac{1}{r\mu_r\mu_0}$ and $J_\phi = \mathbf{g}$.

$$-\iint_{\Omega}\left[\left[\frac{\partial}{\partial r}\left(\lambda\frac{\partial\tilde{u}^e}{\partial r}\right)\phi_i^e\right]+\left[\frac{\partial}{\partial z}\left(\lambda\frac{\partial\tilde{u}^e}{\partial z}\right)\phi_i^e\right]\right]d\Omega-\iint_{\Omega}J_\phi\phi_i^e d\Omega=0 \quad 3.10$$

When the identity in Eq. 3.11 (where $\delta s=\phi_i^e$ and x_n=r or z) and the divergence theorem[1] are invoked, Eq. 3.10 can be rewritten as Eq. 3.12.

$$\frac{\partial}{\partial x_n}\left(\lambda\frac{\partial}{\partial x_n}\right)\delta s=\frac{\partial}{\partial x_n}\left(\lambda\frac{\partial s}{\partial x_n}\delta s\right)-\left(\frac{\partial s}{\partial x_n}\frac{\partial\delta s}{\partial x_n}\right) \quad 3.11$$

$$\iint_{\Omega}\lambda\left[\frac{\partial\tilde{u}^e}{\partial r}\frac{\partial\phi_i^e}{\partial r}+\frac{\partial\tilde{u}^e}{\partial z}\frac{\partial\phi_i^e}{\partial z}\right]d\Omega-\iint_{\Omega}J_\phi\phi_i^e d\Omega$$
$$-\oint_{\Gamma}\left(\frac{\partial\tilde{u}^e}{\partial r}\cdot\hat{\mathbf{r}}+\frac{\partial\tilde{u}^e}{\partial z}\cdot\hat{\mathbf{z}}\right)\cdot\hat{\mathbf{n}}d\Gamma=0 \quad 3.12$$

The superscript e is the element number, and subscript i is the local node number for each element. When the i^{th} node is within the boundary Γ, the surface integral in the last term of Eq. 3.12 is zero because there will be another node within Γ that will cancel the contribution of this surface integral.[1] On the boundary Γ, this surface integral will also be zero because of the natural Neumann boundary condition being used in this problem (Eq. 3.7). When Eq. 3.5 is substituted into Eq. 3.12, Eq. 3.12 can be rewritten as

$$\sum_{j=1}^{q^e}\left[\iint_{\Omega}u_j^e\lambda\left[\frac{\partial\phi_j^e}{\partial r}\frac{\partial\phi_i^e}{\partial r}+\frac{\partial\phi_j^e}{\partial z}\frac{\partial\phi_i^e}{\partial z}\right]d\Omega-\iint_{\Omega}J_\phi\,\phi_i^e\,d\Omega\right]=0 \quad 3.13$$

Eq. 3.13 can be rewritten in matrix form of Eq. 3.1. Thus, elements of the elemental stiffness matrix K_{ij}^e and the elemental load vector b_i^e are given by Eqs 3.14 and 3.15, respectively.

$$K_{ij}^{e} = \iint_{\Omega} \lambda \left[\frac{\partial \phi_j^e}{\partial r} \frac{\partial \phi_i^e}{\partial r} + \frac{\partial \phi_j^e}{\partial z} \frac{\partial \phi_i^e}{\partial z} \right] d\Omega \qquad 3.14$$

$$b_i^e = \iint_{\Omega} J_{\phi}\, \phi_i^e \, d\Omega \qquad 3.15$$

3.2.4 Matrix assembly

Once the elemental matrix equation (Eq. 3.1) is formulated, Eq. 3.1 needs to be assembled into the system matrix equation. The system matrix assembly involves using the local and global indexes from the *T*-array of each elemental stiffness matrix $\mathbf{K}^e$ into the system stiffness matrix **K**. Each element of **K** is given by Eq. 3.16 in terms of each element of $\mathbf{K}^e$.

$$K_{n(e,i)\ n(e,j)} = K_{ij}^{e} \qquad 3.16$$

$$b_{n(e,i)} = b_i^e \qquad 3.17$$

Likewise, each elements of the system load vector **b** is assembled in terms of the elemental load vector in a similar manner (Eq. 3.17). In Eqs 3.16 and 3.17, *n* is the global node number and *e* is the elemental number. In addition, *i* and *j* are the elemental or local node number.

3.2.5 Matrix solution

Once the system matrix equation and the system load vector are assembled, the approximate solution $\tilde{\mathbf{u}}$ is calculated by solving the matrix equation (Eq. 3.18) with a large number of matrix elements.

$$\mathbf{K}\tilde{\mathbf{u}} = \mathbf{b} \qquad 3.18$$

There are many different techniques that can be used to solve Eq. 3.18 such as the Gaussian elimination,[1] conjugate gradient method,[1] the *LU* decomposition,[1] and the LDL^T decomposition.[1] These methods can be divided into direct and iterative solvers. In this work, the 3D fringe magnetic field model is an open bounded system. Therefore, the domain Ω needed for this work is large and has large memory requirements. Because iterative solvers, in general, require less computer memory than direct solvers, an iterative solver call the flexible GMRES or FGMRES[12,13] was used in COMSOL to calculate the MR's fringe magnetic fields. Although iterative solvers are less stable than direct solvers, its convergence is improved through the use of a pre-conditioner.[1] A pre-conditioner is a matrix that transforms the current problem into another problem with the same solution but provides a solution[1] faster. For this work, the pre-conditioner used was the Geometric multigrid[14,15] which takes advantage of the symmetric nature of the geometric structure[14] in the problem.

3.3 The particle tracking code PARMELA

The particle tracking software "Phase and Radial Motion in Electron Linear Accelerators" (PARMELA) from Los Alamos National Laboratory in New Mexico was used in this project to track the electron trajectories inside the time-varying RF fields of a linac waveguide. Each particle used in PARMELA is a representative particle (or *marcoparticle*) that consists of millions of electrons.[16] The velocity (Eq. 3.19) of each particle and the impulses exerted on the particles are (Eq. 3.20) calculated through leap-frog fashion.

$$\mathbf{v}_i = \frac{d\mathbf{x}_i}{dt} \qquad 3.19$$

$$\mathbf{F}_i = m_i \frac{d(\gamma_i \mathbf{v}_i)}{dt} \qquad 3.20$$

Thus, m_i is the mass of the particle i, and γ_i (Eq. 3.21) is the relativistic coefficient needed for Lorentz transformation between the lab frame of reference and the particle's frame of reference.

$$\gamma_i = \frac{1}{\sqrt{1 - \left(\frac{|\mathbf{v}_i|}{c}\right)^2}} \qquad 3.21$$

At each time-step Δt, the electron's spatial coordinates, its dimensionless momentum ($\beta\gamma$), its dimensionless energy γ, its mass, and its charge is known. The space-charge and Eq. 3.20 is evaluated through a particle-in-a-cell (PIC) algorithm[17,18] in PARMELA. This PIC algorithm first generates a user defined space-charge mesh grid of has discrete r_{ij} and z_{ij} values, where ij^{th} denotes a node. A Lorentz transformation of the particles' current coordinates and momentum from the lab frame of reference to the rest frame of space-charge mesh is then made.[18] The space-charge, which is a vector sum of the electric fields generated by all *marcoparticles* is calculated for each ij^{th} node.[18] External electric fields and external magnetic fields, which are calculated by other software packages, can be added to PARMELA through external field maps. The vector sum of all the external electric fields, the external magnetic fields, and the space-charge at each ij^{th} node[18] are calculated. The Lorentz forces that results from the all of the fields present in the waveguide are applied each *macroparticle*.[18] The new longitudinal velocity of the particle is used to find the longitudinal displacement Δz where the particle will drift to during a time interval Δt.[18] If the particle drifts pass the end of the mesh, the Δt is decreased so that the particle will be displaced to the end of the mesh.[18] From the new particle velocity, the particles' coordinates after a period Δt is calculated.

3.4 Monte Carlo

Unlike other numerical methods such as FEM and finite difference method, MC is nondeterministic and probabilistic technique.[2,16] It was named by a group of physicist working at the Los Alamos during the early nuclear weapons development in the 1940s.[2] Although other numerical methods (or any large scale computer simulation) will involve using random numbers or the random generation of mesh points, the deliberate use of random numbers to find mean or expectation values of a system component f is what differentiates MC from the other numerical techniques. Two uses for MC simulations are found in the kinetic particle transport applications and random walk applications. In the particle transport applications, a probability distribution function (PDF) is required and is integrated into a cumulative distribution function (CDF). Random numbers are used to sample the CDF to obtain an expectation value for f. The MC kinetic particle transport simulations are used in the software packages EGSnrc[19-21] and PENELOPE,[22] where the PDF is defined by the particle's differential cross-sections.[23] In the random walk applications, the PDF is not necessary. A mesh (such as a grid if the problem is in two dimensions) is used. A set of random numbers can be used to vary the step size in the mesh while a second set of random numbers are used to decide an action within the mesh. For this work, a version of an MC random walk simulation, which is described in § 3.4.1, was used to optimize the current loop parameters in the analytic MR fringe magnetic field model (*currentloop*$_{analytic}$ *model*), which will be described in CHAPTER 4.

3.4.1 MC optimization

The *currentloop*$_{analytic}$ *model*, which will be described later in CHAPTER 4, needed to emulate the magnetic fringe flux densities from an MR imager. To accomplish this, an MR optimization, which uses a MC floating random walk application, was created. It optimizes the *currentloop*$_{analytic}$ *model*'s parameters to emulate the manufacturer supplied MR fringe magnetic field isoline data. The *currentloop*$_{analytic}$ *model*'s parameters are the loop current I_{ab}, the loop radius R_{ab}, the separation distance d_{ab}, and the number of current loop pairs n_a. The subscript a indicates the number of iterations, and the subscript b indicates the current loop pair being described. A current loop model can be used in the MR fringe magnetic flux density model because the manufacturer supplied data is symmetric about the *xy*-plane. Since the manufacturer data was axisymmetric along the magnets longitudinal (z-) axis, no off-axis offset was applied to the current loop pairs. The MR optimization begins with a user defined initial value or guess (n_0, I_{0b}, R_{0b}, and d_{0b}) for each current loop pair. The optimization minimizes the objective function f_a (Eq. 3.22), where B^{man} is the manufacturer supplied magnetic flux density data.

In Eq. 3.22, i denotes the i^{th} data point, and N is the total number of data points used.

$$f_a = \sum_{i=1}^{N} \left(B_a^{loop} - B^{man}\right)^2 \qquad 3.22$$

$$B_a^{loop} = \sum_{j=1}^{n_a} B_j \qquad 3.23$$

The model's net magnet flux density B_a^{loop} is calculated through Eq. 3.23. In Eq. 3.23, B_j is the magnetic flux density of the j^{th} current loop.

For each iteration, I_{ab}, R_{ab}, and d_{ab} are varied by an amount $r_1\Delta I_a$, $r_2\Delta R_a$, and $r_2\Delta d_a$, respectively. The r_1, r_2, and r_3 values are randomly generated numbers within a range of -1 to 1. Thus, ΔI_a, ΔR_a, and Δd_a are the maximum step size for I_{ab}, R_{ab}, and d_{ab}, respectively. At the end of each iteration, f_a is calculated and tested if it is a minimum. The values for n_a, f_a, I_{ab}, R_{ab}, and d_{ab} are retained if f_a is a minimum or if the maximum number of iterations, which is user defined, is reached, n_a, I_{ab}, R_{ab}, and d_{ab} are used for n_0, I_{0b}, R_{0b}, and d_{0b}, respectively. In order to refine the model, the MR optimization sets the retained n_a, f_a, I_{ab}, R_{ab}, and d_{ab} as the new n_0, I_{0b}, R_{0b}, and d_{0b}, respectively, and repeats the optimization described earlier with smaller ΔI_a, ΔR_a, and Δd_a. This refining process is repeated until a user defined tolerance value for Δf_a (described in Eq. 3.24) or the maximum number of iterations, which is user defined, is reached.

$$\Delta f_a = \left|f_a - f_{a-1}\right| \qquad 3.24$$

3.5 References

[1] J. Jin. *The Finite Element Method in Electromagnetics* (John Wiley & Sons, Inc., New York, 1993).

[2] M. N. O. Sadiku. *Numerical Techniques in Electromagnetics* (CRC Press, Boca Raton, Florida, 2000).

[3] J. St. Aubin, S. Steciw, C. Kirkby and B. G. Fallone. "An integrated 6 MV linear accelerator model from electron gun to dose in a water tank," Med. Phys., **37,** 2279-2288, (2010).

[4] J. St. Aubin, S. Steciw and B. G. Fallone. "The design of a simulated in-line side-coupled 6 MV linear accelerator waveguide," Med. Phys., **37,** 466-476, (2010).

[5] J. St. Aubin. *Three dimensional simulation and magnetic decoupling of the linac in a linac-MR system*. Doctoral dissertation, University of Alberta, Edmonton, Alberta, Canada (2010).

[6] J. St. Aubin, D. M. Santos, S. Steciw and B. G. Fallone. "Effect of longitudinal magnetic fields on a simulated in-line 6 MV linac," Med. Phys., **37,** 4916-4923, (2010).

[7] W. C. Thacker. "A brief review of techniques for generating irregular computational grids," Int J Numer Methods Eng, **15,** 1335-1341, (1980).

[8] M. de Berg, O. Cheong, M. van Kreveld and M. Overmars. *Computational Geometry: Algorithms and Applications* (Springer-Verlag, Berlin, 2008).

[9] H. Jeffreys and B. S. Jeffreys. *Methods of Mathematical Physics, 3rd ed.* (Cambridge University Press, Cambridge, England, 1988)

[10] R. D. Graglia, D. R. Wilton and A. F. Peterson. "Higher order interpolatory vector bases for computational electromagnetics," IEEE Trans. Antennas Propagat., **45,** 329-342, (1997).

[11] J. C. Nedelec. "A new family of mixed finite elements in R^3," Numerische Mathematik, **50,** 57-81, (1986).

[12] Y. Saad. "Chapter 9: Preconditioned Iterations" in *Iterative methods for sparse linear systems* 2nd ed. (SIAM, Philadelphia, 2003), pp. 261-281.

[13] Y. Saad. "A flexible inner-outer preconditioned GMRES algorithm," SIAM J. Sci. Comput., **14,** 461-469, (1993).

[14] Y. Zhu and A. C. Cangellaris. *Multigrid Finite Element Methods for Electromagnetic Field Modeling* (John Wiley & Sons, Inc, Hoboken, New Jersey, 2006).

[15] U. Trottenberg, C. Oosterlee, A. Schueller. *Multigrid* (Academic Press, San Diego, 2001).

[16] H. Fehske, R. Schneider and A. Weiße. *Computational Many-Particle Physics* (Springer, Berlin, 2008).

[17] P. Lapostolle, A. M. Lombardi, E. Tanke, S. Valero, R. W. Garnett and T. P. Wangler. "A modified space charge routine for high intensity bunched beams," Nucl. Instr. and Meth. A, **379,** 21, (1996).

[18] L. M. Young. , "Parmela", LA-UR-96-1835, (2005).

[19] D. W. O. Rogers, B. A. Faddegon, G. X. Ding, C. M. Ma, J. We and T. R. Mackie. "BEAM: A Monte Carlo code to simulate radiotherapy treatment units," Med. Phys., **22,** 503-524, (1995).

[20] C. M. Ma, B. A. Faddegon, D. W. O. Rogers and T. R. Mackie. "Accurate characterization of Monte Carlo calculated electron beams for radiotherapy," Med. Phys., **24,** 401-416, (1997).

[21] I. Kawrakow, D. W. O. Rogers and B. R. B. Walters. "Large efficiency improvements in BEAMnrc using directional bremsstrahlung splitting," Med. Phys., **31,** 2883-2898, (2004).

[22] J. Sempau, A. Sanchez-Reyes, F. Salvat, H. O. b. Tahar, S. B. Jiang and J. M. Fernandez-Varea. "Monte Carlo simulation of electron beams from an accelerator head using PENELOPE," Phys. Med. Biol., **46,** 1163, (2001).

[23] H. E. Johns and J. R. Cunningham. *The Physics of Radiology* (C. C. Thomas, Illinois, 1983).

CHAPTER 4 : LONGITUDINAL MAGNETIC FLUX DENSITY EFFECTS ON 6 MV IN-LINE LINAC

A version of this chapter has been published. J. St. Aubin, D. M. Santos, S. Steciw, B. G. Fallone, "Effects of longitudinal magnetic fields on a simulated 6 MV linac," Med. Phys., 37, 4916-4923 (2010).

4.1 Introduction

The work presented in this chapter is a continuation of work done previously by our group, where a full 3D linac simulation was generated and emulated a Varian 600C linac.[1,2] This linac simulation was validated previously by using experimental measurements from a Varian 600C linac under normal operating conditions (0 T),[2] and its performance in the presence of perpendicular magnetic fields was investigated[3] by our group as well. These magnetic fields traversed the linac perpendicular to the electron trajectories in the waveguide.[3] The transverse/perpendicular magnetic fields occur in the *perpendicular linac-MR configuration* shown in Fig. 1.2. Our group has shown that a perpendicular magnetic field causes asymmetric dose distributions,[3] and field strengths as small as 0.0014 T causes a complete loss of the linac treatment beam[3]. Solutions such as the use of the primary collimators manipulation[3] and/or displacing the linac target off-axis[3] was proposed to regain symmetric dose distributions. Furthermore, the use of passive and active magnetic shield was investigated previously to recovery the lost linac output dose rate.[4,5]

While the effects of perpendicular magnetic fields on the linac's performance have been studied in detail, the effects of *longitudinal/parallel* magnetic fields on the linac performance needed to be studied. These magnetic fields occur in the *parallel linac-MR configuration* in Fig. 1.3. This project studies the effects of longitudinal magnetic fields on linac performance, and the use of passive and active magnetic shields to recovery any lost linac output, which is measured as the linac target current or linac dose rate. The work from this project is divided into two parts. The first part, which is presented in this chapter, deals only with the linac performance in the presence of longitudinal magnetic fields. This work present in this chapter is part of a publication[6] entitled "Effect of longitudinal magnetic fields on a simulated in-line 6 MV linac" in the *Medical Physics Journal*. The focus of the second part is the magnetic shield study and is presented in CHAPTER 5.

4.2 Methods

4.2.1 Linac simulation

The study on the effects of the *parallel/longitudinal* magnetic fields on a 6 MV linac used the linac simulation that was previously created by our group.[1,2] The linac simulation consists of the electron gun simulation[2] and the waveguide simulation.[1] The electron gun simulation is a 3D FEM model based of a pierce-diode electron gun,[7] which is a common electron gun design. It was created using the SCALA. The cathode thermionic emission model used was based off the Child's Law[8] (Eq. 2.38). The SCALA simulations used tetrahedral elements optimized through an optimization method based off Delaunay triangulation.[9] Second order Lagrange basis functions were used. The electron gun model emulates the electron gun of a Varian 600C linac. Its output is a 6 dimensional

(6D) phase-space file containing the x, y, and z position and the v_x, v_y, and v_z velocity of each electron. This 6D output phase-space served as an input into the waveguide simulation. The waveguide simulation consists of a 3D waveguide model, which emulated the waveguide of a Varian 600C[1] and particle tracking simulation. The 3D waveguide model was created, previously, in COMSOL and was used to solve the RF field solutions inside the waveguide model[1] since SCALA cannot solve for the time-varying RF field inside the waveguide. The particle tracking simulation used the particle tracking code PARMELA (described in § 3.3). PARMELA used the output phase-space from the electron gun simulation for the initial conditions of the electron injected into the waveguide and for the space-charge calculations in the waveguide (described in § 3.3). The RF field solutions and any 3D external magnetic or/and electric field maps are used by PARMELA to track the electrons as they travel through the waveguide in a leap-frog fashion described in § 3.3.[1,2] PARMELA writes a 6D output phase-space file for the electrons that are incident on the linac target. The 6D output phase-space from the electron gun simulation and the waveguide simulation were analyzed to evaluate the performance of the linac.

4.2.2 MR fringe magnetic field

The *parallel linac-MR configuration* uses an open MR imager such the PARAmed 0.5 T MROpen^{TM}. The magnitude of the MR's fringe magnetic flux density will vary depending on the linac's location along the symmetric axis of the MR imager. The expected range of linac's source-to-axis-distance (SAD) in the linac-MR is from 1.0 to 2.2 m. In this investigation, three SADs were studied (1.0 m, 1.5 m, and 2.2 m) which have expected magnitudes of MROpen$^{\text{TM}}$'s fringe magnetic flux density of 0.011 T, 0.0046 T, and 0.0022 T, respectively, as measured at the electron gun cathode.

4.2.3 Creation and optimization of the analytic current loop model

The linac simulation required 3D magnetic flux density vector components in any arbitrary location. However, the PARAmed's magnetic isoline data provided only a 2D map of the magnetic flux densities magnitude for only a few magnetic isolines (0.0005, 0.001, 0.002, 0.005, 0.01, and 0.02 T), which must first be digitized. A check for any geometric distortion in the digitized isoline data was performed. Assuming that the MROpen$^{\text{TM}}$'s fringe magnetic flux density has a smooth drop-off and because the PARAmed isoline data shows no asymmetries, the superposition of analytic current loops (Eqs 2.24 and 2.25) was used to emulate the MROpen$^{\text{TM}}$'s fringe magnetic flux density. By using analytic current loop equations, the calculated magnetic flux density solutions are guaranteed to satisfy the Maxwell's equations for magnetostatics (Eqs 2.3 and 2.4); this model will be referred to as the $currentloop_{analytic}$ *model* in this thesis. Because Eqs 2.24 and 2.25 provides only the radial B_r and longitudinal B_z components of the magnetic flux densities, Eqs 4.1, 4.2, and 4.3 were used to transform B_r into B_x and B_y. The sign of Eqs 4.1 and 4.2 depends on which quadrant the measurement point for B_x and B_y is located.

$$B_x(x,y,z) = \pm \frac{B_r}{\sqrt{1 + \left(\frac{y}{x}\right)^2}} \qquad 4.1$$

$$B_y(x,y,z) = \pm \frac{B_r y}{x\sqrt{1 + \left(\frac{y}{x}\right)^2}} \qquad 4.2$$

$$r = \sqrt{x^2 + y^2} \qquad 4.3$$

In the *currentloop$_{analytic}$ model*, the currents and radius of each current loop, the separation distance between each current loop pair, and the number of current loop pairs were optimized in order to emulate the MROpen^{TM}'s fringe magnetic flux density. The optimization was performed for a cylindrical region, which has a radius of 0.2 m and length of 4 m, along the symmetric axis of the current loops. The objective function f_a was calculated by Eq. 3.22 and was minimized according to the MC optimization described in § 3.4.1. The current loops were aligned along their symmetric axis because the PARAmed data is axisymmetric about the z-axis (the magnet's longitudinal axis).

4.2.4 Effects of lateral misalignment of the linac in the presence of MR fringe magnetic flux densities

Linac-MR setup errors during the commissioning process and/or physical accidents can result in the linac misalignment from the MR magnet's symmetric axis. Therefore, the effects of an off-axis misalignment in the linac-MR setup on the linac performance were investigated with a worst-case scenario of a 10 mm off-axis offset. Therefore, the fringe magnetic flux density from the *currentloop$_{analytic}$ model* will no longer be axisymmetric, and there will be a net magnetic flux density component that is perpendicular to the electron trajectories in the waveguide. Perpendicular magnetic flux density, as small as 0.0014 T, can cause a 100 % treatment beam loss.[3] This 10 mm offset was simulated only for the 1.0 m SAD linac-MR setup because this setup has the strongest magnetic flux densities of all the scenarios investigated.

4.2.5 Extension to the stronger MR fringe magnetic flux densities

Other MR imagers, whether they are permanent, resistive, or superconducting magnets, have different fringe magnetic flux densities; therefore, this investigation was extended to include magnetic flux densities that are weaker and stronger than the MROpen^{TM}'s fringe magnetic flux densities. These other fringe magnetic flux densities were approximated by homogenous magnetic flux densities (from 0 to 0.2 T), which are parallel to the overall electron trajectories in the waveguide and are of equal strength everywhere.

4.2.6 Addition of the magnetic flux densities to the linac simulation

The necessary 3D vector components of the fringe magnetic flux densities (B_x, B_y, B_z) were added to the linac simulation through external magnetic flux density maps. For the electron gun, the Cartesian coordinates of the FEM mesh nodes of the 3D electron gun model were extracted. The magnetic flux density solutions at each mesh node was then calculated by using the $currentloop_{analytic}$ *model* described in § 4.2.3 and incorporated into our electron gun model as an external magnetic flux density map. The electron trajectories in the electron gun were tracked in SCALA, and the electron gun's 6D output phase-space was extracted from the electron gun simulation and used as the waveguide's injection beam's phase-space.

In the waveguide simulation, since PARMELA required a 3D rectangular mesh grid for its magnetic field maps, the magnetic flux density was solved by using the *currentloop*$_{analytic}$ *model* described in § 4.2.3 for a user defined 3D grid. PARMELA uses the electron gun's 6D phase-space to calculate the space-charge according the PIC algorithm described in § 3.3. PARMELA uses the magnetic flux density solutions, the space-charge, and the 3D RF field solutions in the waveguide to track the electrons trajectories in the waveguide through a leap-frog method described in § 3.3 until they reach the linac target. The 6D phase-space of the electrons incident at the linac target location was extracted and analyzed to evaluate the linac performance in the presence of longitudinal magnetic flux densities. Figure 4.1 is a flow diagram showing the steps involved in the linac simulation.

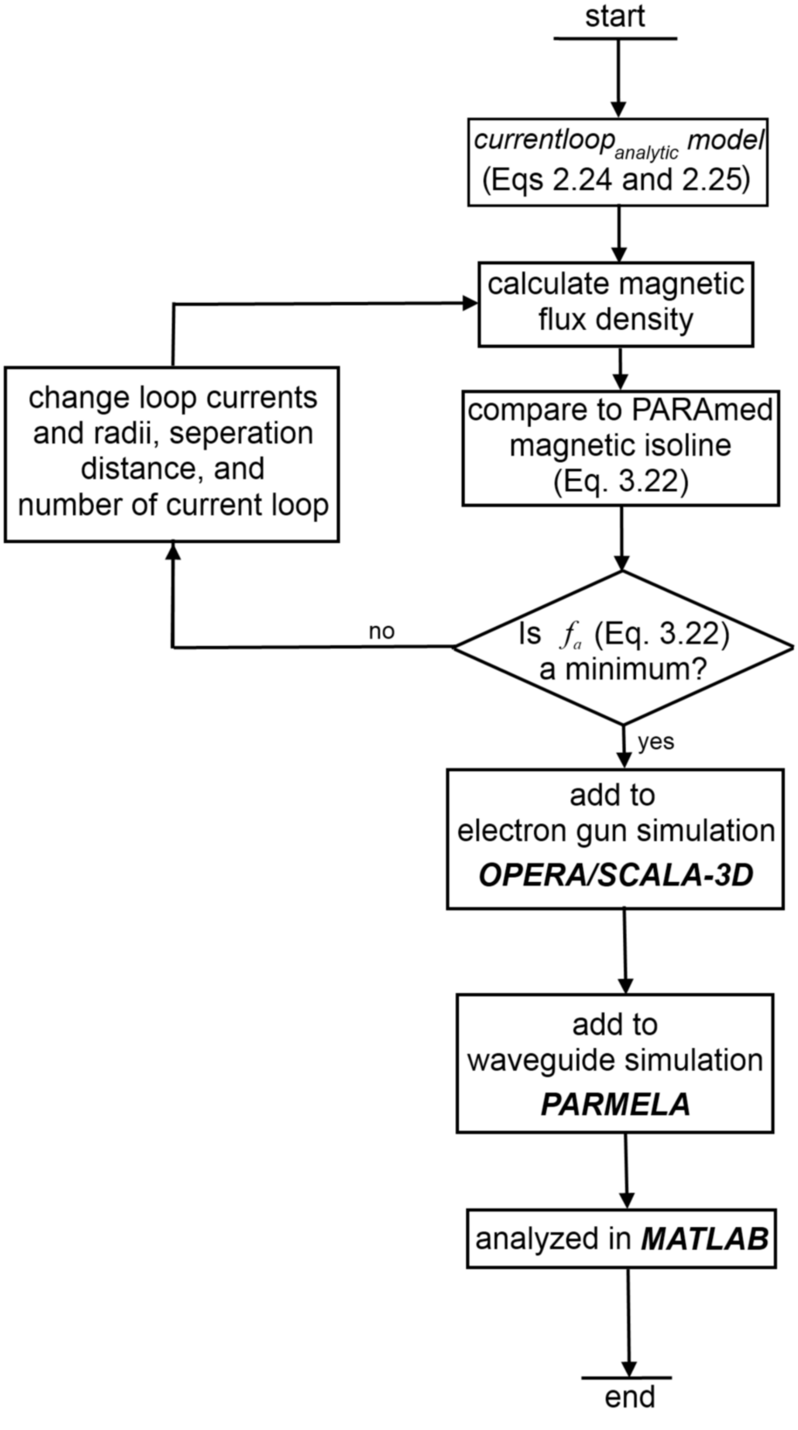

Figure 4.1: A flow diagram which shows the creation of the *currentloop$_{analytic}$ model* to the addition of magnetic flux density via external magnetic flux density maps to the linac simulation.

4.3 Results and Discussion

4.3.1 MR fringe magnetic field optimization

The MC optimized *currentloop$_{analytic}$ model* consists of two pairs of current loops. The *currentloop$_{analytic}$ model* used ideal infinitely thin current loops and its configuration is shown in Fig. 4.2. The loop currents I_1 and I_2 are 6,228 and 22,771 A, respectively. Although these are large currents, this model is intended to only approximate the MROpen^{TM}'s fringe magnetic flux densities for linac simulations. There are no plans to physically build the *currentloop$_{analytic}$ model*.

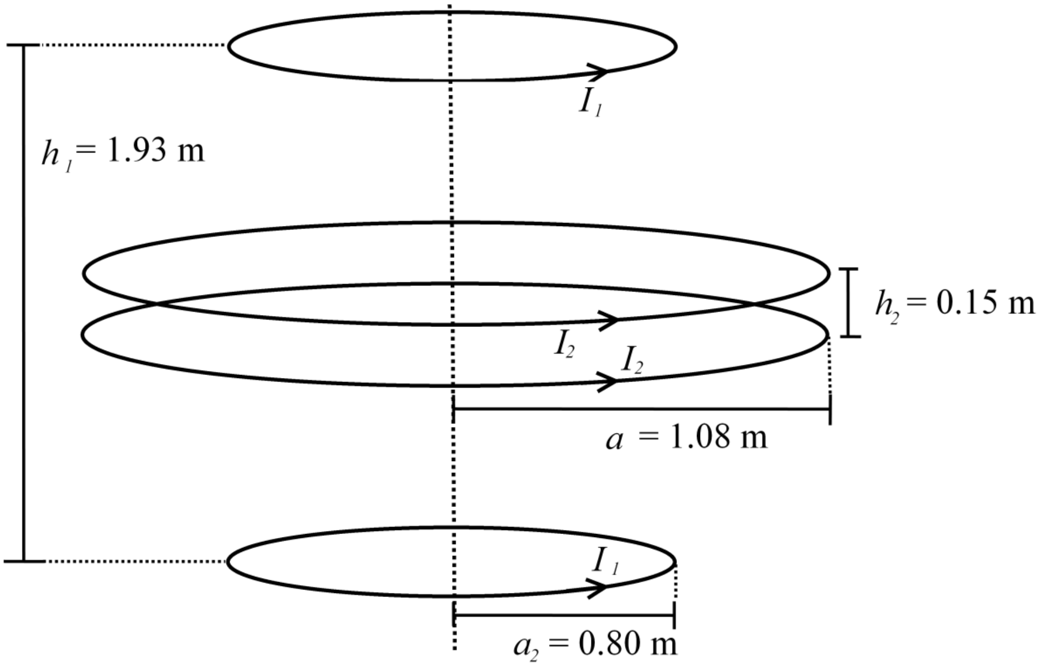

Figure 4.2: A diagram of the *currentloop$_{analytic}$ model* showing the current loop configurations.

The optimized *currentloop$_{analytic}$ model* agreed well with the PARAmed magnetic isoline data. Although there is a 12 % discrepancy with the 0.002 T isoline from the PARAmed data, the calculated fringe magnetic flux densities are within a 1.5 % discrepancy elsewhere. A comparison between the calculated fringe magnetic flux densities and the PARAmed data along the magnet's symmetric axis in Fig. 4.2 is shown in Fig. 4.3.

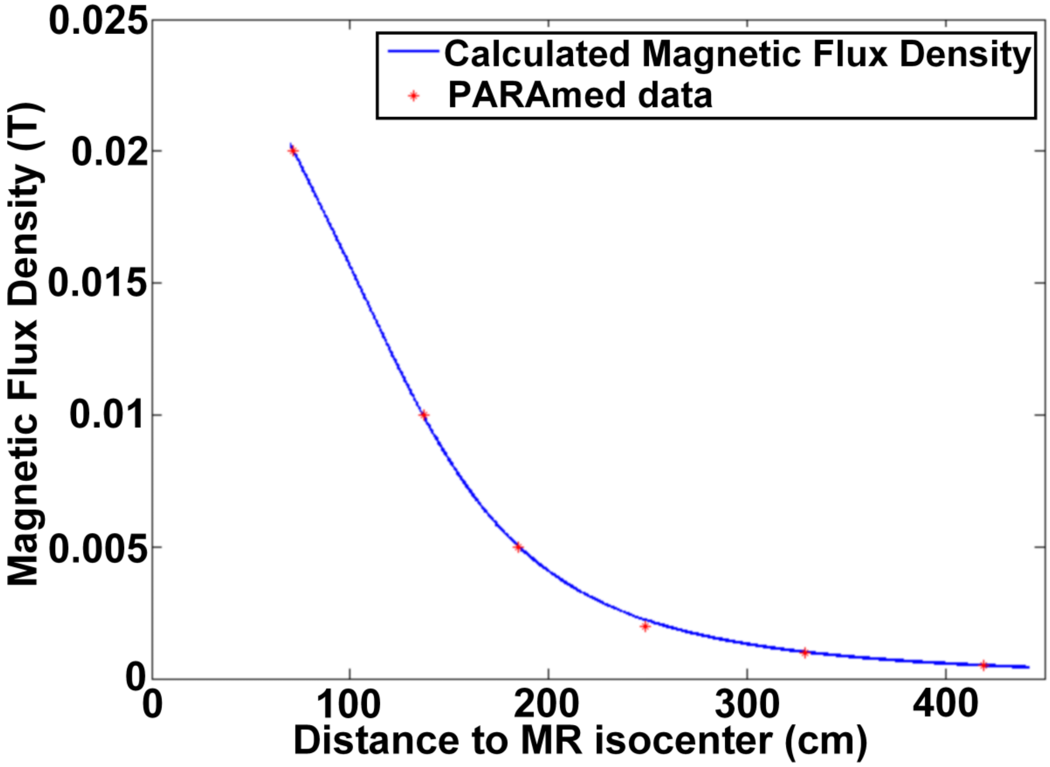

Figure 4.3: The calculated magnetic fields (solid line) and the PARAmed isoline data (dots) along the symmetric axis of the *currentloop$_{analytic}$ model* in Fig. 4.2.

4.3.2 Linac performance in the presence of MR fringe magnetic flux density

The presence of the MR fringe magnetic flux density in the *parallel linac-MR configuration* changes the characteristics of the electron gun's output electron beam. At 1.0, 1.5, and 2.2 m SADs, the expected magnetic flux density magnitudes at the electron gun cathode are 0.011, 0.0049, and 0.0022 T, respectively. The electron gun output phase-space from normal operations (0 T) is shown in Fig. 4.4a while the resulting electron gun output phase-space (Figs 4.4b, 4.4c, and 4.4d) in the presence of the MR's fringe magnetic flux density shows that the electron gun output beam becomes increasingly non-laminar compared to the normal case in Fig. 4.4a. The ε_{rms} (Eq. 2.70) of the electron beams in Fig. 4.4 grow from 0.457π mm-mrad for the 0 T case to 0.858π, 1.597π, and 3.242π mm-mrad for the 0.0022, 0.0049, and 0.011 T cases, respectively.

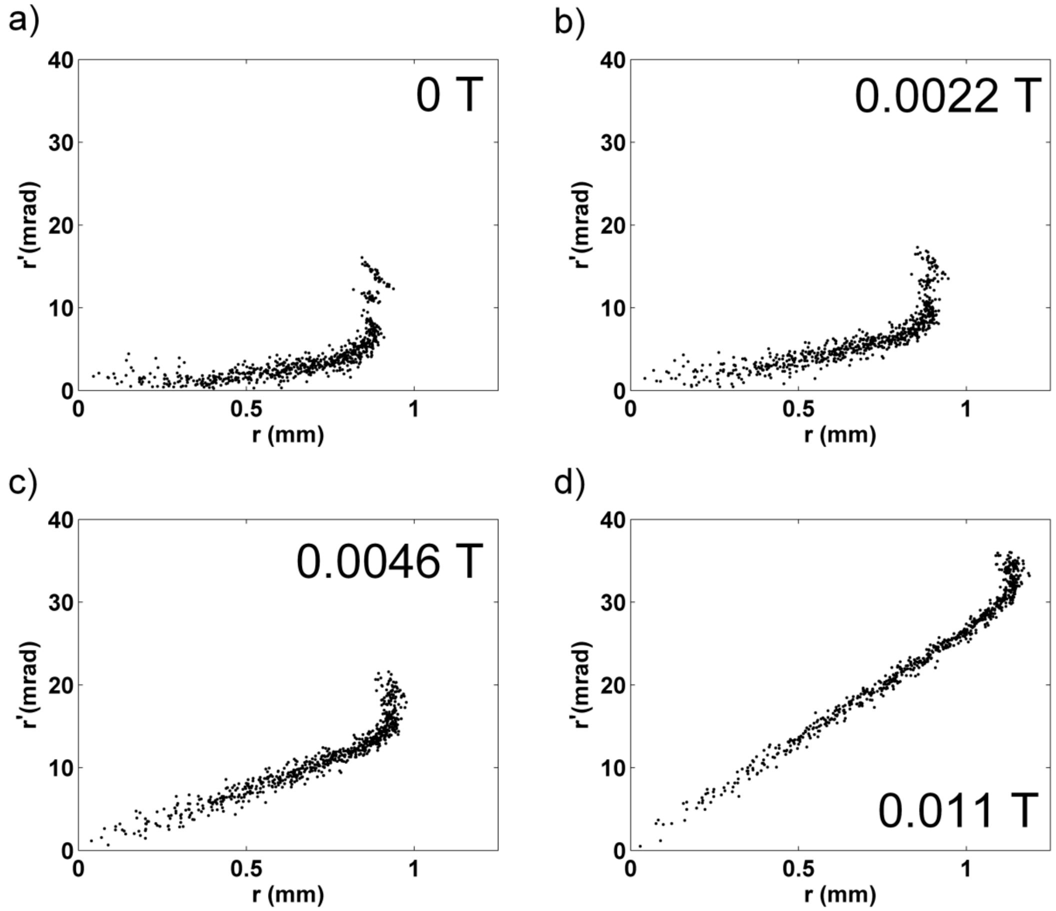

Figure 4.4: The phase-space of the electron gun output beam when a) 0 T, b) 0.0022 T, c) 0.0049 T, and d) 0.011 T MR's fringe magnetic flux densities are present at the electron gun cathode. In the figures, *r* and *r'* are calculated by Eqs 2.68 and 2.69, respectively.

The electron gun output beam is injected into the linac waveguide; because the electron gun and waveguide needed to work as a single unit in the linac, changes in the electron gun output beam characteristics will affect the linac's output (the linac target current). The changes in the electron gun output discussed above resulted in target current losses of 1 ± 1 %, 2 ± 1 %, and 17 ± 1 %, in the presence of 0.0022, 0.0049, and 0.011 T, respectively. Although the MR's fringe magnetic flux densities, in the *parallel linac-MR configuration*, caused a decrease in the linac target current, these fringe magnetic flux densities have an insignificant effect on electron energy distribution at the target (Fig. 4.5). When the 0.011 T fringe magnetic flux density is present, the mean electron energy increased to 5.70 MeV from 5.57 MeV (0 T). Figure 4.5 shows the redistribution of the electron energies as the fringe magnetic flux density magnitude is increased.

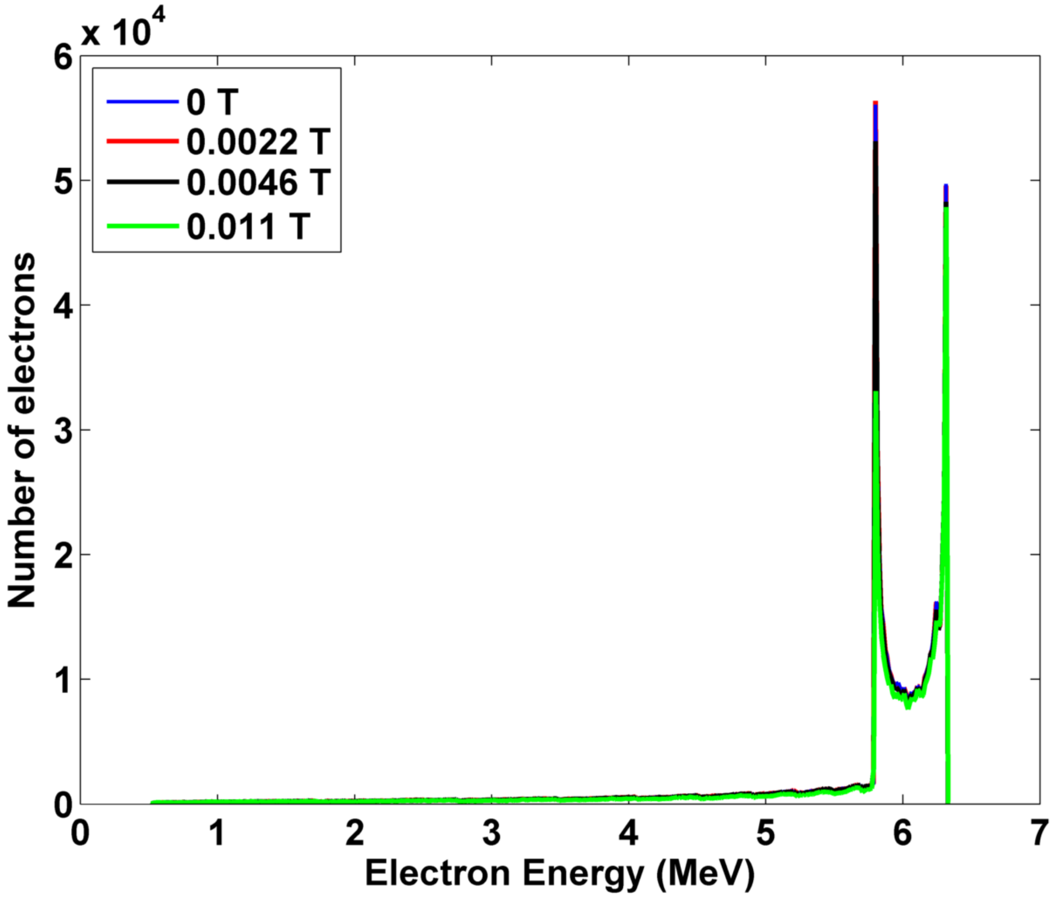

Figure 4.5: The energy distribution of the linac electron beam at the linac target from different MR magnetic flux densities at the electron gun cathode.

The electron beam's spatial distribution (Fig. 4.6) at the target is greatly altered by the MR's parallel fringe magnetic fields. The spatial distributions in Fig. 4.6 are normalized to the peak of the nominal spatial distribution at 0 T. The full width at half (FWHM) of the linac's electron beam at the target increased to 2.11 mm when a 0.011 T MR fringe field is present from its nominal value of 0.14 mm at 0 T; however, the results of the MC simulations from the linac target to the water phantom shows that this altered spatial distribution and the increasing

FWHM of the linac's electron beam has an insignificant effect on the treatment beams cross-line profiles.

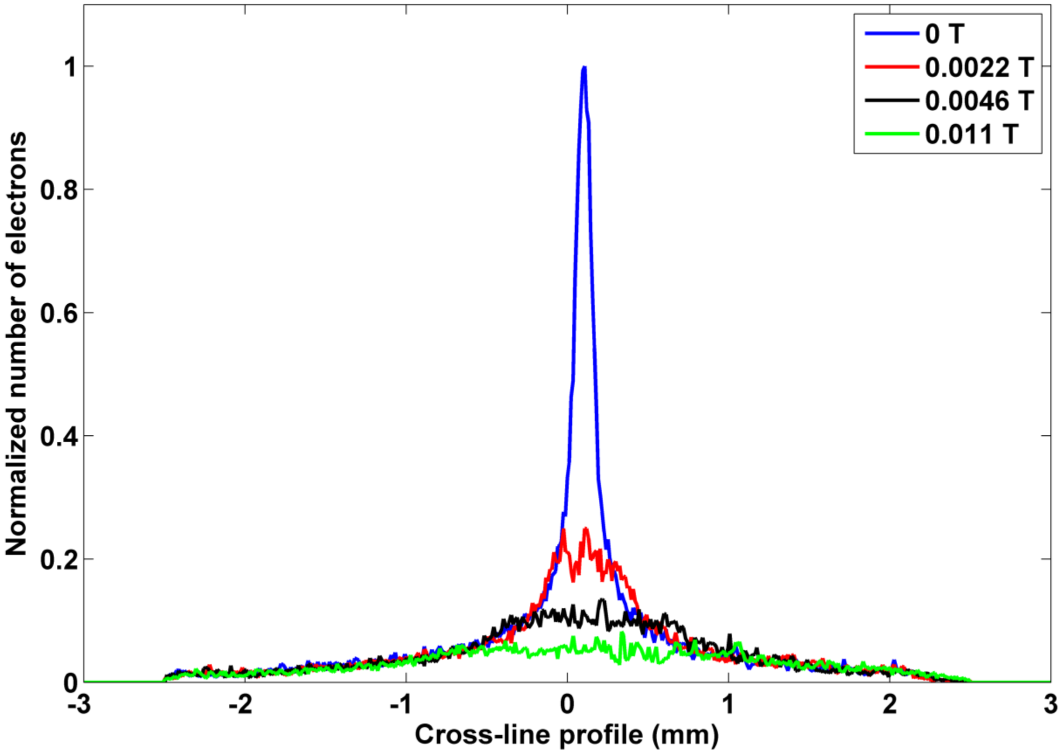

Figure 4.6: The cross-line spatial distribution of the electron beam at the target for the normal 0 T case and three linac-MR SAD setups.

MC simulations of a 40 x 40 cm^2 treatment beam in a water phantom were preformed in collaboration with another student to investigate the effects of the altered electron beam at the target on the treatment beam's dosimetry.[6] The MC simulations were performed using BEAMnrc, EGSnrc, and DOSXYZ.[11-13] The BEAMnrc and EGSnrc simulations used a total of 3 x 10^8 initial histories from the PARMELA output phase-space.[6] The field size was set to 40 x 40 cm^2.[6] The electron transport cut-off energies (ECUT) and the photo transport cut-off energies (PCUT) were set to 0.70 and 0.01 MeV, respectively.[6] The dose distributions were simulated in a 66 x 66 x 48 cm^3 water tank using DOSXYZ, a MC dose calculation package.[6] Each DOSXYZ simulation used the output from BEAMnrc and a total 7 x 10^9 histories.[6] For all the depth dose (DD) simulations, the voxel depth from 0.2 cm to a depth of 1.5 cm and from 0.5 cm to a depth of 30 cm with a lateral voxel dimensions were set to 1 x 1 cm^2.[6] The voxel sizes were set to 1 x 1 x 0.5 cm^3 everywhere except in the penumbra where it was reduced to 0.2 x 1 x 0.5 cm^3.[6] The ECUT and PCUT in the DOSXYZ simulations were set to 0.70 and 0.01 MeV, respectively.[6] The DD curves (Fig. 4.7d) were normalized by the dose at 10 cm depth (D_{10}) and scaled according to the target current.[6] The cross-line dose profiles (Fig. 4.7a-c) were scored at a depth of 1.5 cm and were normalized to the treatment beam's central axis dose (D_{CAX}).[6] From the MC simulations (Fig. 4.7), 96 % of the points match measurements from a Varian 600C linac[6] operating at 0 T within the 1 %/1 mm gamma index criterion.[10] The cross-line dose profiles in Fig. 4.7a-c shows that the treatment beams retain its symmetry[6] in the presence the MR's longitudinal fringe magnetic flux density. As the magnitude of the magnetic flux density is increased,[6] the losses in the target current discussed earlier would result in decreases in the treatment beam's DD in Fig. 4.7d[6] which is the result of decreasing linac dose rate.

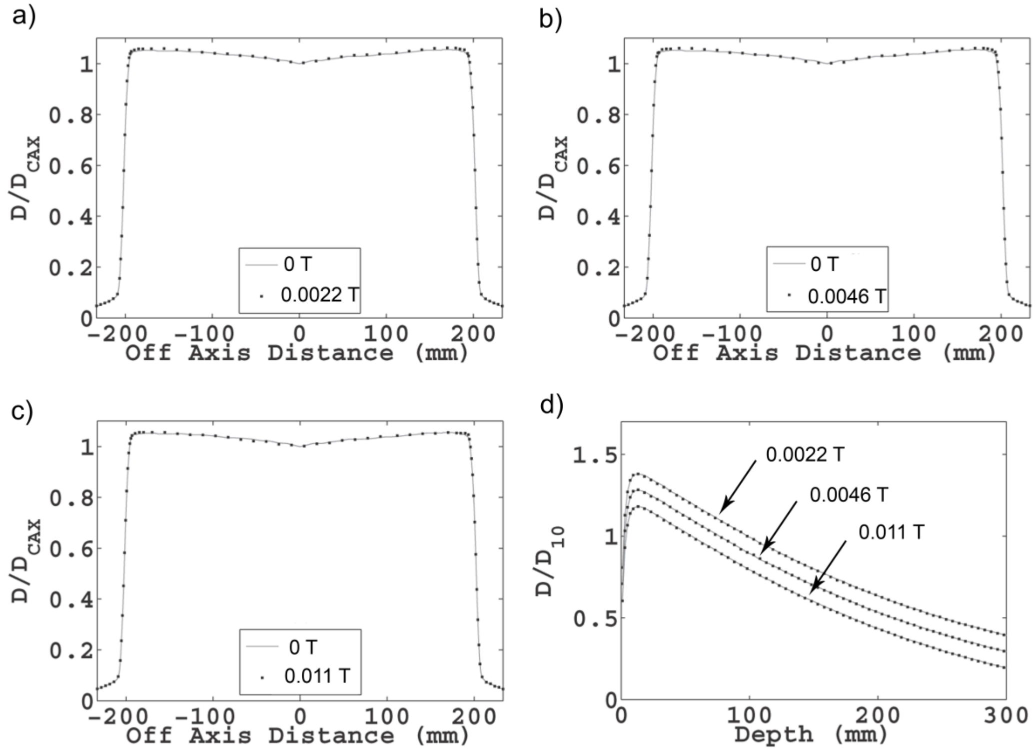

Figure 4.7: MC simulations of a 40 x 40 cm^2 treatment beam were performed in collaboration with another student.[6] The cross-line dose profiles (a-c) at 1.5 cm depth were compared to measurements taken from a linac operating in 0 T. The DD curves in d are from a simulated linac were normalized at the dose at D$_{10}$ but scaled for visual clarity.

A 10 mm off-axis offset was given to the linac to simulate a worst-case in the linac-MR setup error. The 10 mm offset is an exaggerated linac and MR magnet misalignment, which can happen when errors in the commissioning process and/or accidental bumps occur, and represents a worst-case scenario. However, a more realistic offset will be on the order of a few millimetres. The presence of the 10 mm off-axis offset causes an asymmetric fringe magnetic flux density which results in the presence of perpendicular magnetic flux densities;[6] however, only an additional 1 % target current loss was observed in this worst-case. Since the 10 mm offset caused only a 1 % additional target current loss, misalignments of the linac in the *parallel linac-MR configuration* have an insignificant effect on the linac target current and in general the dose rate.

4.3.3 Linac performance in the presence of longitudinal homogeneous magnetic flux densities

Because other MR imagers can have different fringe magnetic flux densities than the MROpen^{TM}, there is interest in the linac's performance in the presence of magnetic flux densities that are stronger and weaker than the MROpen^{TM}'s fringe fields. Different fringe magnetic flux densities can be caused by the differences in MR magnet design, a different B_0 strength, and changes in linac and MR SAD setups. The fringe magnetic flux density drop off from the MROpen^{TM} varies by only 3.6 x 10^{-4} T in the electron gun. When using 0.011 T parallel homogenous magnetic flux densities were used in place of the MR's fringe magnet flux densities for the 1.0 m SAD, the cathode emission, injection, and target currents changed by 0.001 %, 0.001 %, and 1 %, respectively. Therefore, homogeneous magnetic flux densities, which were described in § 4.2.5, can be used to approximate the fringe magnetic flux densities of other MR magnets.

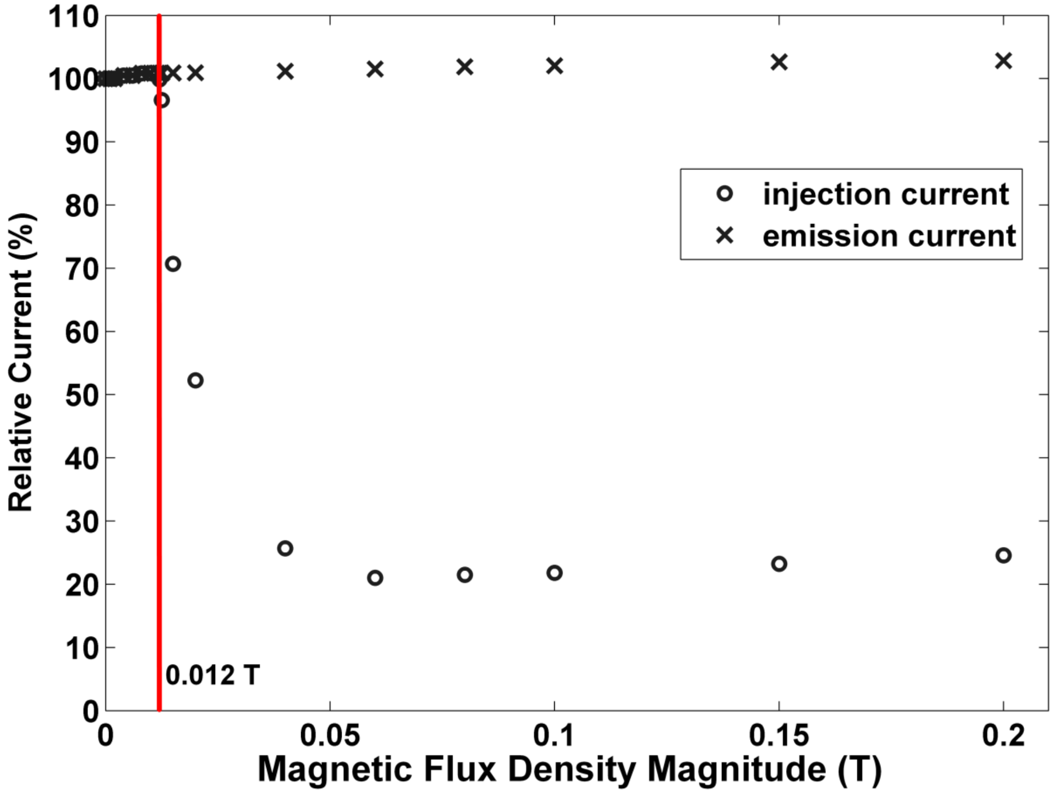

Figure 4.8: The electron gun's cathode emission current and injection current in the presence of parallel magnetic flux densities. The injection current rises slowly, at first but drops when the flux density increases beyond 0.012 T.

The electron gun output beam (the waveguide's injection current) in Fig. 4.8 rises slowly to 101 % until 0.012 T. This increased injection current is caused by the increasing cathode emission current (Fig. 4.8) as the magnetic flux density is increased. The parallel magnetic fields remove the space charge cloud in front of the cathode which causes the electron gun to become less space-charge limited and. This causes the cathode to emit more electrons[6] resulting in the increasing cathode emission and injection currents seen in Fig. 4.8. As the magnetic flux density is further increased, the injection current sharply drop until it reaches its minimum value of 21 % at 0.06 T. The sharp drop in the injection current is explained by the collimation of the electron beam by the anode as shown in Fig. 4.9. As the emission current increased, the electron beam's width increases as well. At 0.012 T, the beam width increased beyond the anode's radius, which results in parts of the electron beam to impact onto the anode[6] (Fig. 4.9). As the magnetic flux density is increased, more electrons impact onto the anode[6] and are removed from the injection beam. Beyond 0.06 T, the injection current recovers to 24.6 % at 0.2 T, which could be caused by collimation from the longitudinal magnetic flux densities.

In the region before the sharp drop in the injection current, the target current steadily drops although the injection current rose slightly. The longitudinal magnetic fields alter the characteristics of the injection beam, such as its laminarness (Fig. 4.4), which has a pre-focussing effect in the electron gun output beam. This change in electron optics (Fig. 4.9) makes the waveguide is less efficient at capturing and accelerating the injected electron beam.[6]

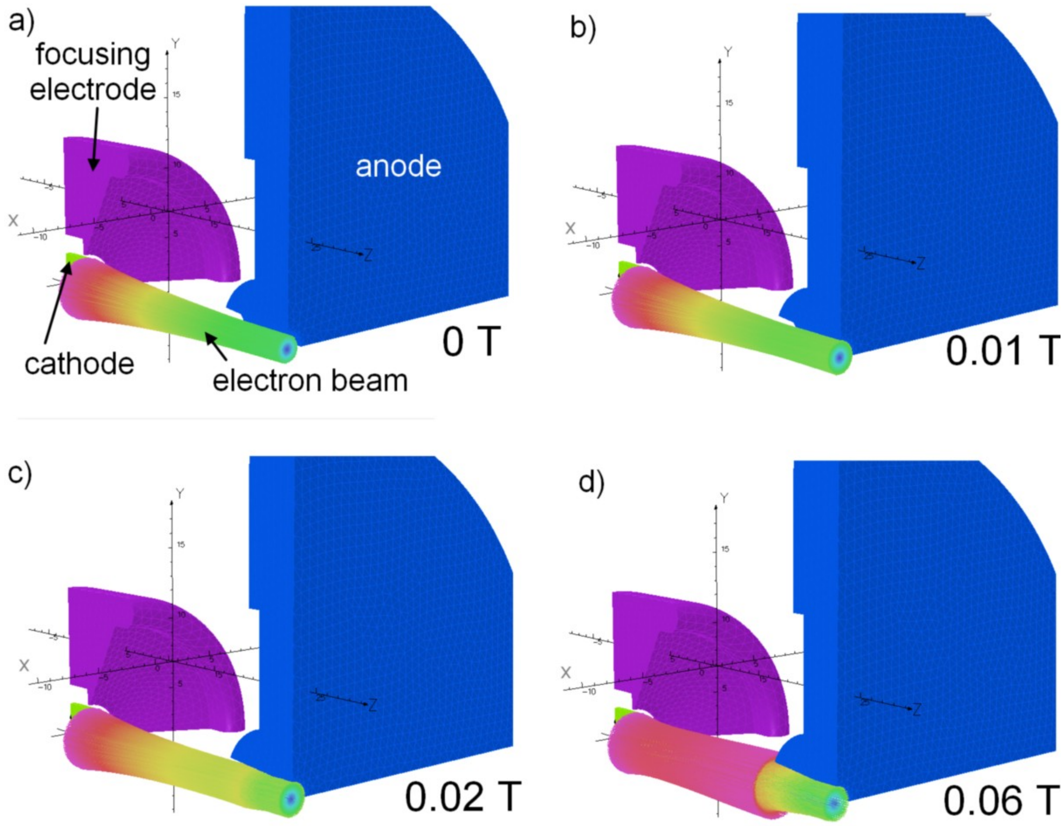

Figure 4.9: A quarter cut-out of the electron gun is shown to show its electron beam in the normal 0 T case and three parallel homogenous fringe magnetic flux densities.

Figure 4.1 shows the target current drop off as the homogenous magnetic flux density is increased. The target current continually drops from its nominal value in 0 T until it reaches its minimum value of 21.7 % in the presence of 0.06 T longitudinal magnetic flux densities. Beyond this magnetic flux density, the target current starts to rise slowly to 29.4 % when 0.2 T longitudinal magnetic flux densities are present.

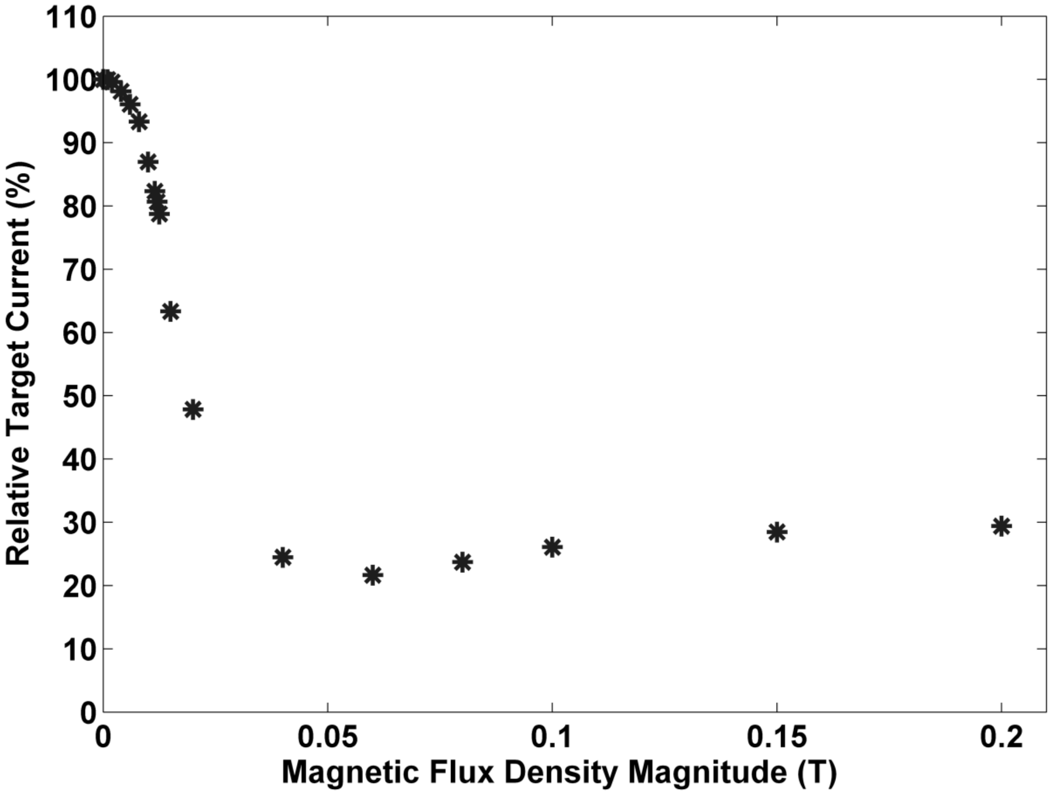

Figure 4.10: The relative target current for a linac in the presence of homogenous fringe magnetic flux densities.

These results (Figs 4.8 and 4.10) are a valid approximation to the emission, injection, and target currents' behaviours in the presence of other MR's fringe magnetic flux densities when a variation of 3.6 x 10^{-4} T or less occurs in the electron gun of a *parallel linac-MR configuration*.

4.4 Summary

The effect of longitudinal magnetic flux densities on a simulated 6 MV in-line linac was quantified in this chapter. Longitudinal magnetic flux densities caused growth in the target beam's FWHM as well as target current loss. Insignificant changes to electron energy distribution and mean electron energy was observed. Although the target beam's FWHM grew and the beam's spatial distribution was altered (Fig. 4.6), MC simulations show that the dosimetric symmetry of the treatment beam was not lost[6] (Fig. 4.7). The lower target current when longitudinal magnetic flux densities are present led to decreased DD’s[6] (Fig. 4.7) or dose rates. The lost in the target current can be traced back to the changes in the laminarness of the waveguide injection current. Therefore, if the lost target current were to be recovered, remedies must regain the nominal laminar injection current. These remedies could include an electron gun redesign or the use of either passive or active magnetic shielding. CHAPTER 5 discusses the use of either passive or active magnetic shielding as a remedy for lost target current.

4.5 References

[1] J. St. Aubin, S. Steciw and B. G. Fallone. "The design of a simulated in-line side-coupled 6 MV linear accelerator waveguide," Med. Phys., **37,** 466-476, (2010).

[2] J. St. Aubin, S. Steciw, C. Kirkby and B. G. Fallone. "An integrated 6 MV linear accelerator model from electron gun to dose in a water tank," Med. Phys., **37,** 2279-2288, (2010).

[3] J. S. Aubin, S. Steciw and B. G. Fallone. "Effect of transverse magnetic fields on a simulated in-line 6 MV linac," Phys. Med. Biol., **55**, 4861, (2010).

[4] J. St. Aubin, S. Steciw and B. G. Fallone. "Magnetic decoupling of the linac in a low field biplanar linac-MR system," Med. Phys., **37**, 4755-4761, (2010).

[5] J. St. Aubin. *Three dimensional simulation and magnetic decoupling of the linac in a linac-MR system*. Doctoral dissertation, University of Alberta, Edmonton, Alberta, Canada (2010).

[6] J. St. Aubin, D. M. Santos, S. Steciw and B. G. Fallone. "Effect of longitudinal magnetic fields on a simulated in-line 6 MV linac," Med. Phys., **37**, 4916-4923, (2010).

[7] J. Pierce R. *Theory and Design of Electron Beams* (D. Van Mostrand Company, Inc., Toronto, 1949).

[8] C. D. Child. "Discharge From Hot CaO," Phys. Rev. (Series I), **32**, 492-511, (1911).

[9] M. de Berg, O. Cheong, M. van Kreveld and M. Overmars. *Computational Geometry: Algorithms and Applications* (Springer-Verlag, Berlin, 2008).

[10] D. A. Low, W. B. Harms, S. Mutic and J. A. Purdy. "A technique for the quantitative evaluation of dose distributions," Med. Phys., **25,** 656-661, (1998).

[11] D. W. O. Rogers, B. A. Faddegon, G. X. Ding, C. M. Ma, J. We and T. R. Mackie. "BEAM: A Monte Carlo code to simulate radiotherapy treatment units," Med. Phys., **22,** 503-524, (1995).

[12] C. M. Ma, B. A. Faddegon, D. W. O. Rogers and T. R. Mackie. "Accurate characterization of Monte Carlo calculated electron beams for radiotherapy," Med. Phys., **24,** 401-416, (1997).

[13] I. Kawrakow, D. W. O. Rogers and B. R. B. Walters. "Large efficiency improvements in BEAMnrc using directional bremsstrahlung splitting," Med. Phys., **31,** 2883-2898, (2004).

CHAPTER 5 : MAGNETIC SHIELDING INVESTIGATION FOR A 6 MV IN-LINE LINAC WITHIN THE PARALLEL CONFIGURATION OF A LINAC-MR SYSTEM

A version of this chapter has been submitted for publication. D. M. Santos, J. St. Aubin, B. G. Fallone, S. Steciw, "Magnetic shielding investigation for a 6 MV in-line linac within the parallel configuration of a linac-MR system," Med. Phys. (submitted on Jun 2011).

5.1 Introduction

CHAPTER 4 discussed the effects of longitudinal/parallel magnetic flux densities on the linac performance. It was shown that, although the parallel magnetic fields caused target current loss, the treatment beam retains its dosimetric symmetry.[1] The lost target current led to fewer electrons available for X-ray production. Therefore, decreases in linac output (such as the dose rate) occur as shown by the DD's curves in Fig. 4.7d. This lost target current is a result of the altered electron gun's output current (the injection current into the linac) characteristics caused by magnetic deflections in the electron trajectories. Although the injection current (Fig. 4.8) did increase until a 0.012 T longitudinal magnetic flux density was present, the target current (Fig. 4.1) steadily decreased. Therefore, the electron gun is sensitive to longitudinal magnetic fields, and alterations to its output electron beam caused an undesired target current loss.

This chapter focuses on the recovery of the lost target current caused by magnetic deflections in the *parallel linac-MR configuration*. The lost linac output can be minimized or recovered either by redesigning the electron gun,[1,2] by moving the linac further away from the MR magnets,[1] or by magnetically shielding the electron gun.[1] The electron gun alteration is not very practical, since the design needs to be optimized for each electron gun-to-MR system, and must be redesigned for different electron gun locations and /or MR magnet systems. Moving the linac further away from the MR magnet would be accompanied by a reduction in dose rate due to the effects of the inverse square law; the recovered target current would be out weighted by the loss in dose rate as the linac-MR SAD is increased. In addition, because of the increased distance linac-MR SAD, more space would be required to house such a linac-MR system. Although active magnetic shields needs to be reoptimized for each electron gun-to-MR setup, the passive magnetic shields are more robust than the electron gun redesign remedy discussed earlier. If a passive magnetic shield can adequately shield the linac from a magnetic flux density such as a 0.011 T longitudinal magnetic flux density at the electron gun cathode, the same passive magnetic shield can successfully shield the linac from weaker magnetic flux densities. Therefore, the use of a magnetic shield may be advantageous to minimize or recover the loss in the linac's target current caused by magnetic deflection since it would allow flexibility for different linac-MR setups.

This study investigates the linac performance (as measured by the changes in the linac target current) when either passive or active magnetic shields are used in a *parallel linac-MR configuration* (Fig. 1.3). For part of this study, the fringe magnetic flux densities that emulate the PARAmed 0.5 T MROpen^{TM} fringe fields were used.

5.2 Methods

5.2.1 Electron gun's casing

The steel casing surrounding the electron gun (illustrated in Fig. 5.1) is roughly 1-mm-thick and is ferromagnetic. Because its presence has a nontrivial effect on the MR's fringe magnetic flux densities, it was included in the FEM simulation with *currentloop$_{FEM}$ model* discussed later in § 5.2.2. The magnetization curve[3] of AISI 1020 carbon steel was used to calculate its relative permeability. There is a hole that is approximately 1 cm in diameter on the side of the gun casing which allows access to the electron gun cables. The hole's effects on the magnetic field inside the electron gun were investigated by comparing the magnetic flux density in the electron gun with and without this hole.

5.2.2 The currentloop models

The *currentloop$_{analytic}$ model*, which consisted of two pairs of current loops (Fig. 4.2) and emulated the fringe magnetic flux densities of a PARAmed 0.5 T MROpen^{TM} system was created as described in CHAPTER 4 through the superposition of analytic current loops[1] calculated using the Biot-Savart law (§ 2.1.1). The *currentloop$_{analytic}$ model* was generated in order to determine the vector components of the fringe magnetic field (required for the particle simulations) which was not provided in the isoline data the manufacturer supplied. This fringe magnetic model was based on the manufacturer-supplied data which consisted of the 0.0005, 0.001, 0.002, 0.005, 0.01, and 0.02 T isolines in the *xz*-plane. Due to the axisymmetric nature of the MROpen$^{\text{TM}}$'s fringe magnetic flux densities, a current loop model can accurately define its fields.

The commercially available MROpen$^{\text{TM}}$ may need modification when it is integrated into the *parallel linac-MR configuration*. Therefore, these emulated magnetic flux density isolines may vary slightly from the modified MROpen$^{\text{TM}}$ system. However, it is currently unknown how these modifications would affect the MROpen$^{\text{TM}}$'s fringe magnetic flux densities, so the current fringe magnetic flux densities are used in this study to illustrate the feasibility of shielding the linac from an MR system.

Due to the non-linear PDEs which are required to be solved to determine the change in the fringe magnetic flux densities caused by the presence of ferromagnetic shielding structures, the *currentloop$_{analytic}$ model* could not be used when calculating the magnetic flux density changes in the presence of ferromagnetic shielding structures. In order to overcome this limitation, the *currentloop$_{analytic}$ model* was recalculated using the 3D FEM package COMSOL, which is capable of accurately solving the required non-linear PDEs. It should be noted that the support structures seen in Fig. 1.3 were made from non-magnetic material and thus will not alter the MR's fringe magnetic flux densities. Therefore, this investigation holds for any orientation with respect to the support structures shown in Fig. 1.3.

The numerical (FEM) current loop model, which will be referred to as *currentloop$_{FEM}$ model* used the optimized current loop parameters (the loop currents, the loop radii, the separation distance of each current loop pair, and the number of current loop pairs) from the *currentloop*$_{analytic}$ *model* discussed in § 4.3.1. This and all subsequent FEM simulations used quadratic vector basis functions for the tetrahedral finite elements which were optimized using Delaunay triangulation.[4] For each simulation, the average mesh density was between 0.219 tetrahedral elements/mm^3 and 3.3 tetrahedral elements/mm^3. In order to incorporate the open boundary conditions in the *currentloop*$_{FEM}$ *model*, the natural Neumann boundary conditions were specified at the external mesh boundaries. Each simulation used an iterative solver (*FGMRES*[5]) with a *Geometric Multigrid* preconditioner[6] to calculate the magnetic flux densities in the region of interest (the electron gun, waveguide, gun casing, and magnetic shielding).

In order to validate the accuracy of the *currentloop*$_{FEM}$ *model*, the fringe magnitude of the magnetic flux density were compared to the manufacturer supplied isoline data. Only one plane (*xz*-plane) was used for the validation since the manufacturer supplied fringe magnetic flux density isolines show that the isolines are axisymmetric in the region where the linac will be placed. The *currentloop*$_{FEM}$ *model* was used to generate magnetic fields at any arbitrary points in 3D space as needed by the linac simulation.

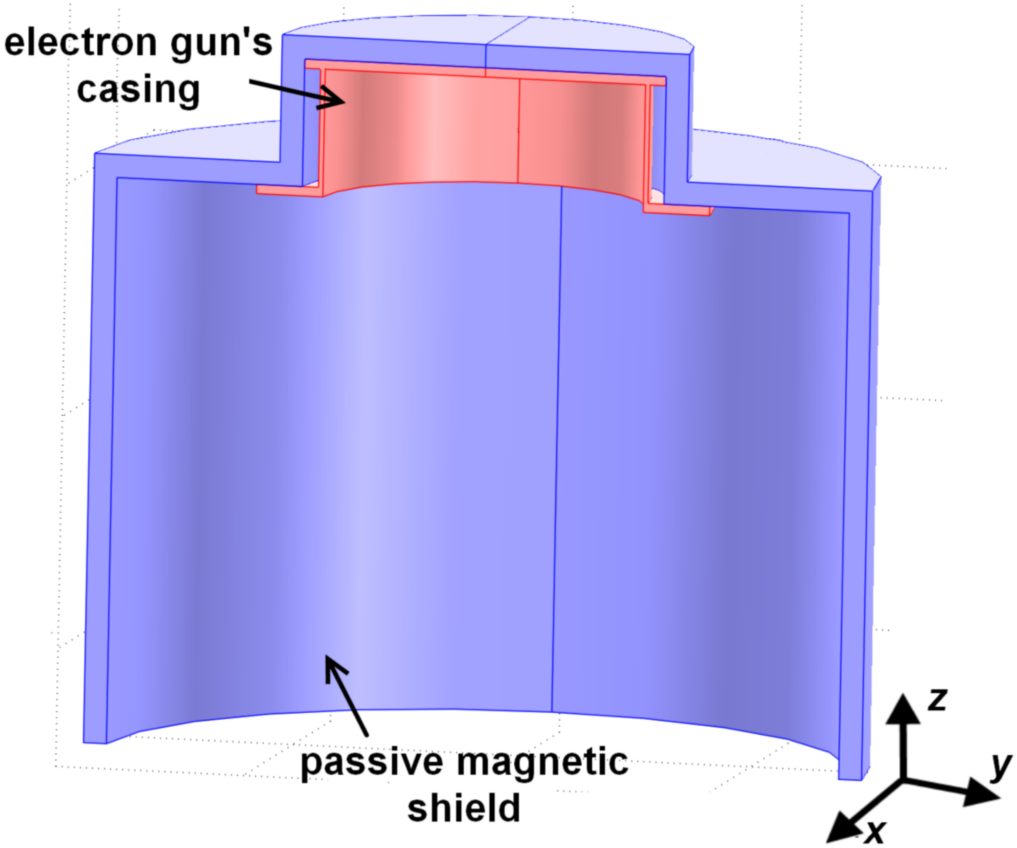

Figure 5.1: Cross-section of a passive magnetic shield setup.

Passive magnetic shielding techniques were studied by surrounding the electron gun's casing and waveguide with a steel cylinder with a metal cap at one end (Fig. 5.1). The location of the passive shield on the linac is shown in Fig. 5.2a. The magnetization curve[3] of AISI 1020 carbon steel was used to calculate the relative permeability of the passive magnetic shield. Passive shield thicknesses from 0.75 mm to 15 mm and inner lengths from 26.5 mm to 306.5 mm were simulated in the *currentloop*$_{FEM}$ *model*. Because the 24.5-mm-long electron gun is the most sensitive component to longitudinal magnetic fields,[1] it is always shielded. The electron gun with its gun casing is

26.5 mm long. The combined length of the electron with its gun casing and the waveguide is 306.5 mm. The maximum passive shield length of 306.5 was chosen because the linac needs to be mounted onto the linac-MR system. Having a longer passive shield would cause problems when installing the linac and passive shield onto the linac-MR. The 3D FEM magnetic flux density solutions incorporating the passive shielding and gun casing were solved in COMSOL and served as an input to both the electron gun simulation[7] and waveguide simulation[8].

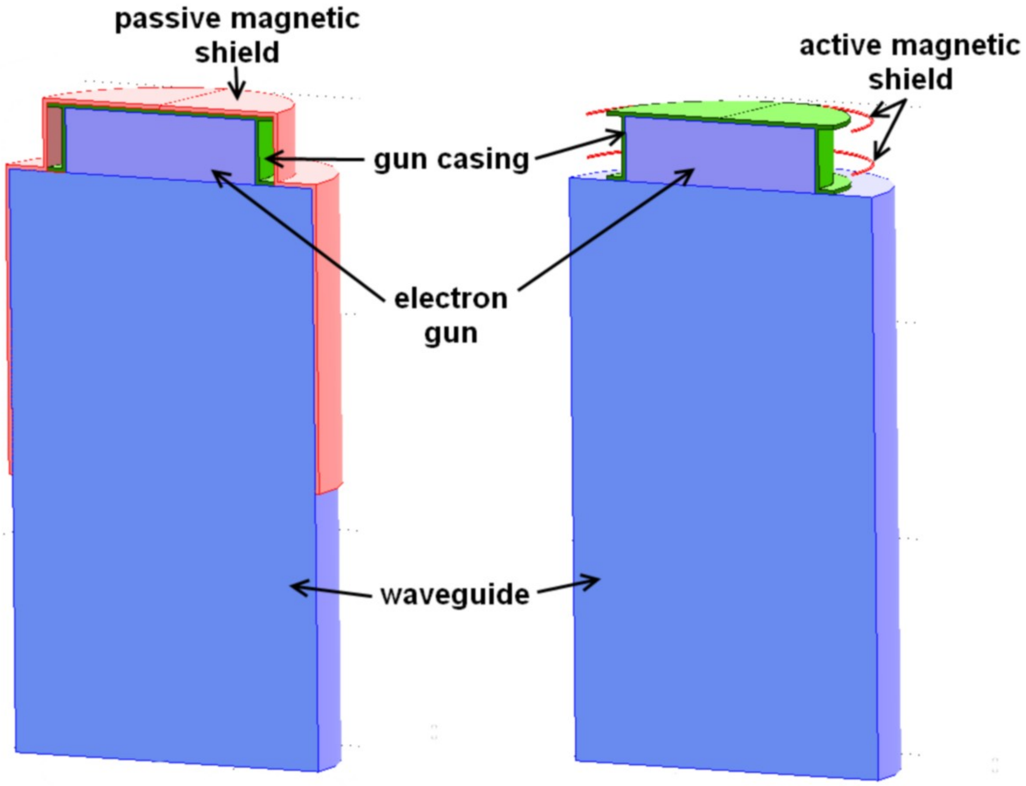

Figure 5.2: A schematic diagram showing the location of the a) passive and b) active magnetic shields relative to the linac electron gun and waveguide.

Active magnetic shielding techniques were studied by adding active shield coils, which consist of current loops around the electron gun's casing (Fig. 5.2b) since the electron gun is the most sensitive part of the linac to longitudinal magnetic flux densities.[1] The magnetic flux densities from these coils were optimized to cancel out the MR's fringe magnetic flux densities inside the electron gun. The electron gun's casing was included in the simulations since it is integral to the electron gun's construction. Therefore, the net MR's fringe flux densities inside the electron gun B_{net}^{i} was added in quadrature (Eq. 5.1) where i is the mesh node number and N is the total number of mesh nodes in the electron gun. The objective function f was minimized.

$$f = \sum_{i=1}^{N} \left(B_{net}^{i}\right)^{2} \qquad 5.1$$

The total currents for each active shield coils, their separation distance d_{shield}, and their location relative to the electron gun cathode were optimized to minimize the net magnetic flux density in the electron gun. Because of the limited space available for magnetic shielding around the electron gun in the linac-MR, the radius of each active shield coil was fixed to 55 mm. The total current in each shield coils must be in the same direction to avoid solutions where the coils would work against each other. The separation distance must be in between 0 and 30 mm because of the limited space available for shielding around the electron gun. A Matlab built-in function (*fmincon*), which uses sequential quadratic programming,[9-12] was used to optimize the active shield instead of the MC optimization[1] from § 3.4.1 because of its more rapid convergence. The FEM magnetic flux density solutions in the electron gun and waveguide served as inputs to the electron gun simulation[7] and waveguide simulation[8], respectively.

Figure 5.3 shows the general process for both active and passive magnetic shielding techniques.

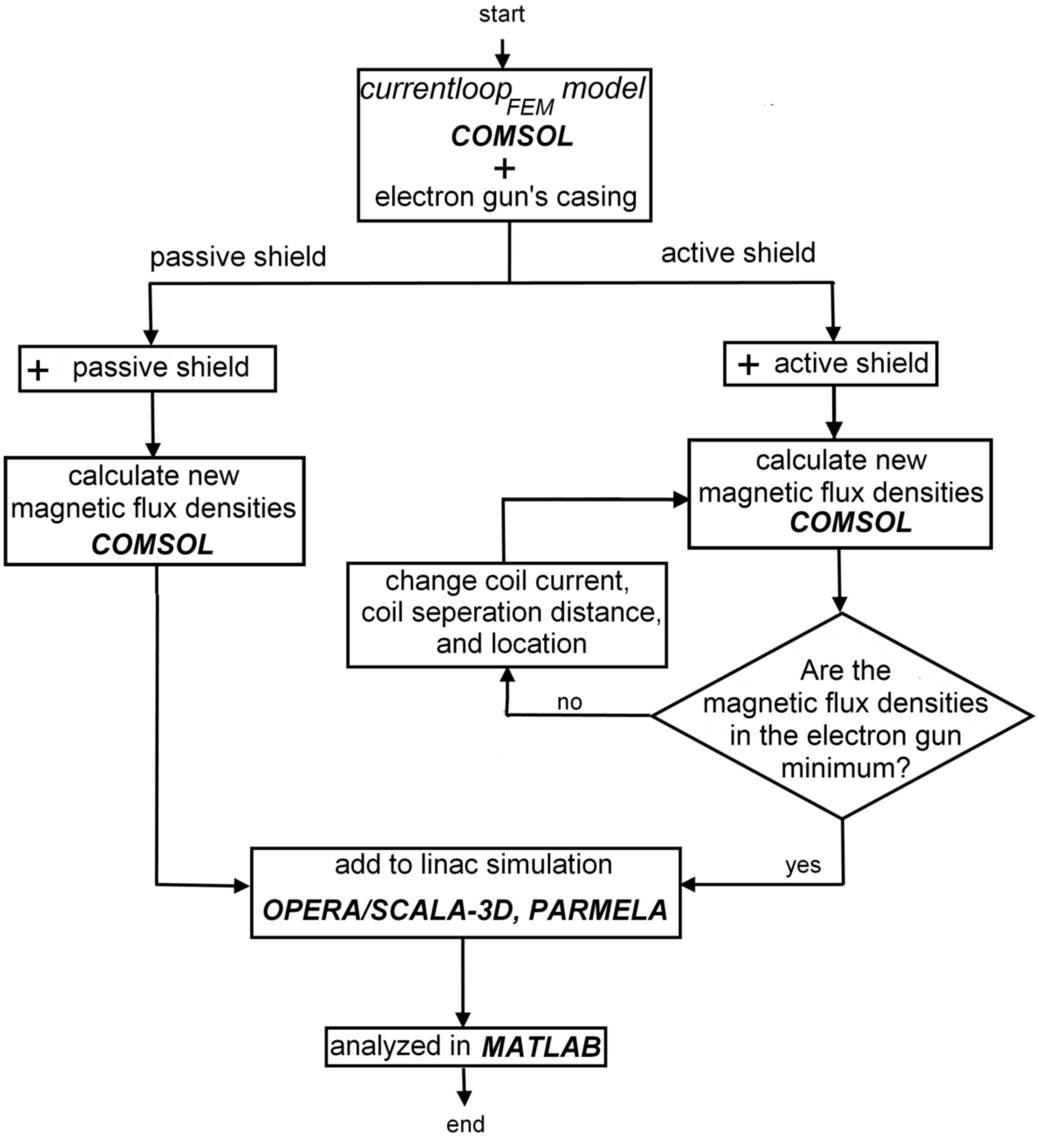

Figure 5.3: A flow diagram showing the passive and active magnetic shielding process.

Calculations estimating the homogeneity in the MR field-of-view were performed on our *currentloop$_{FEM}$ model* to assess the effect of the magnetic shield’s presence on the MR’s imaging volume. Although the manufacturer provided data contained a map of only the MROpen^{TM}'s fringe magnetic flux density isolines, the MROpen^{TM} discussed in this work is a 0.5 T MR imager. Therefore, the magnetic flux density in the imaging volume is assumed to be 0.5 T, as reflected in Eqs 5.2 and 5.3. The resulting magnetic flux density offset ΔB_0 (in ppm) at the isocenter of the magnet and the maximum change in the magnetic flux density ΔB_{DSV} (in ppm) at the 30-cm and 50-cm diametrical spherical volume (DSV) were calculated from Eqs 5.2 and 5.3.

$$\Delta B_0 = \left(\frac{\left| B_c - B_c^{shielded} \right|}{0.5T} \right) \times 10^6 \qquad 5.2$$

$$\Delta B_{DSV} = \left(\frac{max\left(\left| B_{DSV} - B_{DSV}^{shielded} \right| \right)}{0.5T} \right) \times 10^6 \qquad 5.3$$

In Eqs 5.2 and 5.3, B_c and $B_c^{shielded}$ are the magnetic flux densities at the isocenter of the magnet with and without the linac's magnetic shield, respectively. Similarly, B_{DSV} and $B_{DSV}^{shielded}$ are the magnetic fields at the DSV surface from the magnet with and without the linac's magnetic shield, respectively. Since ΔB_0 would cause only a change in B_0, the inhomogeneity in ppm for 30-cm and 50-cm DSV was calculated by subtracting ΔB_0 from ΔB_{DSV} for each spherical volume.

To study the passively shielded linac performance in the presence of other MR magnets with weaker or stronger fringe magnetic flux densities than the MROpen^{TM} imager, homogeneous magnetic fields (from 0 T to 0.2 T) were used. The work discussed in § 4.3 showed that the presence of longitudinal magnetic flux densities caused alterations (Fig. 4.4) to the characteristics of the electron gun output beam. These alterations resulted in lost target current (Fig. 4.1) although the electron output current increased (Fig. 4.8). Therefore, the lost linac output occurring in the presence of the longitudinal magnetic flux densities was solely due to the changes in the electron gun's output.[1] Homogeneous magnetic flux densities is a reasonable approximation for larger (and smaller) fringe magnetic flux densities since the magnetic flux densities over the length of the electron gun varies very slowly,[1] which is a change of 3.6×10^{-4} T. When the MR fringe magnetic flux densities (which is 0.011 T at the electron gun cathode) are replaced by 0.011 T parallel homogenous magnetic flux densities, the cathode emission, injection, and target current changed by 0.001 %, 0.001 %, and 1 %, respectively. Therefore, longitudinal homogenous magnetic flux densities can be used as a surrogate for other MR's magnets when the fringe magnetic flux densities in the electron gun change by 3.6×10^{-4} T or less. For this part of the study, the electron gun's casing was incorporated in all of the FEM simulations as well. Passive magnetic shields with thicknesses from 0 mm to 10 mm were simulated. However, the passive shield length remained fixed to 146.5 mm for simplicity. The reason for using this shield length will be discussed later in § 5.3.5. The 3D FEM magnetic flux density solutions were calculated in COMSOL and served as an input to both the electron gun simulation[7] and waveguide simulation[8], respectively.

5.2.3 In-house-designed MR imager for our linac-MR system

Modifications to the standard, commercially available PARAmed 0.5 T MROpen^{TM} was needed because there is ferromagnetic magnetic material that cover the bore of its superconducting coil magnets. Because the *parallel linac-MR configuration* requires the linac's treatment beam to pass through one to the magnet pole's bore, the removal of this material from one of the magnet pole is necessary. Another student, Tony Tadic, has modelled this modified MROpen$^{\text{TM}}$ and the surrounding steel structures such as the linac mounting flange, in a FEM software called OPERA-3D/TUSCA from (Cobham Technical Services, Kidlington, UK), which will be referred to as TUSCA; this magnet model will be referred to as the *full magnet*$_{FEM}$ *model* in this thesis. Furthermore, the linac target in the *full magnet*$_{FEM}$ *model* was moved from 1.0 m SAD to 1.26 m SAD. Three passive shield scenarios were investigated using the *full magnet*$_{FEM}$ *model*: when only the gun's casing was present, when a 25.4-mm-thick steel cylinder surrounded the linac and gun's casing, and when a 5-mm-thick, 146.5-mm-long passive shield surrounded the linac and gun's casing. The magnetic flux densities in the electron gun and waveguide from the three scenarios were solved in TUSCA and served as an input to the electron gun simulation[7] and waveguide simulation[8], respectively.

5.2.4 Linac simulation

The linac simulation is described in § 4.2. It consists of a 3D electron gun simulation[7] and a 3D waveguide simulation[8], which were both described in § 4.2.6. The magnetic flux density solutions from models described in § 5.2.2 (*currentloop*$_{FEM}$ *model*) and § 5.2.3 (*full magnet*$_{FEM}$ *model*) were added to our linac simulation[1,7,8] as external magnetic flux density maps using the procedure described earlier in § 4.2.6.

MC simulation for modeling the dose distributions were not performed for this portion of the study since it was shown in CHAPTER 4 that the longitudinal magnetic flux densities do not affect the linac's treatment beam's profile symmetry or depth dose characteristics.[1] It was shown that greater than 96 % of all points met a 1 %/1 mm gamma index criterion in longitudinal magnetic flux densities up to 0.011 T.[1] It was also clearly shown that the target current (and thus dose rate) dropped as a result of electron losses within the electron gun.[1] Therefore, the target current was chosen as an end point for the magnetic shielding study since target current losses in the presence of longitudinal magnetic flux densities is an indirect measure of how much dose rate would be lost. In a clinical setting, a moderate reduction in the dose rate, such as the previously observed 17 % lost[1] in the presence of a 0.011 T MR's fringe magnetic flux densities, can be accounted for by an increase in patient treatment time. The focus of this work, however, is to investigate the use of magnetic shielding to recover the lost target current, and therefore restoring the linac to its original 0 T state and keeping the treatment times unchanged.

5.3 Results and discussion

5.3.1 The *currentloop$_{FEM}$ model*

A simulation with no gun casing or linac magnetic shield was used to validate the *currentloop$_{FEM}$ model* against the manufacturer supplied fringe magnetic flux density isoline data in a similar fashion as in the *currentloop*$_{analytic}$ *model* validation[1] described in § 4.2. Since the manufacturer isoline data contained only the magnitude of the magnetic isolines, the magnitude of the magnetic flux densities from the *currentloop*$_{FEM}$ *model* was calculated. A comparison of the magnetic flux densities between the calculated magnetic flux density magnitudes and the manufacturer supplied magnetic isoline data was made to validate the *currentloop*$_{FEM}$ *model*. The validation shows that the magnetic flux density magnitudes from the *currentloop*$_{FEM}$ *model* are within 1.5 % of the manufacturer magnetic isoline data.

Magnetic flux density perturbations that are caused by the presence of a 1 cm hole on the side of the gun casing and passive magnetic shield were insignificant in the electron beam region. The curves in Fig. 5.4 show the magnetic flux density differences between the two electron gun casing simulations (the gun casing with and without the hole) for B_x, B_y, B_z (Figs 5.4a, 5.4b, and 5.4c, respectively) along the central axis of the electron gun and along 3 mm off-axis furthest from and nearest to the gun casing's hole. The ±3 mm off-axis lines in Fig. 5.4 represent the maximum radius where the electron beam is present during the electron gun operations. In the region where the electron beam is present, only a maximum difference of 5.13 x 10^{-5} T occurs in B_z. This field strength is comparable to the Earth's field since the linac (Varian 600C) used in this operates in presences of this field.

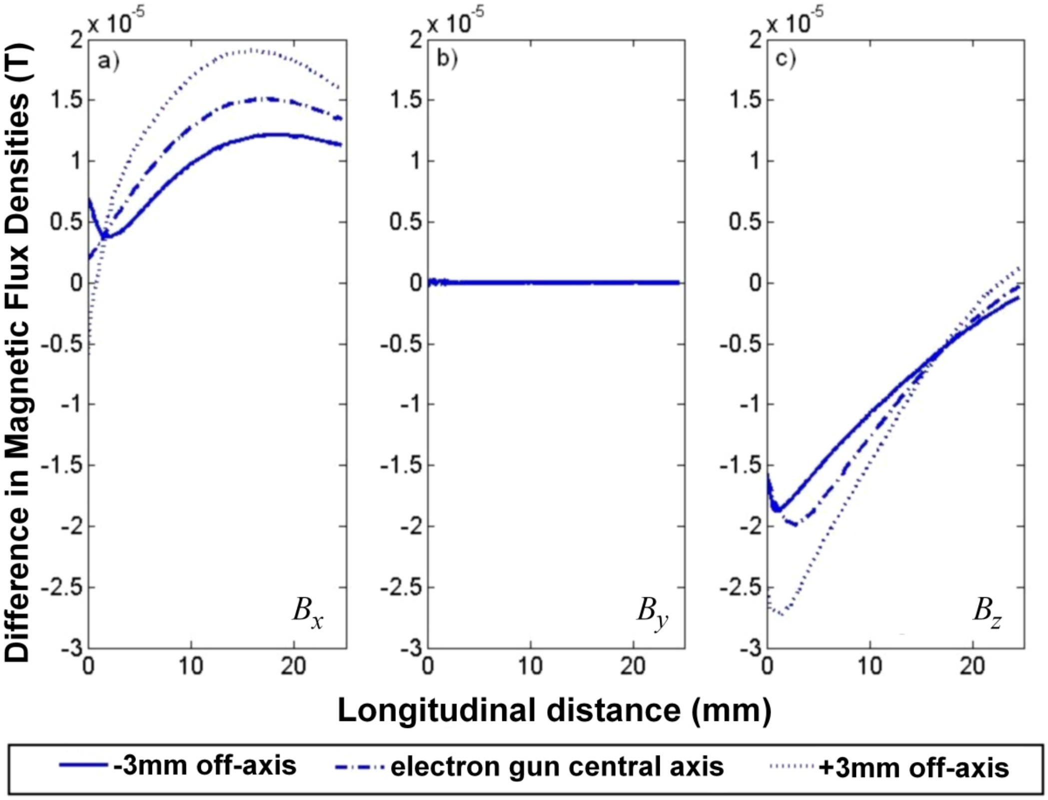

Figure 5.4: Plots of the differences in B_x, B_y, and B_z (in a, b, c, respectively), from the gun casing simulations (with and without the 1 cm hole on its side). The differences are plotted along the electron gun's central axis and ±3 mm off-axis.

Since the Varian 600C operates normally in this field strength, the hole on the gun casing has an insignificant effect on its output current and emittance ε_{rms} (Eq. 2.70), which is a quantitative measure of the beam's laminar flow.[18,19]

The electron gun output current is 362.75 mA and remains constant in both simulations described earlier. The ε_{rms} of the output beam are 3.560π and 3.553π mm-mrad for the simulation with the gun casing with and without the hole, respectively. Since there is less than 1 % difference between the two values, the presence of the hole in the side of the gun casing has an insignificant effect of the magnetic flux densities present in the electron beam region.

5.3.2 Electron gun output

Longitudinal magnetic fields have a significant adverse effect on the electron gun output. It causes the electron trajectories at the electron gun's output to become more nonlaminar, where the individual electron trajectories intersect one another to a greater extent. The electron gun's output beam is the waveguide's injection beam. Therefore, the decrease in the injection will ultimately lead to a reduction in the linac's target current, which in turn results in a reduced linac dose rate.[1] The electron gun's output phase-space diagram under normal operations (0 T) is shown in Fig. 5.5a. The effect of a 0.011 T MR's fringe magnetic fields on a magnetically unshielded electron gun's output phase-space is shown in Fig. 5.5b. Figure 5.5c shows the electron gun's output phase-space when a passive magnetic shield, which has a uniform thickness of 5 mm and is 146.5 mm long, was used. The electron gun's output phase-space when an optimized active magnetic shield was used is shown in Fig. 5.5d. Both output phase-spaces in Figs 5.5c and 5.5d show that both type of magnet shield (passive and active) can return the electron gun to its normal state since the resulting phase-space resembles phase-space presented in Fig. 5.5a. The calculated ε_{rms} (Eq. 2.70) for 0 T, unshielded linac, passively shielded linac, and actively shielded linac are 0.457π, 3.242π, 0.671π, and 0.470π mm-mrad, respectively.

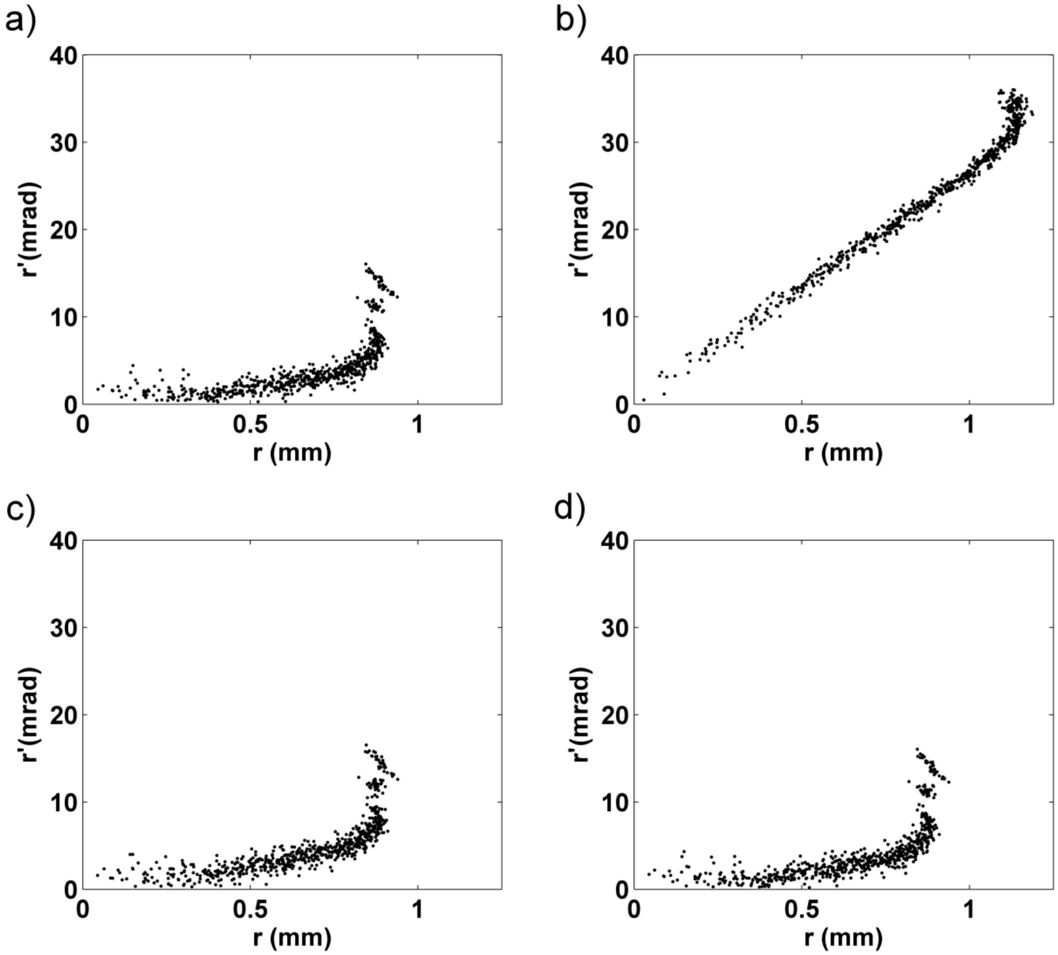

Figure 5.5: The phase-space diagram for an electron gun output beam is shown for four simulation conditions: a) a linac during normal operation (0 T), b) an unshielded linac, c) a passively shielded linac (which used a 5-mm-thickness and 146.5-mm-long passive shield), and d) an actively shielded linac. For scenarios b to c, a linac-MR SAD setup of 1.0 m was used. In this figure, *r* and *r'* are the radial distance and angular deflection calculated by Eqs 2.68 and 2.69, respectively.

5.3.3 Passive magnetic shield studies

The results of the passive magnetic shield studies shows that the passive magnetic shield can shield the linac from longitudinal MR fringe magnetic flux densities. With a linac-MR SAD of 1.0 m, the expected MR's fringe magnetic flux density in the electron gun is expected to be 0.011 T.

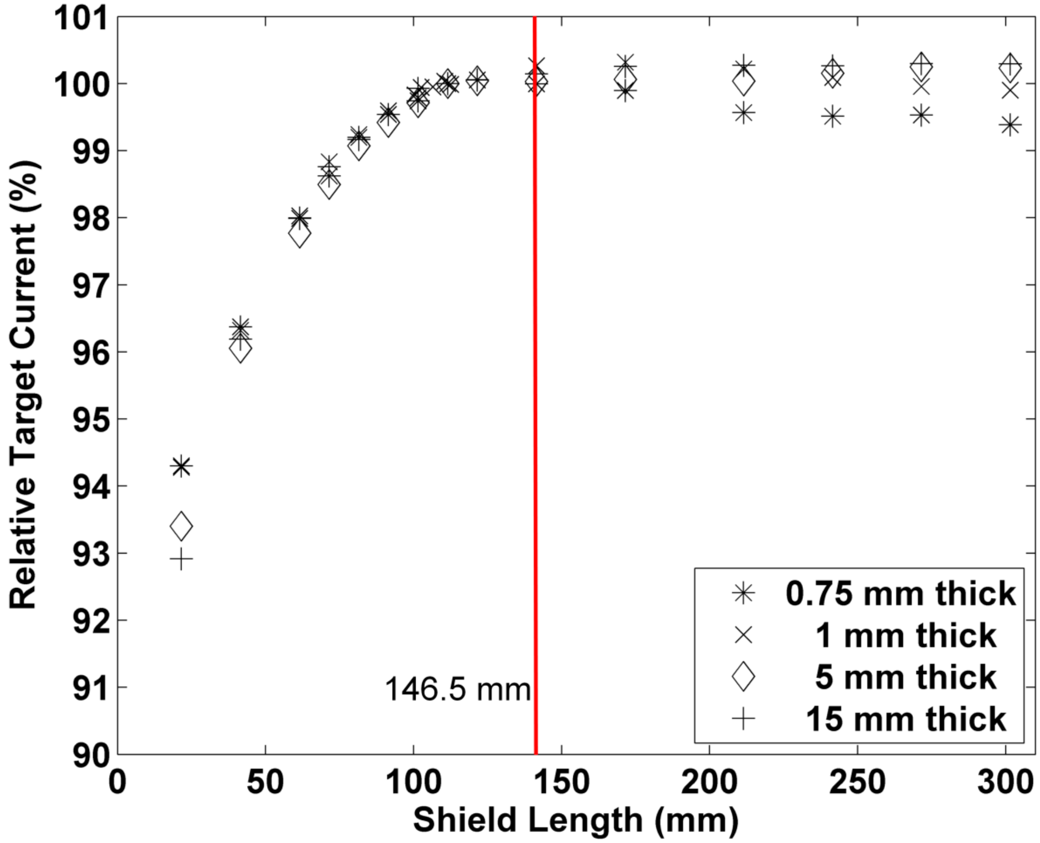

Figure 5.6: The target current (as a percentage of the nominal case) for four passive shield thicknesses is plotted against the passive shield length. The linac-MR SAD setup of 1.0 m was used for the simulations. At a shield length of 146.5 mm, full target current recovery is possible for the four shield thicknesses.

Figure 5.6 shows the target current recovery when passive shields were incorporated in the simulations. A target current recovery that is greater than 99 % of nominal is achievable for all passive shield thicknesses studied (from 0.75 to 15 mm). The target current recovery for thinner shielding (≤ 1-mm-thick) does not monotonically increase as the passive shield length is increased (Fig. 5.6). At a passive shield length of 146.5 mm, a peak target current recovery of 100.3 % is reached before the target current recovery begins to drop. This current recovery behaviour occurs because passive magnetic shields become partially magnetically saturated as its thickness is decreased and its length is increased.

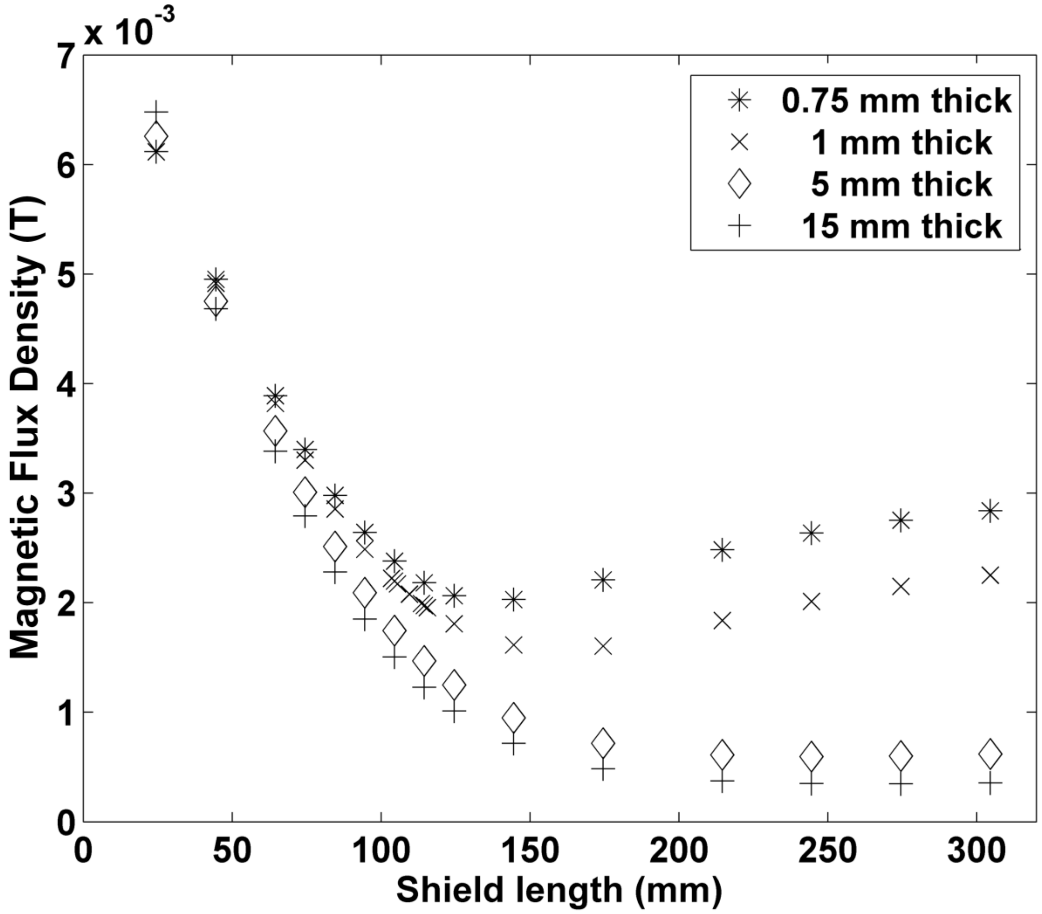

Figure 5.7: The mean magnetic flux densities in the electron gun plotted against the passive shield length for the four passive shield thicknesses in Fig. 5.6.

Because of the shield's magnetic saturation, the thinner passive shields become less effective at shielding the linac from the MR's fringe magnetic flux densities which is seen in Fig. 5.7. For passive shields that are thicker than 1 mm, the target current recovery does not exhibit this behaviour and increases monotonically with increasing shield length. This behaviour is reflected in Fig. 5.7 by the monotonic decrease in the mean magnetic field strength in the electron gun for these passive shields.

The presence of magnetic shielding can influence field homogeneity of an MR imager. Previous inhomogeneity studies on the linac-MR with large passive magnetic shields (2 m x 2 m x 0.05 m, with a volume of 0.2 m^3) and have shown that the resulting inhomogeneity[13-15] was manageable by standard shimming.[16] The passive magnetic shields used in this work are the same distance away from the MR's isocenter but are much smaller in volume (≤ 0.0028 m^3) than the ones used in the previous studies. Therefore, the magnetic shielding is not expected to create large field inhomogeneities in the MR's imaging region. However, in order to estimate the field inhomogeneities caused by the passive shields, the *currentloop$_{FEM}$ model* was used to calculate a worst-case scenario which is represented by the largest passive shielding (15-mm-thick and 299.5-mm-long with a volume of 0.0028 m^3). This passive shield caused a ΔB_0 of 124 ppm and a maximum field inhomogeneity of 66 ppm and 136 ppm for a 30-cm and 50-cm DSV, respectively. These inhomogeneities are shimmable since inhomogeneities of several hundred ppm's are manageable by standard shimming,[16] the passive shielding used in this study will not affect the MR's imaging volume.

5.3.4 Active magnetic shield studies

The active magnetic shield was optimized through a built-in Matlab function (fmincon) by minimizing Eq. 5.1. The optimization of the active shield produced a pair of coils with an ideal separation distance of 29.5 mm. The total current *nI* (where *n* is the number of windings in the active shield coils and *I* is the current for a single loop) for the active shield coil located closest to the waveguide was 625 A-turns while the coil that was further away from the magnet has a total current of 430 A-turns. By using many windings in each active shield coil, this active shield can be built with conventional power and cooling. Its power and cooling requirements are much less than that required for the active shield coils in the *perpendicular linac-MR configuration*.[17] Incorporating this optimized active shield into the FEM simulation led to a reduction of the mean magnetic flux density magnitude in the electron gun from 0.011 T to 1.1 x 10^{-4} T. A target current recovery from 83 % to 100.2 % of nominal is observed when this optimized active shield was used. This small gain in target current shows the competition between the effects of longitudinal magnetic fields on the waveguide and on the electron gun. Because this active shield uses current loops, its magnetic field strength decreases quickly as one gets further away from the shield's center. Therefore the active shield leaves a large portion of the waveguide remains unshielded while it shields the electron gun. The presence of longitudinal magnetic fields in the electron gun causes a loss in the current input into the waveguide, which results in lost target current.[1] However, its presence in the waveguide can result in current gain since some of the electrons that would be lost in the waveguide under normal operation are confined by the longitudinal magnetic fields. Therefore, the target current is increased.

The magnetic fields from the active shield coils caused a ΔB_0 of 2.35 ppm and a maximum field inhomogeneity of 1.05 ppm and 2.13 ppm for a 30-cm and

50-cm DSV, respectively. These inhomogeneities can be easily manageable by shimming.[16]

5.3.5 Homogeneous magnetic fields

We are interested in how the passively shielded linac performs over a range of magnetic field strengths. § 5.3.3and 5.3.4studied the effects of a 0.011 T fringe magnetic flux densities at the electron gun, however other field strengths can be caused by a change in the B_o field strength or a change in the linac-MR system's SAD. The fringe magnetic flux density in the electron gun varies by only 3.6 x 10^{-4} T (Fig. 4.3) from the cathode to the anode. From § 4.3.3, replacing the magnetic flux density from the $currentloop_{analytic}$ *model* with a 0.011 T parallel homogeneous magnetic flux density resulted in a cathode emission, injection, and target currents changes of only 0.001 %, 0.001 %, and 1 %, respectively. Since the $currentloop_{FEM}$ *model* agrees well with the $currentloop_{analytic}$ *model* (§ 5.3.1), the magnetic flux densities from the $currentloop_{FEM}$ *model* can be approximated by homogeneous magnetic flux densities, which have equal strength everywhere and are parallel to the net electron trajectories in the waveguides..

To simplify this portion of the study, the passive shield length for all thicknesses simulated in this part of the study is fixed to 146.5 mm. This was chosen since from § 5.3.3, it was shown (Fig. 5.6) that a full target current recovery occurs at this passive shield length for all passive shield thicknesses studied. Using this length as a starting point, only the effect of the passive shield thickness on the target current recovery was investigated in this part of the study.

The injection currents for each passive shield thickness in Fig. 5.8 show a slight increase before dropping sharply. This behaviour was also observed previously[1] in CHAPTER 4. This slight increase in the injection current is caused by the increasing cathode emission current. As homogenous magnetic flux density magnitude increased, a reduction of the space charge surrounding the electron gun cathode occurs. This leads to the increasing cathode emission. Furthermore, the radius increased with the increasing emission current. As the beam radius increased, more electrons start to impact onto the anode and are removed from the injection current causing the sharp reduction in the injection current seen in Fig. 5.8. In Fig. 5.8, this sharp drop in injection current began at 0.015, 0.032, 0.08, and 0.125 T when no shield, 1-mm-thick, 5-mm-thick, and 10-mm-thick shields, respectively, are used on the linac.

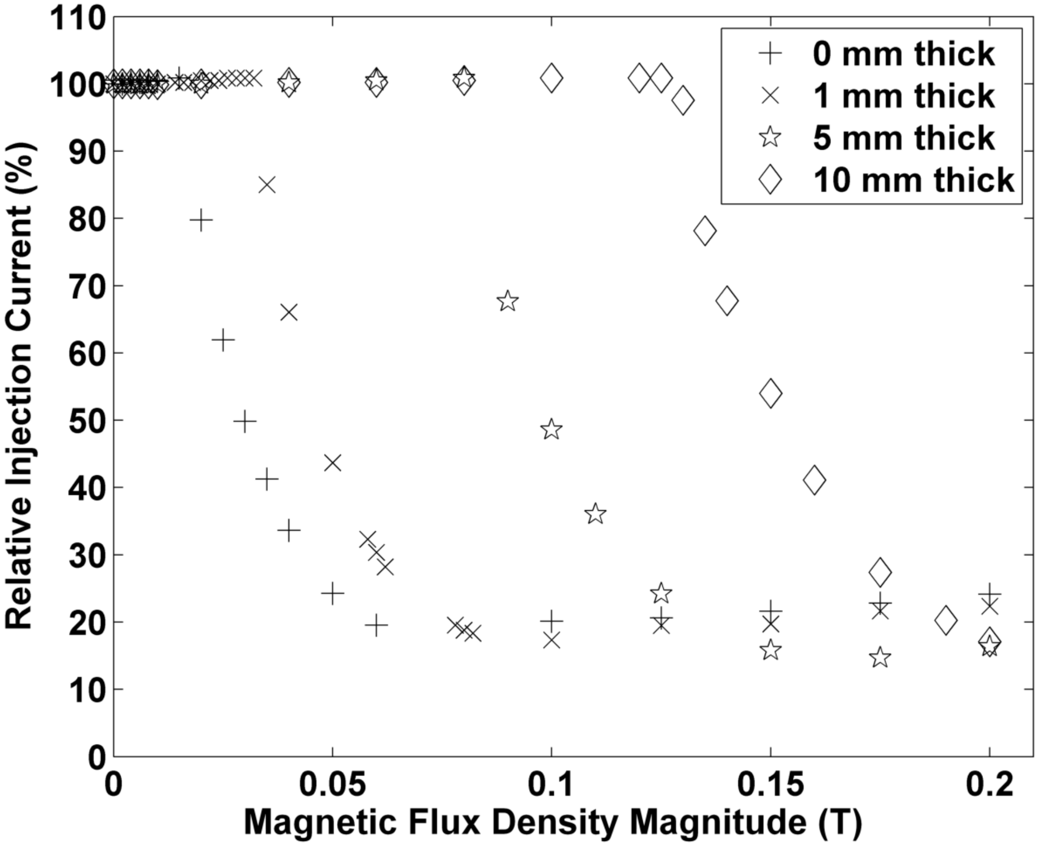

Figure 5.8: The relative injection currents (as a percentage of the nominal injection current) for four passive shield thicknesses are plotted against the homogeneous magnetic flux density magnitudes. A fixed passive shield length of 146.5 mm was used for all shield thicknesses investigated.

Since the electron gun and waveguide need to work as a single unit in a linac, any injection current loss will result in lost target current (Fig. 5.9). As stated earlier, the lost target current causes a loss in the dose rate and an increased in the treatment times. Although there is a slight increase in the injection currents, the target current for each passive shield thickness continue to drop as the increasing magnetic flux density increases. Figure 5.9 shows the decreasing target current as the homogeneous magnetic flux density increased for all the passive shield thicknesses that were studied. As the shield's thickness increases larger field strengths are needed to create the same level of target current lost. For example, a target current that is 84% of nominal occurs at 0.0147, 0.0307, 0.0704, and 0.0886 T when no shield, 1-mm-thick, 5-mm-thick, and 10-mm-thick shields, respectively, are used.

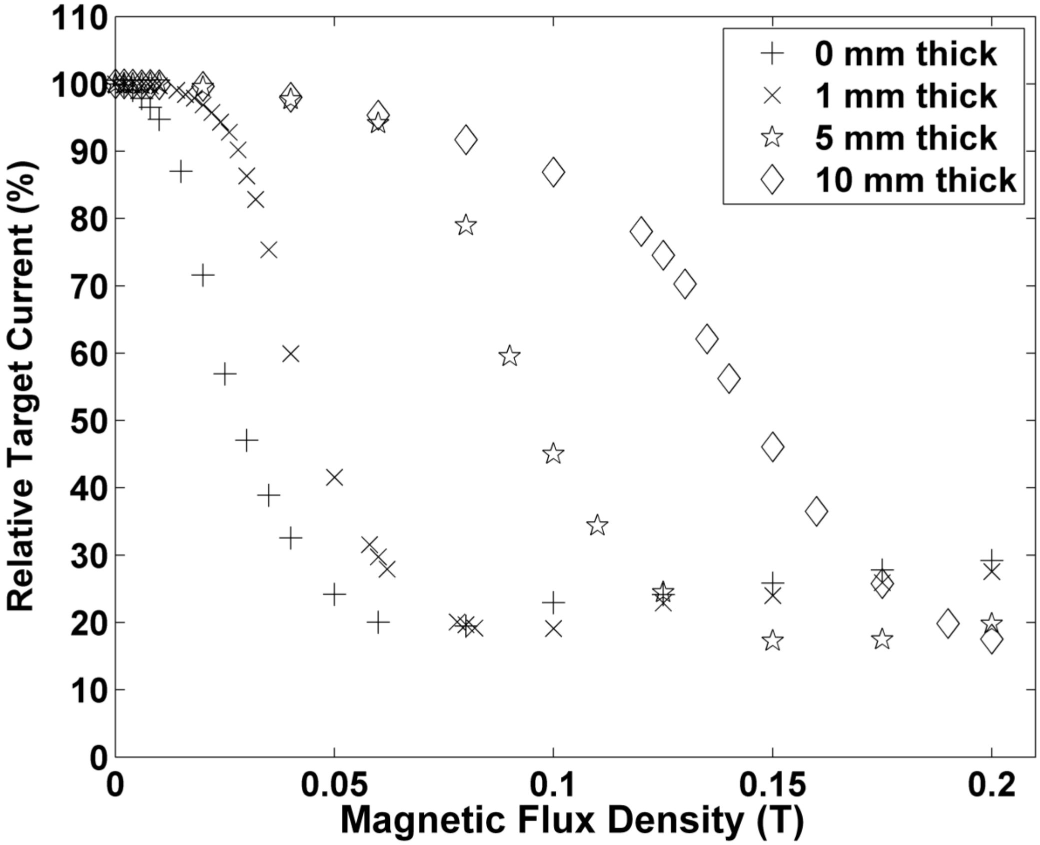

Figure 5.9: The relative target current (as a percentage of the nominal target current) as the longitudinal homogeneous magnetic flux densities are increased. A fixed passive shield length of 146.5 mm was used for all shield thicknesses investigated.

When the magnetic flux densities in the electron gun of a linac-MR system varies by 3.6 x 10^{-4} T or less, the results shown in Fig 5.8 and 5.9 are a valid approximation to the injection and target currents' behaviour for different passive shielding scenarios. The results presented in Figs 5.8 and 5.9 show that a passive shield designed for an MR fringe magnetic flux density such as a 0.05 T can be used to shield the linac from weaker MR fringe magnetic flux densities. These two figures show how robust and flexible the passive shielding solution for different MR fringe magnetic fields. The technique of passive shielding described above can be used to optimize shielding for different cylinder lengths and different magnetic flux density for the various linac-to-MR scenarios possible. Either passive or active shielding described above can be easily engineered to shield the linac and electron gun from the effects of the MR's magnetic flux densities in the *parallel linac-MR configuration*. Active shielding may require some cooling and additional maintenance, however.

5.3.6 Linac performance in the in-house linac-MR system

The removal of the material covering the bore of one of the MROpen^{TM}'s magnet pole resulted in the occurrence of larger radial magnetic flux density near the uncovered bore in the *full magnet$_{FEM}$ model*. When only the electron gun casing is used as a magnetic shield, the target current was 82 % of nominal. Both of the passive shields that were modelled (the 25-mm-thick steel cylinder and the 5-mm-thick, 146.5-mm-long passive shield) were able to magnetically shield the linac from the MROpen^{TM}'s fringe magnetic flux densities. A target current recovery of 99.9 % and 99.2 % was the result of the presence of the 25-mm-thick steel cylinder and 5-mm-thick, and 146.5-mm-long passive shield, respectively.

5.4 Summary

Although the effects of magnetic fields on the linac in the *parallel configuration* still result in lost dose rate,[1] the lost linac output can be recovered by using magnetic shielding, which was demonstrated by the work presented in this chapter. Either passive or active magnetic shielding can be used to shield the electron gun and still leave large portions of the waveguide exposed to the collimating effects of the fringe fields of the MR in the parallel linac-MR configuration. Both passive and active magnetic shielding caused minimal inhomogeneities, which are manageable by shimming,[16] in the 30-cm and 50-cm DSV's. Although the electron gun's casing provides some magnetic shielding, additional magnetic shielding is still required to recover the linac output that was lost due to magnetic deflections. Greater than 99 % of the nominal target current can be recovered by surrounding the linac and gun casing with passive shielding of thicknesses greater than 0.75 mm. An optimized active shielding comprised of a pair of 110 mm diameter coils with 625 and 430 A-turns running in each coil can fully recover the lost target current when it is placed around the electron gun and its casing. However, the active shield may introduce additional complexity such as the need for cooling and maintenance systems for the coils. Simulations using the magnetic fields from the modified MROpen^{TM} imager showed that the passive shields that were investigated are adequate for the linac's magnetic shielding in the *parallel linac-MR configuration*.

5.5 References

[1] J. St. Aubin, D. M. Santos, S. Steciw and B. G. Fallone. "Effect of longitudinal magnetic fields on a simulated in-line 6 MV linac," Med. Phys., **37,** 4916-4923, (2010).

[2] D. E. Constantin, R. Fahrig, and P. J. Keall "A study of the effect of in-line and perpendicular magnetic fields on beam characteristics of electron guns in medical linear accelerators", Med. Phys. **38**, 4174-4185 (2011).

[3] N. B. S. Gloria, M. C. L. Areiza, I. V. J. Miranda and J. M. A. Rebello. "Development of a magnetic sensor for detection and sizing of internal pipeline corrosion defects," NDT E Int., **42,** 669-677, (2009).

[4] M. de Berg, O. Cheong, M. van Kreveld and M. Overmars. “Chapter 9: Delaunay Triangulations” in *Computational Geometry: Algorithms and Applications* (Springer-Verlag, Berlin, 2008), pp. 191-218.

[5] Y. Saad. “Chapter 9: Preconditioned Iterations” in *Iterative methods for sparse linear systems* 2nd ed (SIAM, Philadelphia, 2003), pp. 261-281.

[6] U. Trottenberg, C. Oosterlee, A. Schueller. *Multigrid* (Academic Press, San Diego, 2001).

[7] J. St. Aubin, S. Steciw, C. Kirkby and B. G. Fallone. "An integrated 6 MV linear accelerator model from electron gun to dose in a water tank," Med. Phys., **37**, 2279-2288, (2010).

[8] J. St. Aubin, S. Steciw and B. G. Fallone. "The design of a simulated in-line side-coupled 6 MV linear accelerator waveguide," Med. Phys., **37**, 466-476, (2010).

[9] R. Fletcher. “Chapter 5: Quadratic Programming,” in *Practical Methods of Optimization* (John Wiley and Sons, 1987), pp. 229-258.

[10] P.E. Gill, W. Murray, and M.H. Wright. “Section 5.3: Special Problem Categories,” in *Practical Optimization* (Academic Press, London, 1981), pp. 176-181.

[11] M. J. D. Powell, "Variable Metric Methods for Constrained Optimization," *Mathematical Programming: The State of the Art*, (A. Bachem, M. Grotschel and B. Korte, eds.) Springer Verlag, p 288-311, (1983).

[12] W. Hock and K. Schittkowski, "A Comparative Performance Evaluation of 27 Nonlinear Programming Codes," Computing, **30**, 335, (1983).

[13] B. G. Fallone, B. Murray, S. Rathee, et al. "First MR images obtained during megavoltage photon irradiation from a prototype integrated linac-MR system," Med. Phys., **36,** 2084-2088, (2009).

[14] S. Steciw, T. Stanescu, M. Carlone, B. G. Fallone. “Magnetic shielding of a coupled MRI-Linac system,” Med. Phys., **34**, 2623-2623, (2007).

[15] B. Murray, B. G. Fallone, M. Carlone, S. Steciw, T. Stanescu, S. Rathee. “Designing a Linac to Operate Near an MRI,” Radiother Oncol, **84** (**Supp 2**), S3, (2007).

[16] E. M. Haacke, R. W. Brown, M. R. Thompson, R. Venkatesan. *Magnetic Resonance Imaging: Physical Principles and Sequence Design* (John Wiley and Sons, New York, 1999), pp. 841.

[17] J. St. Aubin, S. Steciw and B. G. Fallone. "Magnetic decoupling of the linac in a low field biplanar linac-MR system," Med. Phys., **37,** 4755-4761, (2010).

[18] S. Humphries. *Charged Particle Beams* (Wiley, New York, 1990).

[19] T. P. Wangler. *RF Linear Accelerators* (Wiley-VCH, Weinheim, 2008).

CHAPTER 6 : CONCLUSION AND FUTURE WORK

6.1 Concluding statements

The work presented in CHAPTER 4 and CHAPTER 5 builds on previous work done by our group. This work investigated in CHAPTER 4 the effects of longitudinal/parallel magnetic fields on a 6 MV in-line linac such as a Varian 600C linac. The lost linac output was quantified by using the target current losses in the presence of parallel magnetic fields. Other effects such as increases in the linac target beam's FWHM have an insignificant effect on the linac treatment beam. Parallel magnetic fields have an insignificant effect on the electron beams' mean energy and energy distribution. In CHAPTER 5, the exploration of the use of magnetic shields (either passive or active) for the linac electron gun and waveguide was presented. For all passive shield thicknesses investigated (up to 15 mm), full target current recovery is possible for a passive shield length of 146.5 mm. A simple active shield configuration, such as a current ring pair with optimized ring currents and separation distance, was needed to recover the full target current lost through magnetic deflection. From the work presented in this thesis, it was shown that the adverse effects of parallel magnetic flux densities on the linac can be eliminated through the use of either passive or active magnetic shield.

6.2 Future work

The final form of the clinical version of the *parallel linac-MR configuration* is not yet finalized. A new waveguide for the linac-MR is currently being developed and an MR imager that is more compact than the commercially available MROpen^{TM} system is being considered for the clinical version of the linac-MR. Since the MR's magnetic fringe flux densities depends on the MR magnet design, studies of the performances of different waveguides and/or MR imagers combinations can be performed. These studies are necessary to ensure that the remedies proposed in CHAPTER 5 are valid for the clinical version of the linac-MR system. Since the work present in this thesis consist of computer simulations, experiments can be performed when the parallel-configured linac-MR system is built to valid the results presented in here.